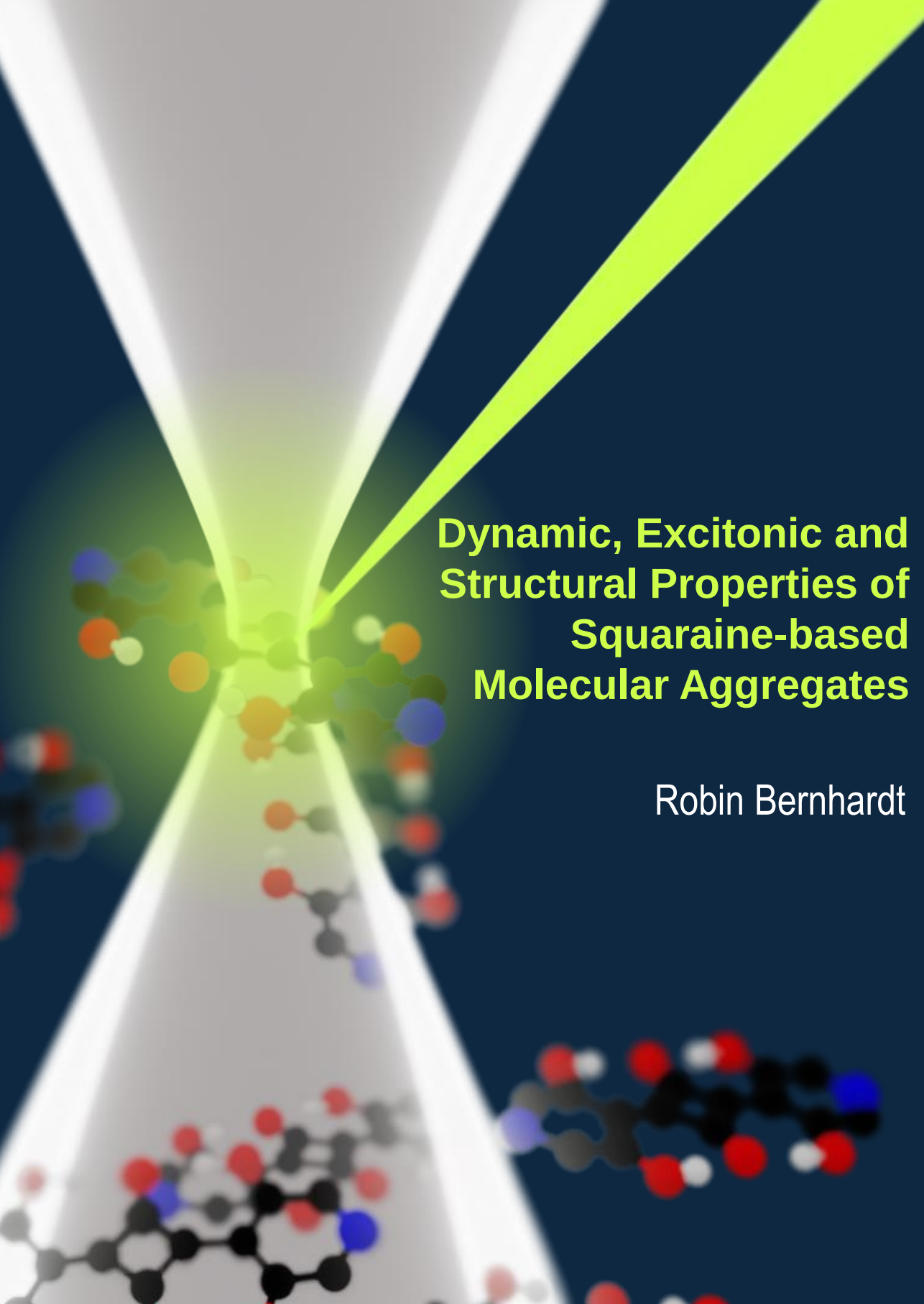

Dynamic, Excitonic and Structural Properties of Squaraine-based Molecular Aggregates

Robin Bernhardt

UNIVERSITÄT
ZU KÖLN

Dynamic, Excitonic and Structural Properties of Squaraine-based Molecular Aggregates

Inaugural-Dissertation
zur
Erlangung des Doktorgrades
der Mathematisch-Naturwissenschaftlichen Fakultät
der Universität zu Köln

vorgelegt von
M. Sc. Robin Bernhardt
geboren in Bergisch Gladbach

Köln, 2024

Gutachter:
Prof. Dr. Paul H. M. van Loosdrecht
Prof. Dr. Maxim S. Pchenitchnikov

Vorsitzender:
Prof. Dr. Stephan Schlemmer

Beisitzer:
Dr. Tianyi Wang

Dedication
To my parents and my Grandpa

"Handle nur nach derjenigen Maxime,
durch die du zugleich wollen kannst,
daß sie ein allgemeines Gesetz werde."
Immanuel Kant

Contents

Chapter 1

Introduction

This chapter gives a general introduction to π-conjugated organic dye molecules and their aggregates, and squaraine molecules in particular. Furthermore, the concept of main technique used in this thesis is introduced. The chapter closes with a presentation of the scope of this thesis.

1.1 Introduction to Organic Dye Molecules

Organic dye molecules are a crucial material class for organic electronics in today's technology [1–3], and have served various purposes for thousands of years and are deeply ingrained into human history and culture. As their name implies, organic dye molecules have been widely used to color clothes, food, decorations, and many other items of cultural and aesthetic importance. Since ancient times, humans have used plants like woad, saffron, and madder to extract dyes like indigo (blue), α-crocin (yellow), and alizarin (red), respectively. Some of these dyes needed an enormous amount of effort to be produced, making them an almost priceless display of wealth and power. Tyrian purple comes to mind—also known as imperial dye.

Even before the times of human beings, nature had been utilizing dye molecules as key molecules for both plants and animals. Chlorophyll imparts a green color to plants, and is at the core of photosysnthesis [4, 5], while the porphyrin heme, closely related to chlorophyll, is the central building block for oxygen transportation in our blood—and gives it its rich red color [6, 7].

At the dawn of modern synthetic chemistry, William Henry Perkin synthesized the first artificial dye known, mauveine, by accident in 1856 [8]. Since then, the variety and affordability of dyes grew exponentially to this day.

With the rise of semiconductor electronics and optoelectronics in the last 60 years, the interest in the (opto-)electronic properties of dye molecules has risen dramatically, inspired by the work of Heeger, MacDiarmid, and Shirakawa on conductive polymers [9]. Nowadays, semiconductor electronics are still dominated by inorganic semiconductors like Germanium, Gallium Arsenide, and—most importantly—Silicon. However, limitations of technologies based on these materials have become evident. The mechanical rigidness, high energy consumption in production, and discrete band gap energy of these materials drive the search for alternatives. In this context, organic dye molecules can shine bright, as they offer intense absorption cross-sections, are light weight, can be bio-compatible, demonstrate mechanical flexibility and a high degree of customizability, and are cheap and scalable in production. These properties are crucial for the active materials in solar cells, photodetectors, and light emitting devices.

Organic light emitting diodes (OLEDs) are the most successful examples of the or-

ganic electronics family to date, as they have gained an important market share for mobile and television displays [1–3]. At the same time, major advances have also been made for organic light harvesting systems, especially organic solar cells (OSCs), which have overtaken dye-sensitized solar cells in power-conversion efficiency [10–12]. The development of OSCs has progressed significantly over the last 40 years, first using small molecules [13, 14], and later also polymers [15, 16]. For a long time, the bulk heterojunction of two organic compounds—one electron acceptor and one electron donor—has been found to be the most efficient microstructure, as it maximizes the interface between the two compounds, which is crucial for the charge separation of strongly bound electron-hole pairs, i.e., excitons [13–16]. As an electron acceptor, [6,6]-phenyl-C_{61}-butyric acid methyl ester (PCBM), a derivative of fullerene, was the go-to choice for organic solar cells [17]. The dominance has been challenged in recent years, with small-molecule, non-fullerene acceptor based organic solar cells reporting high efficiencies up to over 15% developed [18, 19]. For electron donors, many different polymers and small molecules have been used, but over the last decade, polymers have outperformed their small molecule counterparts, consistently scoring record efficiencies [10–12]. However, the latter have recently been able to close the efficiency gap, with efficiencies of up to over 14% reported [20]. While the efficiencies still cannot reach the performance of silicon solar cells [10–12], they increased significantly from less than 1% to over 15%. This feasible efficiency combined with the economical and ecological benefits of organic compounds makes organic solar cells an immensely popular field in both science and industry. Physicists, chemists, material scientists, engineers, and biologists alike are tackling the major challenge of understanding and removing the bottlenecks of these light harvesting devices.
These limitations are manifold, and while some are material-dependent, there are general problems which come with using organic compounds: inefficient charge separation of the strongly bound electron-hole pairs, poor transport of charge carriers to the electrodes, limited absorption wavelength window, low device lifetime, etc. All traits are extremely sensitive to the morphologies and structures of the active media used, as well as the interactions between the absorbing media. Depending on the molecular system, the supramolecular packing arrangement can either be self-organized, as is the case for the systems discussed in this thesis, or induced by a template [21]. Resolving the structure-property relationships in organic, often amor-

phous materials is therefore of enormous importance.

1.2 Ultrafast Processes in Molecular Systems

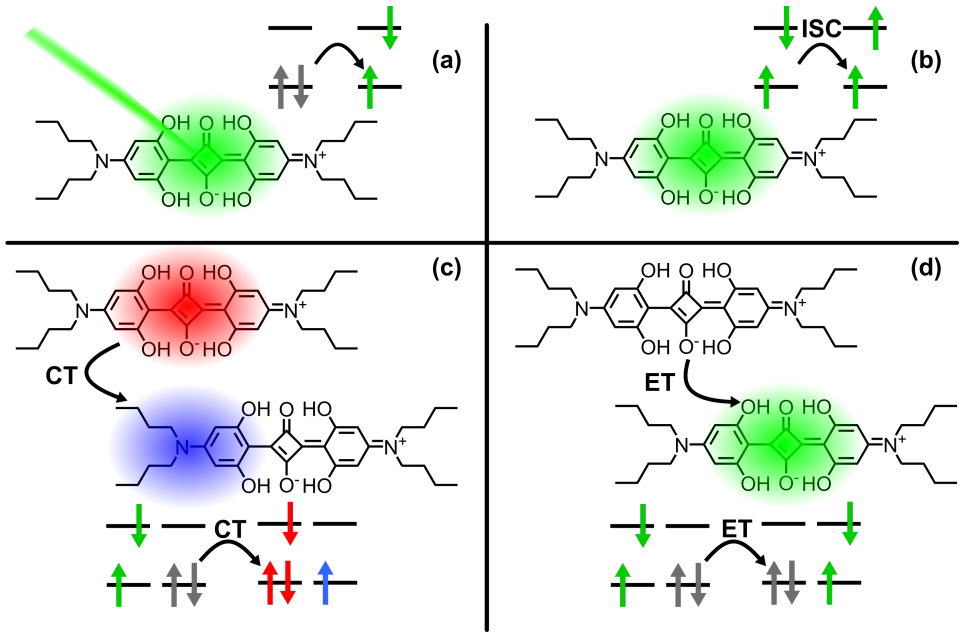

Figure 1.1: Selected ultrafast processes happening in molecular systems. The molecule displayed is 2,4-bis[4-(N,N-dibutylamino)-2,6-dihydroxyphenyl]-squaraine (nBSQ). (a) Excitation of the molecule and generation of a singlet exciton. (b) Intersystem crossing (ISC) resulting in a triplet exciton. (c) Charge transfer (CT) to neighboring molecules. (d) Energy transfer (ET) to neighboring molecules. Note that the energy levels are only for illustration purposes and do not represent the actual energy levels.

Most of the processes inside organic solar cells mentioned in the last section are based on electronic molecular proccesses. Many of these processes happen on ultrafast timescales, which is far beyond the resolution of human senses. To directly monitor and visualize ultrafast processes like exciton generation, intersystem crossing, and energy or charge transfer (see Fig. 1.1), which happen on a timescale from 1 fs (10^{-15} s) to 1 ns (10^{-9} s), optical ultrafast spectroscopy techniques are required. Ultrafast spectroscopy is a powerful tool employing (at least) two ultrashort laser pulses in a

pump-probe scheme.

The first pulse, the so-called *pump* pulse, is exciting the system, pushing it out of equilibrium. The second pulse, the *probe* pulse, probes a desired optical property, which changes when the system is out of equilibrium. By changing the optical path length of one of the pulses, the delay between pump and probe pulse can be controlled, which enables recording of the temporal progression of the system back to equilibrium, offering a direct measurement of the evolution of lifetimes of the involved excitations.

1.2.1 Ultrafast Transient Absorption Spectroscopy

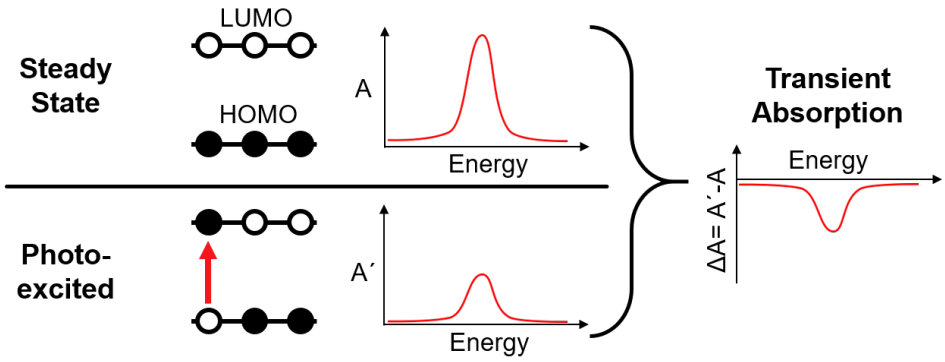

Figure 1.2: Sketch of the working principle of transient absorption spectroscopy for a two-level system. If photoexcitation of electrons from the HOMO into the LUMO state occurs, the absorption spectrum will change. Calculating the difference between the steady-state and excited absorption spectra yields the transient absorption spectrum.

The main experimental technique used in this thesis is ultrafast transient absorption spectroscopy, a pump-probe spectroscopy technique based on sub-picosecond laser pulses. The core idea is that an intense monochromatic pump pulse selectively excites an excitonic species, changing the optical properties related to this exciton. A time-delayed broadband probe pulse is used to measure the absorption spectrum before $(A(\omega, t < t_0))$ and after $(A'(\omega, t > t_0))$ the pump excitation at t_0. As this time delay can be controlled, we can measure the differential absorption as a function of time, allowing access to both spectral and temporal resolutions. The differential absorption can further be corrected for scattering contributions, by subtracting the

spectra collected without a probe source $I_{pump,dark}$ and I_{dark}, leading to

$$\Delta A(\omega, t) = A'(\omega, t) - A(\omega) = -log_{10}\left(\frac{I_{pump,probe} - I_{pump,dark}}{I_{probe} - I_{dark}}\right). \tag{1.1}$$

From the temporal resolution, we can access information about the evolution of a given state as well as the interaction between different states. A simple sketch is shown in Fig. 1.2. In this simple example, the steady-state absorption spectrum is dominated by a single highest occupied molecular orbital (HOMO) to lowest unoccupied molecular orbital (LUMO) transition of a molecule. Under steady-state conditions, all molecules are in their ground state, with the highest energy electron residing in the HOMO. Using an ultrashort monochromatic pulse, we could excite some molecules, promoting some of the electrons residing in the HOMO state into the LUMO state. After the HOMO state is depleted and the LUMO state is populated, the probability for this transition will be reduced, as there is less HOMO population to excite—the example system will absorb less. This leads to the negative transient absorption signal seen in Fig. 1.2.

1.2.2 Common Transient Features

For most systems studied using transient absorption spectroscopy, the transient properties are governed by many more transitions than a single HOMO-LUMO transition. Delocalization of excitons in aggregates and crystals, charge transfer and separation, and energy transfer to other molecules can drastically change the transient response of the systems at hand. These effects produce a multitude of possible features of different signs and spectral positions, leading to a rich transient absorption spectrum. Fig. 1.3 summarizes the most important transient features observed for generic coupled molecular systems. They can be categorized into three main categories:

1. Ground state bleach (GSB);
2. Stimulated emission (SE);
3. Photoinduced absorption (PIA).

While many different types of electronic states can contribute to these features, the physical origin is always the same for each feature. The first and most fundamental

transient feature is the ground state bleach. It occurs because of the depletion of the ground state of a system after photexcitation, similar to the example given above in Fig. 1.2. The ground state bleach is observed for all optically bright excited states connected to the ground state, which makes it a "mirror image" of the steady-state absorption spectrum of the excited species.
Stimulated emission occurs when the excited, optically bright state relaxes radiatively due to interaction with the probe pulse. As this interaction creates more photons, the detector registers a higher intensity for the probe pulse, which gives a signal identical to a higher transparency, i.e., negative signal in transient spectrum. The transient absorption spectrum of stimulated emission is similar to the ground state bleach, but since only emissive states undergo stimulated emission, the stimulated emission transient spectrum looks like the "mirror image" of the fluorescence spectrum of the given material.
Photoinduced absorption can be observed for many different states, including e.g. triplets and charge transfer states, as well as spectral shifts, and can therefore occur in energy regions deviating from the steady-state absorption/emission footprint of the sample. This can be either a transition from an excited state to a similar excited state of higher quantum number (see Fig. 1.3 (**4, 6, 8**)), or a previously dark transition from the ground state (**3**). The latter is sometimes referred to by different names like "two-exciton absorption" to differentiate it from the former [22, 23]. As the activation of optical excitations will lead to more absorption, the sign of the transient response of photoinduced absorption is always positive. If the state involved in PIA is not directly excited by the pump pulse, it allows probing of the transition rate from the initially excited state into the PIA state.

1.3 Optical Properties of π-conjugated Molecules and their Aggregates

To achieve light-matter coupling in the visible (VIS) or near-infrared (NIR) light regions, a specific molecule must possess electronic states with suitable energy spacing (around 1.5-3 eV/400-800 nm for visible light). Frequently, this requirement is not met, because the energy gap between the highest occupied molecular orbital (HOMO) and the lowest unoccupied molecular orbital (LUMO) is greater, necessi-

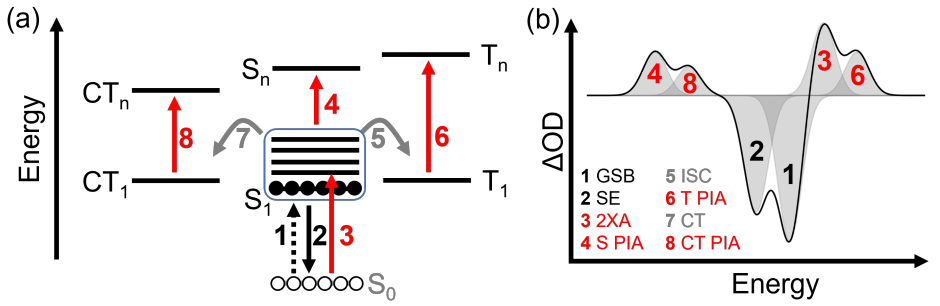

Figure 1.3: Different transient features (a) that can possibly appear in the transient absorption spectra (b) of aggregated dye molecules upon photoexcitation into the S_1^0 state. **1** denotes the ground state bleach (GSB) of the $S_0 \rightarrow S_1^0$ transition, while **2** corresponds the stimulated emission (SE) of the $S_1^0 \rightarrow S_0$ transition. Both transitions provide a negative signal. The singlet band can also induce two-exciton absorption (2XA) of the $S_0 \rightarrow S_1^n$ transition (**3**), as well as the photoinduced absorption of the $S_1^0 \rightarrow S_n$ transition (S PIA, **4**). Via intersystem crossing (ISC, **5**) or charge transfer (CT, **7**), triplet and CT states can become populated as well, yielding a $T_1 \rightarrow T_n$ (T PIA, **6**) or $CT_1 \rightarrow CT_n$ transition (CT PIA, **8**), respectively.

tating the use of ultraviolet (UV) light for overcoming the gap. To lower the energy to visible light energies, the electronic states need to exhibit greater delocalization. For electronic eigenstates to be genuinely delocalized, the electron density should be evenly distributed throughout the entire bond. This cannot be achieved with σ-like bonds, as the electron density is concentrated around the midpoint between two atoms, with minimal density elsewhere. Instead, π-like orbitals are required to evenly distribute the electron density. The concept of π-bond delocalization is shown for the smallest example system, ethene, in Fig. 1.4.

π-like bonds necessitate p- or higher orbitals to be aligned perpendicular to the bond direction. In the case of carbon atoms, the most abundant element in organic dyes, this condition is met when only three or fewer of the four valence electrons are involved in a planar σ-bond. This condition is met in sp^2-hybridized orbitals, as well as the rarely occuring sp^1-hybridization. In this thesis, the relevant orbitals are sp^2-hybridized for all discussed dyes. The threefold planar bonds give rise to the characteristic hexagonal structure found in many organic molecules [24], while the π-bonds can delocalize the electron wavefunction over several atoms and reduce the energy gap between the bonding ("π") and antibonding ("π^*") orbitals. This

extensive delocalization of π-bond orbitals is referred to as π-conjugation. In an extreme case, delocalization can extend quasi-infinitely, resulting in the well-known semimetallic properties of graphene [25].
An important feature of π-conjugation is that the transition between HOMO and

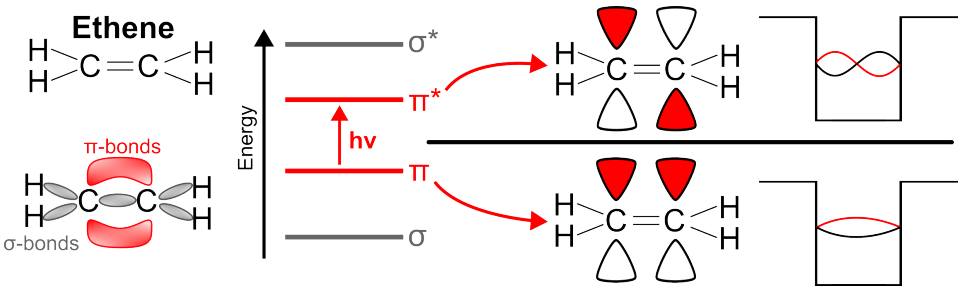

Figure 1.4: Sketch of the orbitals in ethene, the smallest π-bond system. Due to the sp^2-hybridization, the orbitals overlap either parallel or perpendicular to their extent, yielding π- and σ-bonds. The resulting bonding (π) and antibonding (π^*) π-orbitals represent the HOMO and LUMO of the system, and have a significantly lower energy difference, which allows photoexcitation by visible or even infrared light. Comparing the symmetries of the HOMO and LUMO shows a remarkable resemblance to the particle-in-a-box eigenstates [24].

LUMO can strongly couple to incoming light. In the perturbative regime of the electronic Hamiltonian of a molecule, the response of the electronic states to an emerging light field is given by

$$H' = \mu \cdot E(\nu), \tag{1.2}$$

where

$$\mu = e \langle \Psi_{LUMO} | \hat{x} | \Psi_{HOMO} \rangle = e \int \Psi^*_{LUMO} \, \vec{x} \, \Psi_{HOMO} \, d\vec{x} \tag{1.3}$$

is the transition dipole moment, $E(\nu)$ is the electric field of the light with a frequency ν, and H' represents the perturbation of the molecule Hamiltonian. Considering the symmetry and charge distribution of each orbital, the bonding HOMO orbital in a π-conjugated system typically exhibits even symmetry, while the antibonding LUMO orbital possesses odd symmetry. The complex product of HOMO and LUMO wavefunctions is therefore an odd function. As the position operator $\hat{x}$ is an odd function as well as, the integral used to calculate μ will be an even function, yielding a non-zero and often high value for the transition dipole moment. Therefore, if the

incoming electric field has a frequency which satisfies the condition

$$h\nu = \Delta\epsilon_{HOMO \to LUMO} - E_B = E_X, \tag{1.4}$$

photons can be absorbed efficiently to elevate the electrons from the HOMO into the LUMO state. Reversely, photons might also be emitted when an electron relaxes from the LUMO back to the HOMO state.
At this point it should be noted that the terms "HOMO" and "LUMO" are not sufficiently accurate, as they represent states and energies under the consideration that the HOMO is fully occupied and the LUMO is fully unoccupied. This obviously does not hold true when an electron occupies the LUMO after photoexcitation, interacting with the hole in the HOMO. This quasiparticle is called an (Frenkel) exciton and the photon energy has to match its energy (E_X) rather than the HOMO-LUMO gap. The difference in energy is called the exciton binding energy (E_B). The exciton binding energy is predominantly determined by the Coulomb-attraction of the electron and the hole, a term which can be hundreds of meV large for small organic molecules. Note that this bosonic/paulionic quasiparticle contains two half-integer spin particles and can therefore appear in singlet or triplet configuration. Only the singlet state is optically accessible, as it has an even symmetry.
Overall, the absorption and emission spectra of π-conjugated molecules are dominated by the contribution of HOMO-LUMO excitons, as long as the molecule is in an isolated environment like a gas or in (the right) solution.
In many condensed media of organic dye molecules like molecular crystals, aggregates or thin films, the optical properties might differ from the single molecular response. Energy levels of absorptive states might be shifted, and fluorescence can be either quenched or enhanced. These deviations arise from different intermolecular interactions, including Coulombic interactions between the charges and excitons of adjacent molecules, various forms of energy transfer, and intermolecular charge transfer. As applications often require a condensed medium, understanding these interactions between molecules and how they correspond to the optical properties is of high importance.
Historically, the first and most general theory for systems of coupled molecules, simply termed exciton theory, was developed by Michael Kasha in the 1960's [26]. The

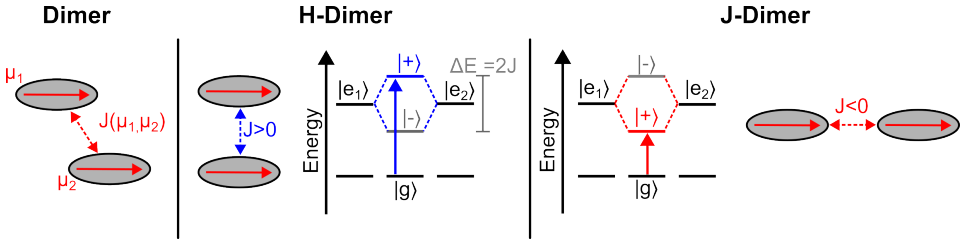

Figure 1.5: Spectral changes to a homodimer according to exciton theory. Two nearby molecules interact via their transition dipole moments, forcing their excitons to couple with an interaction energy J. This results in a delocalization of the eigenstates into collective excitations as superposition of single molecular excitations. Depending on the angle of the two molecules with respect to each other, the bright delocalized state can either appear red-shifted (J-dimer) or blue-shifted (H-dimer).

model is based on the Coulombic coupling of optically bright (singlet) exciton states of neighboring molecules through transition dipole - transition dipole interactions, which are analogue to electric dipole-dipole interactions. This model was first used to explain the enhancement of triplet emission (phosphorescence) at the expense of singlet emission (fluorescence) in a variety of molecular aggregates based on toluene, triphenylamine and other dyes [26].

Most notably, the Kasha model explained the changes of optical properties of pseudoisocyanine dyes upon aggregation, as discovered by Scheibe [27] and Jelly [28] independently, giving rise to an archetype of aggregation called J-aggregate (sometimes referred to as "Jelly-aggregate" or "Scheibe-aggregate").

These aggregates show a red-shifted (bathochromic), narrow absorption line, as well as an enhanced narrow emission line only slightly shifted with respect to the absorption line. They stand in opposition to the second archetype, the hypsochromic or H-aggregate. These aggregates are generally found to have a blue-shifted, often broader absorption line compared to the monomer, while the fluorescent emission is strongly suppressed.

A simple example of how the Kasha exciton model explains these types of aggregation is shown in Fig. 1.5 for the simplified case of parallel dimers. In this case, the transition dipole moment coupling energy J can be written as

$$J = \frac{\mu_1 \mu_2}{4\pi\epsilon_0\epsilon_r R_{1,2}^3} \left(1 - 3\ \cos^2(\theta_{1,2})\right). \tag{1.5}$$

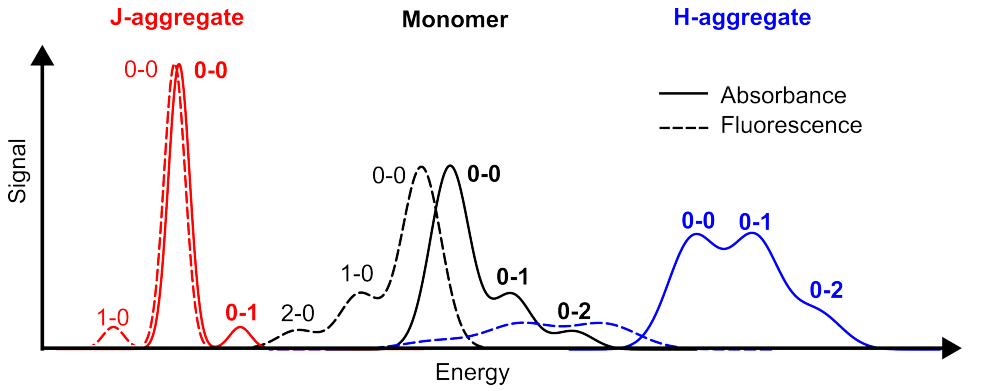

Figure 1.6: Spectral footprint of an archetypical J- (red) and H-aggregate (blue) with respect to a given monomer (black). The J-aggregate induces a strong red-shift, while the H-aggregate induces a small blue-shift. Furthermore, the peaks of the J-aggregate are narrowed compared to the monomer, while the H-aggregate shows even wider peaks. Finally, the fluorescence intensity is enhanced for J-aggregates, but quenched for H-aggregates.

Here, μ is the transition dipole moment of each molecule's exciton, R the distance, and θ the angle between the two molecules. ϵ_0 and ϵ_r represent the dielectric constant and permittivity, respectively. If the monomeric excitons are chosen as a state basis, the Hamiltonian takes a convenient matrix form

$$H = \begin{bmatrix} \epsilon & J \\ J & \epsilon \end{bmatrix}. \tag{1.6}$$

The collective eigenmodes coming out of this Hamiltonian are the in- ($|+\rangle$) and out-of-phase ($|-\rangle$) superpositions of the monomeric excitons

$$|+\rangle = \frac{1}{\sqrt{2}}\left(|e_1\rangle + |e_2\rangle\right);\ |-\rangle = \frac{1}{\sqrt{2}}\left(|e_1\rangle - |e_2\rangle\right), \tag{1.7}$$

with energies

$$\epsilon_+ = \epsilon + J;\ \epsilon_- = \epsilon - J. \tag{1.8}$$

Only $|+\rangle$ is optically bright, as the contributions from each monomeric exciton cancel each other for $|-\rangle$. On the other hand, the transition dipole moment of $|+\rangle$ is enhanced compared to the monomeric excitons. Depending on the angle between the transition dipole moments, this sign of J is either positive or negative. In case

of a body-to-body alignment ($\theta > 54.7°$), J will be positive, and the optically bright state will be at higher energies than that of the monomer, while the dark state on the other hand will be at lower energies. This dimer is called an H-dimer, as the optically active state is blue-shifted with respect to that of the monomer. If the alignment resembles a head-to-tail alignment ($\theta < 54.7°$), the sign of J will be negative and the energy of the optically bright state will be below the monomeric exciton energy. This dimer is called J-dimer. The physics of this dimer as the smallest form of molecular aggregates can be extended indefinitely to very large systems. There, the Hamiltonian reads

$$H = \sum_i e_i \left|i\right\rangle \left\langle i\right| + \sum_{i \neq j} J_{ij}(\left|i\right\rangle \left\langle j\right| + h.c.). \tag{1.9}$$

Similarities to the tight-binding Hamiltonian generally used in solid-state physics arise, and in this analogy, an *exciton band* of $|k\rangle$-states forms. If one is to replace the $|+\rangle$ by $|k = 0\rangle$, the sign of the interaction will dictate if the optically bright $|k = 0\rangle$ state will be either on the top or the bottom of the exciton band.
Besides the shift of energy described above, the energetic position of the $|k = 0\rangle$ state has important implications for the emissive properties of the material. Kasha's rule states that the internal relaxation towards the bottom of the exciton band outpaces any other relaxation mechanism. Therefore, in an H-aggregate, where the bright collective exciton sits on the top, excitons will quickly relax into the dark state at the bottom of the band [29]. This effectively quenches the fluorescence of the system. On the other hand, the J-aggregate finds its optically bright state already at the bottom of the band, possessing a significant amount of transition dipole moment. Relaxation via fluorescent radiation becomes highly efficient—an effect termed *superradiance*. Using more sophisticated theories like coherent exciton scattering theory [30], other characteristics of J- and H-aggregation can be derived based on their energetics, such as the reduced Stokes shift between absorption and emission as well as the reduced coupling to vibrations for J-aggregates, while both effects are enhanced for H-aggregates. A graphical illustration of the spectral responses for both J- and H-aggregates can be found in Fig. 1.6.
To this day, the Kasha exciton model is still used as a fundamental theory to under-

stand the optical properties of many molecular aggregates, and J- and H-aggregation are the standard description of many supramolecular systems [23, 31–34].
However, over time more and more molecules were found to aggregate unconventionally, fitting neither the simple J- nor H-aggregation theme. Higher dimensional supramolecular structures like herringbone lattices or chiral stacks gave rise to more complex optical responses, and allowed multiple optically bright states within one aggregate [34–38]. This is especially evident for disordered and non-crystalline aggregates, where the structure remains elusive, necessitating a involved reverse-engineering of the structure-property relationships.
Furthermore, the interaction between nearby dye molecules and their excitons is often not limited to transition dipole moment interactions. Intermolecular charge transfer in particular can lead to efficient coupling between neighboring molecules, while giving rise to a whole new exciton class, the charge transfer (CT) exciton, to be considered in addition to Frenkel excitons.
Intricate three-dimensional structures and competing interactions make realistic predictions about the system at hand difficult. However, it can often be described sufficiently by using the exciton theory and a not-too-complicated, lower-dimensional structure.

1.4 Fundamental Properties of Squaraine Molecules

Squaraine (SQ) molecules are a well-known and versatile class of molecules which absorb strongly ($\epsilon \approx 10^5$ l mol^{-1} cm^{-1}) in the red to infrared region [39]. Together with their high yield and low ecological impact synthesis, their high degree of tunability and a general tendency to aggregate, SQ molecules have been of high interest for a number of applications like dye-sensitized solar cells (efficiency = 4.5%) [40], organic solar cells (efficiency = 8.3%) [41], two-photon absorbing materials, field-effect transistors, light-sensing devices, and photodynamic therapy [42–46]. As the optical transitions of these molecules in their monomeric nature have a sharp and well-defined spectral footprint, they are ideal candidates for investigating the structure-property relationships of their molecular aggregates by optical probes.
The common feature of SQ molecules is the central squaric acid group which acts as an electron acceptor, with a π-conjugated side group on each side acting as elec-

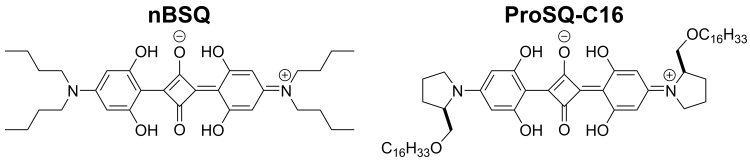

Figure 1.7: Chemical structures of the two squaraine dye molecules investigated in this thesis: nBSQ (left) and ProSQ-C16 (right). The molecules share the same symmetric chromophore in the center of the molecule and are expected to have identical monomeric properties. Note that the shown charge and conjugation sites are only one of the two resonant zwitterionic states. For clarity only the (S, S)-enantiomer of ProSQ-C16 is shown in this figure.

tron donors, yielding a π-conjugated donor-acceptor-donor (D-A-D) structure (see Fig. 1.7). The choice of these donor-groups determines the optical properties of the SQ molecule, like vibronic coupling strength, exciton energy, two-photon absorption efficiency or solvatochromism. Usually, various side groups can be attached beyond the extent of the π-conjugated backbone of a squaraine [47, 48]. These side groups do not alter the optical properties of the individual molecule, but strongly influence how molecules pack in molecular aggregates. The latter is of uttermost importance, as it allows tuning of the optical and excitonic properties of SQ aggregates without the need of changing chromophore, which can be highly beneficial for applications. In this thesis, we will deal with SQ molecules which share the same chromophore and explore their intriguing optical properties which arise solely from the aggregate structure. The structure of the two molecules, 2,4-bis[4-(N,N- dibutylamino)-2,6-dihydroxyphenyl]-squaraine (nBSQ) and 2,4-Bis[4-((S))-(-)-2-(hexadecyloxymethyl)-pyrrolidone-2,6-dihydroxyphenyl]-squaraine (ProSQ-C16), can be seen in Fig. 1.7. The SQ chromophore is built from the squaric core as well as one anniline group on each side, acting as the electron donor. The anniline groups are functionalized with four hydroxy groups on the four carbon atoms closest to the oxygen sites of the squaric core. The hydrogen bonds of the hydroxy group with the center oxygen sides make the molecules backbone rigid and planar and reduces the coupling to vibronic modes [49]. Due to the symmetric D-A-D layout of this chromophore, the *electric* dipole moment cancels out, reducing dipolar coupling to its environment as well as molecular vibrations, resulting in a relatively low Stokes-shift of about 60 meV (see Fig. 1.8). The low coupling strength to vibronic states and the environment results

in a well-defined sharp spectral footprint. This makes this SQ chromophore an ideal candidate to study the effects of aggregation, such as spectral shifts, broadening, and even chiral effects.

In general, sophisticated quantum chemical calculations are needed to properly com-

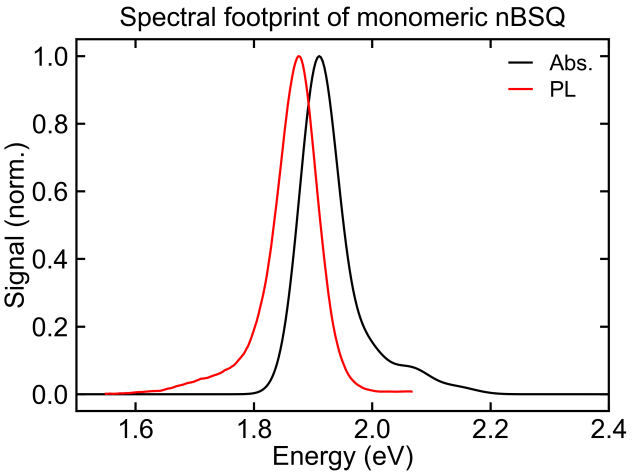

Figure 1.8: Normalized absorbance (black) and photoluminescence (red) spectra of a highly diluted solution of nBSQ in chloroform. Both spectra are dominated by the 0-0 transition, showing only limited coupling to vibronic states. The Stokes-shift between absorbance and photoluminescence peaks is around 60 meV. This relatively small number indicates the low degree of coupling to the solution environment.

pute the wavefunctions of HOMO and LUMO states, as well as their energy levels and related transition dipole moments [50]. However, certain semi-empirical models fitted to experimentally obtained data can yield satisfying results without the need for costly methods. A particularly successful model is the *essential states model*, pioneered by Painelli and coworkers [51]. This model has found success especially with several squaraine molecules and related molecules of similar structure [32, 51–54].

The essential states model makes use of the zwitterionic D-A-D layout of the molecule and considers diabatic states of the system based on the occupation of charge sites. Fig. 1.9 shows how the squaraine backbone is simplified to three charge sites, and the resulting base of states is spanned by the neutral state $|N\rangle$, as well as the two zwitterionic states $|Z_1\rangle$ and $|Z_2\rangle$. To reach the zwitterionic state from the neutral state, an electron transfer from the nitrogen towards the oxygen moieties is needed,

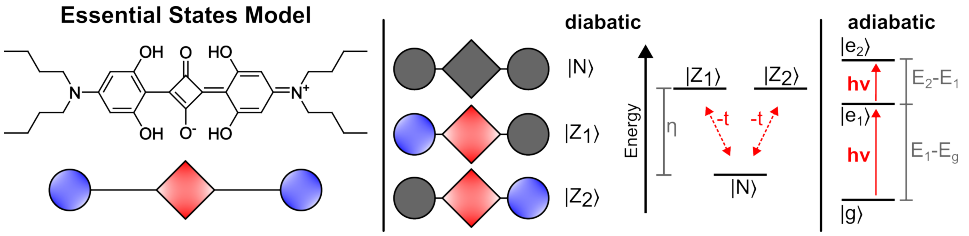

Figure 1.9: The essential states model for nBSQ and related squaraine molecules in general, based on Ref. [32]. The central chromophore can be approximated as three charge sites at the oxygen and nitrogen sites, which can either be occupied (blue represents a hole, red an electron) or not (grey). From these states, three diabatic states emerge: a neutral state ($|N\rangle$), and the two zwitterionic states $|Z_1\rangle$ and $|Z_2\rangle$. The eigenstates of a squaraine molecule can be built from those diabatic states, yielding a ground state $|g\rangle$, an optically bright excited state $|e_1\rangle$ and a two-photon absorptive state $|e_2\rangle$.

parametrized by an *intramolecular* charge transfer integral $-t$. As the second empirical parameter, η is introduced as the energy offset of the zwitterionic states with respect to the neutral state. Based on this basis-set and parameters, the Hamiltonian reads

$$H = \eta \sum_{i=1,2} |Z_i\rangle \langle Z_i| - t \sum_{i=1,2} \left(|N\rangle \langle Z_i| + h.c. \right). \tag{1.10}$$

Diagonalization of this Hamiltonian results in the three eigenstates of the system, usually parametrized by a single, third parameter ρ, which defines the quadrupolar character of the ground state, and can be calculated from the other two parameters $\rho = \frac{1}{2}\left(1 - \frac{\eta}{\sqrt{\eta^2+8t^2}}\right)$. The three eigenstates are

$$\begin{aligned} |g\rangle &= \sqrt{1-\rho}\,|N\rangle + \sqrt{\frac{\rho}{2}}\left(|Z_1\rangle + |Z_2\rangle\right) \\ |e_1\rangle &= \sqrt{\frac{1}{2}}\left(|Z_1\rangle - |Z_2\rangle\right) \\ |e_2\rangle &= \sqrt{\rho}\,|N\rangle - \sqrt{\frac{1-\rho}{2}}\left(|Z_1\rangle + |Z_2\rangle\right) \end{aligned} \tag{1.11}$$

with energies

$$\begin{aligned} E_g &= \rho\eta - 2t\sqrt{2\rho\,(1-\rho)} \\ E_{e_1} &= \eta \\ E_{e_2} &= (1-\rho)\,\eta + 2t\sqrt{2\rho\,(1-\rho)}. \end{aligned} \tag{1.12}$$

Here, $|g\rangle$ is the ground state, $|e_1\rangle$ is the first, optically bright excited state, and $|e_2\rangle$ the two-photon active second excited state. For the SQ chromophore of ProSQ-C16 and nBSQ, the parameters have a value of $\eta = 0.69$ eV and $t = 1.05$ eV [32], resulting in $\rho = 0.39$, which is classified as a chromophore of intermediate quadrupolar moment [51].
Therefore, the optical and excitonic properties of this chromophore are given by three states carrying significant electric quadrupolar moment without any electric dipole moment. Since only the first excited state is optically bright, the system at hand can be approximated as a two-level system molecule ($|g\rangle, |e_1\rangle$), which makes simulating the optical properties of different aggregate structures using simple models feasible. These models will be introduced in the second part of the next chapter.

1.5 Scope of the Thesis

Chapter 1 introduces organic dye molecules and principles of transient absorption spectroscopy, as well as the origin of the optical properties of squaraine molecules, π-conjugated molecules in general, and molecular aggregates.
Chapter 2 will introduce the experimental and simulation methods used in this thesis. For the experimental methods, the physical effects and working principles are described, as well as schematics of the most important parts in each experimental setup. The structural models and theory part describes how to parametrize the structure of an aggregate, its Hamiltonian, and how to calculate various optical spectra from it.
In chapter 3, we apply these methods to the extraordinary aggregated thin films of the highly symmetric squaraine molecule nBSQ. The exotic absorption spectrum, which features panchromaticity, defies standard exciton theory, and was previously only modelled under the consideration of intermolecular charge transfer in a dimer

system [32]. We employ ultrafast transient absorption spectroscopy for the first time to this system and simulate both the steady-state and transient absorption spectra under the consideration of structural disorder inside the aggregate as opposed to an ordered, crystalline structure. The exceptional agreement of experiment and theory suggests that structural disorder alone has the power to alternate the absorption spectra of molecules after aggregation tremendously, and that it can be used to tailor and optimize the optical properties of molecular aggregates in thin films for optoelectronic applications. This study has been published in the *Journal of the American Chemical Society* [23].

Chapter 4 is concerned with the transient footprint of intermolecular charge transfer states and charge separation in nBSQ aggregates adopting the double hump absorption spectrum. We perform ultrafast transient absorption spectroscopy on both a pristine nBSQ thin film and a blend of nBSQ and the electron acceptor $PC_{61}BM$ to monitor the charged state dynamics between PCBM and nBSQ. A photoinduced Stark effect gives rise to a sizable electroabsorption signal in both samples. To the best of our knowledge, this marks the first time photoinduced electroabsorption is reported in a single-chromophore system. The electroabsorption signal arises from both the intermolecular charge transfer inside the nBSQ aggregate, as well as charge separation at the interface of nBSQ and PCBM. This signal is dominating the transient response for delay times longer than the Frenkel exciton lifetime ($\approx$ 200 ps), showing that intermolecular charge transfer states are essential to understand the optical properties of nBSQ aggregates beyond steady-state absorption. Furthermore, we could show that the blend film features a fast sub-picosecond charge separation rate at the interface of the two components, conforming a delocalized-wave function driven charge separation mechanism [55, 56].

Chapters 5 and 6 are concerned with another squaraine molecule, ProSQ-C16, which consists of the same chromophore as nBSQ, but is known for its tremendously strong coupling to circularly polarized light [57] and an equally non-trivial optical response. Theory predicts several structures to explain the exotic linear and circular dichroic properties, including different interactions like intermolecular charge transfer or a multitude of optically active aggregates [33]. We conduct utrafast transient absorption spectroscopy to reveal the structural nature of both enantiopure, chiral aggregates as well as racemic thin films, which do not show any sign of chirality. Our

measurements strongly suggest that a single type of aggregate is responsible for the multiple absorption peaks present for the enantiopure films, and that intermolecular charge transfer might be the origin. Analysis of the dynamics further suggests that the lack of fluorescence from ProSQ-C16 thin films comes from a fast and efficient decay into an intermediate dark state, possibly due to a conical intersection.
Chapter 6 is a theoretical investigation into the linear optical properties of enantiopure ProSQ-C16 thin films and is showcasing how different structural models can predict the chiroptical properties depending on the interactions considered. Our simulations show that the chiroptical properties of ProSQ-C16 thin films can be qualitatively accounted for by two coexisting large chiral aggregate structures, even if only Frenkel excitons are considered. In line with previous theoretical assumptions [33, 58], we could further show that a single large size molecular aggregate can also describe the optical properties of the thin film, if intermolecular charge transfer is considered. Our study underlines the importance of lightweight modelling, as large-scale chiral structures cannot easily be considered using more sophisticated methods such as the essential states model.

References

(1) Park, J.-S.; Chae, H.; Chung, H. K.; Lee, S. I. *Semiconductor Science and Technology* **2011**, *26*, 034001.

(2) Salehi, A.; Fu, X.; Shin, D.-H.; So, F. *Advanced Functional Materials* **2019**, *29*, 1808803.

(3) Bauri, J.; Choudhary, R. B.; Mandal, G. *Journal of Materials Science* **2021**, *56*, 18837–18866.

(4) Krause, G. H.; Weis, E. *Annual Review of Plant Physiology and Plant Molecular Biology* **1991**, *42*, 313–349.

(5) Rabinowitch, E. I.; Govindjee *Scientific American* **1965**, *213*, 74–83.

(6) Abraham, N. G.; Lin, J. H. .-; Schwartzman, M. L.; Levere, R. D.; Shibahara, S. *International Journal of Biochemistry* **1988**, *20*, 543–558.

(7) Goldberg, M. A.; Dunning, S. P.; Bunn, H. F. *Science* **1988**, *242*, 1412–1415.

(8) Travis, A. S. *Technology and Culture* **1990**, *31*, 51–82.

(9) Chiang, C. K.; Fincher, C. R.; Park, Y. W.; Heeger, A. J.; Shirakawa, H.; Louis, E. J.; Gau, S. C.; MacDiarmid, A. G. *Physical Review Letters* **1977**, *39*, 1098–1101.

(10) Green, M. A.; Emery, K.; Hishikawa, Y.; Warta, W. *Progress in Photovoltaics: Research and Applications* **2010**, *18*, 144–150.

(11) Green, M. A.; Hishikawa, Y.; Warta, W.; Dunlop, E. D.; Levi, D. H.; Hohl-Ebinger, J.; Ho-Baillie, A. W. *Progress in Photovoltaics: Research and Applications* **2017**, *25*, 668–676.

(12) Green, M. A.; Dunlop, E. D.; Yoshita, M.; Kopidakis, N.; Bothe, K.; Siefer, G.; Hao, X. *Progress in Photovoltaics: Research and Applications* **2023**, *31*, 651–663.

(13) Chamberlain, G. A. *Solar Cells* **1983**, *8*, 47–83.

(14) Wöhrle, D.; Meissner, D. *Advanced Materials* **1991**, *3*, 129–138.

(15) Hoppe, H.; Sariciftci, N. S. *Journal of Materials Research* **2004**, *19*, 1924–1945.

(16) Brabec, C. J.; Sariciftci, N. S.; Hummelen, J. C. *Advanced Functional Materials* **2001**, *11*, 15–26.

(17) Sampaio, P. G. V.; González, M. O. A. *International Journal of Energy Research* **2022**, *46*, 17813–17828.

(18) Würfel, U.; Herterich, J.; List, M.; Faisst, J.; Bhuyian, M. F. M.; Schleiermacher, H.-F.; Knupfer, K. T.; Zimmermann, B. *Solar RRL* **2021**, *5*, 2000802.

(19) Yan, C.; Barlow, S.; Wang, Z.; Yan, H.; Jen, A. K.-Y.; Marder, S. R.; Zhan, X. *Nature Reviews Materials* **2018**, *3*, 1–19.

(20) Zhou, R.; Jiang, Z.; Yang, C.; Yu, J.; Feng, J.; Adil, M. A.; Deng, D.; Zou, W.; Zhang, J.; Lu, K.; Ma, W.; Gao, F.; Wei, Z. *Nature Communications* **2019**, *10*, 5393.

(21) Yang, J.; Yan, D.; Jones, T. S. *Chemical Reviews* **2015**, *115*, 5570–5603.

(22) Bakalis, L. D.; Knoester, J. *The Journal of Physical Chemistry B* **1999**, *103*, 6620–6628.

(23) Bernhardt, R.; Manrho, M.; Zablocki, J.; Rieland, L.; Lützen, A.; Schiek, M.; Meerholz, K.; Zhu, J.; Jansen, T. L. C.; Knoester, J.; van Loosdrecht, P. H. M. *Journal of the American Chemical Society* **2022**, *144*, 19372–19381.

(24) Atkins, P.; de Paula, J.; Keeler, J. *Atkins' Physical Chemistry, 12th Edition* **2022**.

(25) Castro Neto, A. H.; Guinea, F.; Peres, N. M. R.; Novoselov, K. S.; Geim, A. K. *Reviews of Modern Physics* **2009**, *81*, 109–162.

(26) Kasha, M.; Rawls, H. R.; Ashraf El-Bayoumi, M. *Pure and Applied Chemistry* **1965**, *11*, 371–392.

(27) Scheibe, G. *Angewandte Chemie* **1937**, *50*, 212–219.

(28) Jelley, E. E. *Nature* **1936**, *138*, 1009–1010.

(29) Kasha, M. *Discussions of the Faraday Society* **1950**, *9*, 14–19.

(30) Eisfeld, A.; Briggs, J. S. *Chemical Physics* **2006**, *324*, 376–384.

(31) Spano, F. C.; Silva, C. *Annual Review of Physical Chemistry* **2014**, *65*, 477–500.

(32) Hestand, N. J.; Zheng, C.; Penmetcha, A. R.; Cona, B.; Cody, J. A.; Spano, F. C.; Collison, C. J. *The Journal of Physical Chemistry C* **2015**, *119*, 18964–18974.

(33) Giavazzi, D.; F. Schumacher, M.; Grisanti, L.; Anzola, M.; Maiolo, F. D.; Zablocki, J.; Lützen, A.; Schiek, M.; Painelli, A. *Journal of Materials Chemistry C* **2023**, *11*, 8307–8321.

(34) Hestand, N. J.; Spano, F. C. *Accounts of Chemical Research* **2017**, *50*, 341–350.

(35) Lindorfer, D.; Renger, T. *The Journal of Physical Chemistry B* **2018**, *122*, 2747–2756.

(36) Chen, H.; Farahat, M. S.; Law, K.-Y.; Whitten, D. G. *Journal of the American Chemical Society* **1996**, *118*, 2584–2594.

(37) Gierschner, J.; Park, S. Y. *Journal of Materials Chemistry C* **2013**, *1*, 5818–5832.

(38) De Rossi, U.; Dähne, S.; Meskers, S. C. J.; Dekkers, H. P. J. M. *Angewandte Chemie International Edition in English* **1996**, *35*, 760–763.

(39) Chen, G.; Sasabe, H.; Igarashi, T.; Hong, Z.; Kido, J. *Journal of Materials Chemistry A* **2015**, *3*, 14517–14534.

(40) Yum, J.-H.; Walter, P.; Huber, S.; Rentsch, D.; Geiger, T.; Nüesch, F.; De Angelis, F.; Grätzel, M.; Nazeeruddin, M. K. *Journal of the American Chemical Society* **2007**, *129*, 10320–10321.

(41) Zimmerman, J. D.; Lassiter, B. E.; Xiao, X.; Sun, K.; Dolocan, A.; Gearba, R.; Vanden Bout, D. A.; Stevenson, K. J.; Wickramasinghe, P.; Thompson, M. E.; Forrest, S. R. *ACS Nano* **2013**, *7*, 9268–9275.

(42) De Miguel, G.; Ziółek, M.; Zitnan, M.; Organero, J. A.; Pandey, S. S.; Hayase, S.; Douhal, A. *The Journal of Physical Chemistry C* **2012**, *116*, 9379–9389.

(43) Beverina, L.; Salice, P. *European Journal of Organic Chemistry* **2010**, *2010*, 1207–1225.

(44) Schulz, M.; Balzer, F.; Scheunemann, D.; Arteaga, O.; Lützen, A.; Meskers, S. C. J.; Schiek, M. *Advanced Functional Materials* **2019**, *29*, 1900684.

(45) Gsänger, M.; Kirchner, E.; Stolte, M.; Burschka, C.; Stepanenko, V.; Pflaum, J.; Würthner, F. *Journal of the American Chemical Society* **2014**, *136*, 2351–2362.

(46) Avirah, R. R.; Jayaram, D. T.; Adarsh, N.; Ramaiah, D. *Organic & Biomolecular Chemistry* **2012**, *10*, 911–920.

(47) Zablocki, J.; Schulz, M.; Schnakenburg, G.; Beverina, L.; Warzanowski, P.; Revelli, A.; Grüninger, M.; Balzer, F.; Meerholz, K.; Lützen, A.; Schiek, M. *The Journal of Physical Chemistry C* **2020**, *124*, 22721–22732.

(48) Schulz, M.; Mack, M.; Kolloge, O.; Lützen, A.; Schiek, M. *Physical Chemistry Chemical Physics* **2017**, *19*, 6996–7008.

(49) Timmer, D.; Zheng, F.; Gittinger, M.; Quenzel, T.; Lünemann, D. C.; Winte, K.; Zhang, Y.; Madjet, M. E.; Zablocki, J.; Lützen, A.; Zhong, J.-H.; De Sio, A.; Frauenheim, T.; Tretiak, S.; Lienau, C. *Journal of the American Chemical Society* **2022**, *144*, 19150–19162.

(50) Grimme, S.; Hansen, A.; Brandenburg, J. G.; Bannwarth, C. *Chemical Reviews* **2016**, *116*, 5105–5154.

(51) Terenziani, F.; Painelli, A.; Katan, C.; Charlot, M.; Blanchard-Desce, M. *Journal of the American Chemical Society* **2006**, *128*, 15742–15755.

(52) Sissa, C.; Terenziani, F.; Painelli, A.; Abbotto, A.; Bellotto, L.; Marinzi, C.; Garbin, E.; Ferrante, C.; Bozio, R. *The Journal of Physical Chemistry B* **2010**, *114*, 882–893.

(53) D'Avino, G.; Terenziani, F.; Painelli, A. *The Journal of Physical Chemistry B* **2006**, *110*, 25590–25592.

(54) Shafeekh, K. M.; Das, S.; Sissa, C.; Painelli, A. *The Journal of Physical Chemistry B* **2013**, *117*, 8536–8546.

(55) Tamai, Y.; Fan, Y.; Kim, V. O.; Ziabrev, K.; Rao, A.; Barlow, S.; Marder, S. R.; Friend, R. H.; Menke, S. M. *ACS Nano* **2017**, *11*, 12473–12481.

(56) Jakowetz, A. C.; Böhm, M. L.; Zhang, J.; Sadhanala, A.; Huettner, S.; Bakulin, A. A.; Rao, A.; Friend, R. H. *Journal of the American Chemical Society* **2016**, *138*, 11672–11679.

(57) Schulz, M.; Zablocki, J.; Abdullaeva, O. S.; Brück, S.; Balzer, F.; Lützen, A.; Arteaga, O.; Schiek, M. *Nature Communications* **2018**, *9*, 2413.

(58) Manrho, M.; Jansen, T. L. C.; Knoester, J. *The Journal of Chemical Physics* **2022**, *156*, 224112.

Chapter 2

Methods

This chapter provides an introduction to the experimental and theoretical methods used in this thesis. Both steady-state absorption and photoluminescence spectroscopy will be introduced along with the experimental realization of ultrafast transient absorption spectroscopy in the lab. In the end, the theoretical framework used to simulate the optical properties of various aggregates is discussed, guiding the reader through the buildup of each model.

2.1 Experimental Techniques

Optical spectroscopy techniques are essential for characterization of organic dye molecules in all kinds of media, from gas-phase to condensed matter. In this thesis, several fundamental and advanced techniques were conducted. Two of the most used methods, absorption spectroscopy (commonly referred to as "UV-Vis") and photoluminescence spectroscopy will be used in this thesis to gain information on fundamental excitonic and structural properties.

2.1.1 Steady-State Absorption Spectroscopy

Steady-state absorption spectroscopy is one of the most widely used types of optical spectroscopy and often used as the experiment of choice for sample validation and characterization. It is possible to connect transmitted light intensities to the absorptive properties of a sample using the Beer-Lambert law, which reads:

$$I(\omega) = I_0(\omega) \cdot 10^{-\epsilon(\omega)\cdot c\cdot d} = I_0(\omega) \cdot 10^{-A(\omega)}. \tag{2.1}$$

Here, $I_0(\omega)$ and $I(\omega)$ describe the incoming and transmitted light intensity of a given frequency ω, $\epsilon(\omega)$ is the extinction coefficient, an intrinsic material property, c is the concentration of the sample, and d the optical path through the sample. The absorbance A can be calculated knowing I_0 and I using:

$$A(\omega) = log_{10}\left(\frac{I_0}{I}\right). \tag{2.2}$$

Both observables $A(\omega)$ and $\epsilon(\omega)$ provide important information about our sample, mainly the light-matter interaction strength and the number of different optically active states. The light matter interaction strength of a given material depends on its (electronic) transitions, each with a given frequency ω and oscillator strength f, which in turn depends on both ω and the transition dipole moment μ

$$A(\omega) \propto \epsilon(\omega) \propto f \propto \mu^2\omega. \tag{2.3}$$

Therefore, we can access the amplitude of the transition dipole moment of a given transition by measuring its absorbance.
Unless mentioned otherwise, steady-state absorbance spectra shown in this thesis originated from a Lambda 1050 absorption spectrometer (PerkinElmer). A description of the key components of the spectrometer and more generally absorption spectrometers is given below.
The experimental setup used to measure the absorbance as a spectrum consists of only a few functional parts:

- A broadband UV/visible (Vis)/near infrared (NIR) light source;
- A dispersive element;
- A detector unit.

As a light source, a tungsten halogen lamp is used, which yields a wider spectrum than most LEDs and other light sources. As its spectrum is constricted to the NIR and Vis regions, an additional Deuterium lamp is used to extend the range down to 200 nm.
As a dispersive element, diffraction gratings are chosen. For light sources with extremely broad spectra, multiple gratings might be used.
The material of choice for visible and low energy UV light detectors is Silicon, either in a CCD or CMOS architecture consisting of an array of pixels, on which different photon wavelengths are mapped using the dispersive element. This allows wavelength or energy-resolved light intensity detection, from which the absorbance spectrum can be calculated. To extend the spectral range of the spectrometer towards the NIR region, different detectors based on semiconductors like InGaAs and PbS can be used complementary to the Silicon detector. Photomultiplyer tubes can also be used to increase signal-to-noise ratio and extend the UV detection range.

2.1.2 Steady-State Photoluminescence Spectroscopy

Photoluminescence describes the emissive relaxation processes of a material after photoexcitation. This emission can be categorized into two concepts, namely fluorescence and phosphorescence. Fluorescence usually describes the direct radiative

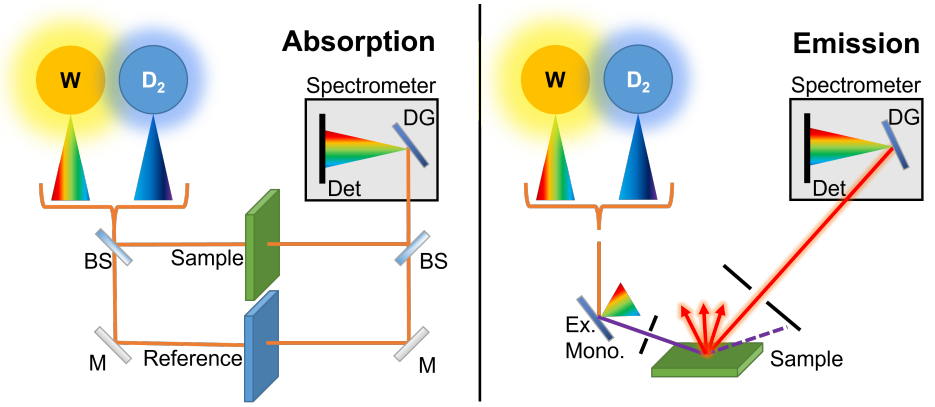

Figure 2.1: Absorption (left) and photoluminescence (right) spectroscopy layouts.

recombination of the initially excited singlet state back to the singlet ground state, $S_1 \xrightarrow{\hbar\omega} S_0$. This transition happens immediately after photoexcitation, usually in the timescale of nanoseconds [1].

For phosphorescence, the system first undergoes intersystem crossing (ISC), converting the singlet excited state into a triplet excited state. As the relaxation back to the singlet ground state is spin-forbidden, the radiative relaxation process happens on much longer time scales, from milliseconds to hours ($S_1 \xrightarrow{ISC} T_1 \xrightarrow{\hbar\omega} S_0$).

To measure the photoluminescent emission, a setup similar to the absorption spectroscopy setup is needed. For excitation, a (tunable) monochromatic light source is needed, which is typically achieved by using a broadband light source coupled to a monochromator, which consists of a dispersive medium and a slit, or a laser. The monochromatic light is then guided to the sample. The outcoming emission is then collected from an angle other than the reflection angle, as spontaneous emission is quasi-isotropic. Alternatively, an integration sphere can be used to collect all emitted photons. In any case the photons are guided to a dispersive medium, usually a diffraction grating, followed by a detection unit, which should have a high degree of sensitivity to detect even faintly emissive signals.

For the projects discussed in this thesis, photoluminescence spectra were recorded on a LS-55 fluorescence spectrometer (PerkinElmer), which offers monochromatic excitation wavelengths between 200 nm and 800 nm. The emission spectrum can be collected between 400 nm and 900 nm. The spectrometer can host both solid-state

thin film samples as well as solution samples.

2.1.3 Transient Absorption Spectroscopy

The concept of transient absorption spectroscopy has been addressed in chapter 1. In the following, we will deal with the realization of transient absorption spectroscopy in the lab and how the setup used in this thesis is working.
All transient absorption data shown in this thesis were recorded using a customized

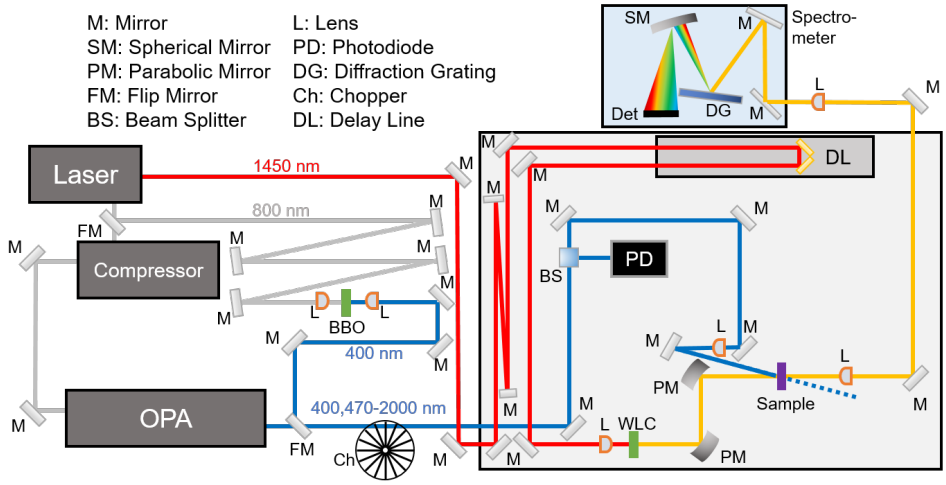

Figure 2.2: Simplified layout of the transient absorption setup used in this work.

transient absorption setup [2]. A functional sketch of the most important components can be seen in Fig. 2.2. This setup is based on a Yb:KGW regenerative amplifier laser system (PHAROS, Light Conversion) with an integrated OPA, producing three pulsed (ca. 160 fs) output beams with wavelengths of 513, 800 and 1445 nm. The 800 nm line is used for generating the pump pulse in our experiments. This can be achieved by doubling the frequency in a β-BBO crystal to 400 nm using second harmonic generation, or by compressing the pulse to ca. 40 fs before feeding it into an optical parametric amplifier (OPA) (TOPAS, LightConversion). The OPA generates tunable wavelengths from 470-2000 nm by four-wave mixing of white-light pulses with the high intensity 800 nm beam. The output from either the OPA or the BBO is then sent through a chopper wheel and into the spectrometer setup (HARPIA, LightConversion), together with the 1445 nm line, which will be used to generate

the probe line. The 400 nm line features an artificially prolonged optical path to compensate the long optical path of the OPA line.
Inside the HARPIA box, the 1445 nm probe line is sent through an artificially prolonged beam path before entering the delay line, which controls the time delay between pump and probe. The delay line has a maximum optical path of around 60 cm, which corresponds to a delay of 2000 ps or 2 ns. After passing through the delay line, the beam is sent into a white light (WL) generating crystal (sapphire). The beam is focused tightly on the white light generating crystal to allow non-linear optical effects to happen. In particular, the infrared pulse changes the refractive index of the crystal, allowing the pulse to interact with itself, leading to self-phase-modulation, four-wave-mixing and modulational instability, which broadens the spectrum to a supercontinuum. This supercontinuum spans the most part of the visible and NIR spectrum, with a maximum intensity around 600 nm (see Fig. 2.3). This white light probe is directed and focused onto the sample using two parabolic mirrors with a focus spot of around 80 µm in diameter. The pump pulse is focused to spatially overlap with the probe spot, but with a larger diameter to ensure homogeneous excitation conditions on the probe spot area. The probe beam is then collimated and sent to the detector, while the pump is dumped into a blocker. The detector unit consists of a diffraction grating and a CCD detector array, which reads out the data at a rate of 1 kHz. To correct for scattering contributions from both pump and probe, the transient data is collected by measuring four intensity spectra.

$$\Delta A = \frac{I_p - I_{p,dark}}{I_u - I_{u,dark}}. \tag{2.4}$$

Here, p/u refers to pumped or unpumped intensity spectra, while *dark* refers to the spectrum without probe pulse. To further minimize the scattering contributions from the pump, it can be polarized perpendicular to the probe and filtered out using a linear polarizer. The reference of *pumped* and *unpumped* is obtained by a photodiode.
This setup has multiple advantages. The white light supercontinuum allows a much more comprehensive understanding of the spectral dynamics than regular two-color pump-probe spectroscopy can. Because of the high repetition rate of up to 150 kHz, the signal-to-noise ratio of this setup is extraordinarily high, and measurements can

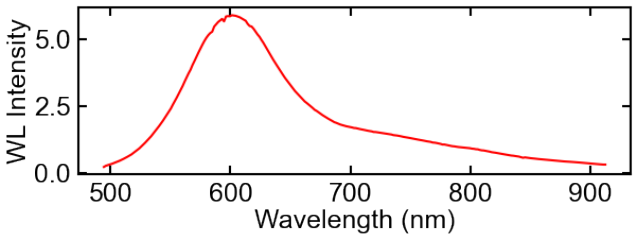

Figure 2.3: Exemplary spectrum of the white light (WL) supercontinuum spectrum used as a probe in ultrafast transient absorption spectroscopy.

be conducted in a rapid manner, allowing measurements of samples which are stable only on the hour scale with a noise floor of around 0.01 mOD. Moreover, the already impressive wavelength range covered by white light can be further explored in the NIR region by another, InGaAs-based detector.
For sample handling, several upgrades have been added to the original design. For spatial resolution, a motorized x-y-z-stage has been added, which allows for automated measurements using a python script.
As the intensity of light is excessive in these experiments, many molecules in solution will suffer from degradation if exposed to pump and probe for too long. To reduce the exposure time of solution samples, a flow-cell has been installed with a peristaltic pump, reducing the exposure per molecule drastically.

2.2 Structural Models and Theory

In the following, we will introduce the reader to the models used to simulate the optical properties of molecular aggregates. The simulation process can be divided into three parts:

1. Structure;
2. Hamiltonian;
3. Spectrum.

In section 2.2.1 we discuss how several aggregate structures relevant for nBSQ and ProSQ-C16 molecules can be parametrized. Section 2.2.2 is concerned with the intermolecular interactions considered for different Hamiltonians and how the structure

affects them. Finally, in section 2.2.3 we present how eigenstates of a given Hamiltonian can be converted into different optical spectra.

2.2.1 Structure

Choosing the aggregate structure is the most important task during the simulation, as it dictates the structure-property relationships. Depending on the aggregate at hand, different parametrizations might be used to quantify the three-dimensional position of each molecule as well as its orientation. For this thesis, two structures are of particular importance: the one-dimensional disordered aggregate chain and the chiral helix aggregate.
The details of the one-dimensional disordered chain aggregate model can be found in chapter 3; nevertheless, we will give a brief overview here. In essence, the model is simplified, as all molecules are assumed to be parallel, with their transition dipole moments directed perpendicular to the extent of the chain. Additionally, only Coulombic (transition dipole moment) interaction in the point dipole approximation is considered, reducing the required number of simulation parameters tremendously. Hence, all structural information needed is the position of each molecule, straightforwardly parametrized as Δx, Δy, and Δz. As the construction of this aggregate follows an iterative procedure (see chapter 3 for details), the only other number needed to parametrize a given aggregate is the number of molecules inside the aggregate, N.
For the helix, the structural information is even more important, as the geometry of the system is directly related to the circular dichroic properties [3]. On top of that, the orientation of the molecules continuously rotates around the aggregate axis, yielding strongly anisotropic polarization dependencies. Due to this rotation, Cartesian coordinates are suboptimal. Instead, the aggregate can be parametrized in cylindrical coordinates, using the distance between nearest neighboring molecules (Δz), their twisting angle (α), as well as half of the extent of their π-conjugation (Δl), as sketched in Fig. 2.4. Using half of the π-conjugated extent is a more convenient choice for later calculation. Since the construction of the aggregate follows an iterative procedure as well, the only other parameter needed here is again the number of molecules in the structure (N). The helix structure can be further altered

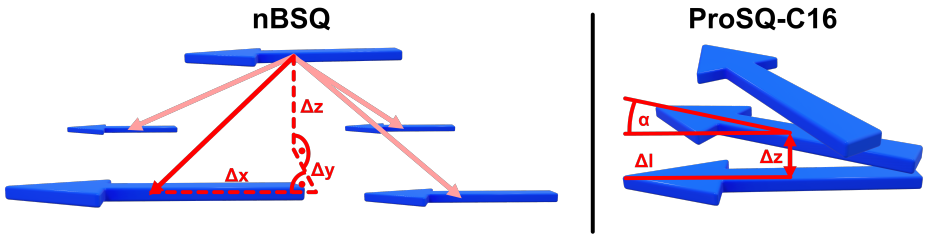

Figure 2.4: Sketch of the structures considered in this study. For nBSQ (left), the disordered aggregate structure is built iteratively given the three cartesian translation vector coordinates Δx, Δy, and Δz. For ProSQ-C16 (right) the nearest neighbor alignment is parametrized by the π-conjugation length 2Δl, the twist angle α and the nearest neighbor distance Δz.

to form a "creeper" structure. Parametrization of this structure will be discussed in detail in chapter 6.

From those parameters, a structure file can be built, which stores the three-dimensional coordinates of center-of-mass as well as the tips of the π-conjugated part for all molecules. Conveniently, these three positions of each molecule coincide with the position of the electron-donating oxygen sites in the center and the nitrogen moieties on the edge, which becomes important for both the Coulombic interactions as well as charge hopping.

The parametrized structure allows us to calculate helical properties, which are based on the geometry of the system and mediated through the rotation strength R_{ij}, which gives a measure for the twistedness of molecular alignments. It can be calculated using

$$R_{ij} \propto (\vec{\mu}_i \times \vec{\mu}_j) \cdot (\vec{r}_i - \vec{r}_j). \tag{2.5}$$

Here, $\vec{\mu_i}$ is the transition dipole moment vector, which can be substituted by the vector connecting the two nitrogen sites of a given molecule. $\vec{r_i}$ is the position of the center of mass of the respective molecule.

2.2.2 Hamiltonian

For the Hamiltonian two different basis-sets can be utilized, depending on whether ICT is considered or not.
In the first consideration, we use only Frenkel-states, and interaction is mediated solely via transition dipole moment interactions (H_J). This yields the well-known Frenkel-Hamiltonian in an on-site basis,

$$H = H_0 + H_J, \tag{2.6}$$

$$H = \sum_i e_i \left|i\right\rangle \left\langle i\right| + \sum_{i \neq j} J_{ij}(\left|i\right\rangle \left\langle j\right| + h.c.). \tag{2.7}$$

The state $\left|i\right\rangle$ represents an excited molecule i, while all other molecules are not excited. e_i is the excitation energy of site i, and J_{ij} is the interaction energy between transition dipole moments. Note that generally, we can fix all excitation energies e_i to a constant, or even zero. Static disorder can be introduced by adding a random variance to the fixed energy ($e_i = e + \delta_i$).
J can be calculated using different approximations. The first and most used approximation is the point dipole approximation (PDA), where both transition dipole moments of length l and distance z interact in the limit of $l \ll z$. In this limit, the interaction energy can be calculated as

$$J_{ij}^{PDA} = \frac{\vec{\mu}_i \cdot \vec{\mu}_j - 3(\vec{\mu}_i \cdot \vec{R})(\vec{\mu}_j \cdot \vec{R})}{4\pi\epsilon\epsilon_0 |\vec{R}|^3}. \tag{2.8}$$

$\vec{R}$ is the distance between the point dipoles collapsing at the center-of-mass of each molecule, while ϵ is the permittivity of the material, and ϵ_0 is the dielectric constant. μ_i denotes the transition dipole moment of the i-th molecule. While this is a useful approximation due to its simplicity, it breaks down when the extent of a dipole moment ($\approx$ extent of π-conjugation) becomes significant compared to the distance z (l $\approx$ z). As a close packed system is a prerequisite for strong molecular interactions as well as charge transfer, we use a slightly more complicated, but more realistic extended dipole approximation (EDA). In EDA, we assign "transition charges" at the ends of the transition dipole moment and calculate the interaction of these proxy

point charges using

$$J_{ij}^{EDA} = \frac{1}{4\pi\epsilon\epsilon_0}\left(\frac{q_i^+ q_j^+}{r_i^+ - r_j^+} - \frac{q_i^- q_j^+}{r_i^- - r_j^+} - \frac{q_i^+ q_j^-}{r_i^+ - r_j^-} + \frac{q_i^- q_j^-}{r_i^- - r_j^-}\right) \tag{2.9}$$

$q_i^{\pm}$ represents the absolute of the transition charge on the positive or negative end of the dipole with the respective position $r_i^{\pm}$. As these positions are known from the structure file, interactions can be easily calculated, and its components added to the Hamiltonian matrix. Note that the transition point charges are a simplified point-like approximation of the transition charge density.
Adding intermolecular charge transfer (ICT) to the Hamiltonian requires a different basis set. A convenient basis set is the extension of the exciton basis states $|i\rangle$ into the charge basis states $|i^+, j^-\rangle$, where i and j index the molecule containing the hole and electron, respectively. $i = j$ corresponds to a Frenkel state, which enters the Hamiltonian as described above. Including ICT states ($i \neq j$) demands an extension of the Hamiltonian into five components:

$$H = H_0 + H_J + H_P + H_{et} + H_{ht}. \tag{2.10}$$

Next to the Frenkel Hamiltonian, the Hamiltonian H_P describes the ICT energies, considering the separated charge states as polarons rather than unscreened charges. Electron and hole hopping is accounted for in Hamiltonian H_{et} and (H_{ht}), respectively. In the charge basis set, the Hamiltonian can be written as

$$\begin{aligned} H = &\sum_i e_i \left|i,i\right\rangle \left\langle i,i\right| + \sum_{i\neq k} J(\left|ii\right\rangle \left\langle kk\right| + h.c.) + \sum_{i\neq j} e_{ij}^p \left|i,j\right\rangle \left\langle i,j\right| \\ &- \sum_{i,j} t_e(\left|i,j\pm 1\right\rangle \left\langle i,j\right| + h.c.) - \sum_{i,j} t_h(\left|i\pm 1,j\right\rangle \left\langle i,j\right| + h.c.). \end{aligned} \tag{2.11}$$

Three new parameters emerge here: the polaron energy e_{ij}^p and the charge hopping parameters t_e and t_h. The polaron energy itself consists of the energy of two polaronic states as well as their Coulomb attraction, which can be calculated as

$$e_{ij}^p = e^p - \frac{e^2}{4\pi\epsilon}\frac{1}{r_i - r_j} = e^p - \epsilon'\frac{1}{i-j}. \tag{2.12}$$

ϵ' describes the effective depth of the Coulomb well, which controls the energy spacing between ICT states of various electron-hole-distances; e^p is the energy of the polaron pair.
After the full Hamiltonian has been parametrized, we gain access to the eigenstates Ψ_k, eigenenergies ω_k and wavefunction coefficients c_{ik} by employing straight-forward numerical diagonalization.

2.2.3 Spectrum

Based on the eigenstates $\Psi_k = \sum_i c_{ik} |i\rangle$ of the system, we can calculate three different spectra: density of states, absorbance, and circular dichroism. All spectra can be obtained either as a precise stick spectrum or as a more realistic spectrum using a line shape function $L(\omega)$. Since we calculate single excitonic states, a Lorentzian line shape has been chosen to calculate the spectrum.
The density of states spectrum can be calculated straightforwardly by summing over all eigenstates

$$\rho(\omega) = \sum_k L(\omega - \omega_k). \tag{2.13}$$

In order to calculate linear absorbance spectra of a certain polarization $\vec{a}$, we need to calculate the projection of the transition dipole moment onto that axis:

$$A_a(\omega) = \sum_k \left(\left(\sum_i c_{ik} \cdot \vec{\mu}_i \right) \cdot \vec{a} \right)^2 L(\omega - \omega_k). \tag{2.14}$$

Here, c_{ik} is the coefficient of eigenstate k on site i. This parameter also enters the formula for the circular dichroism, together with the rotation strength mentioned above

$$CD(\omega) = \sum_k \left(\sum_{i,j} c_i c_j R_{ij} \right) L(\omega - \omega_k). \tag{2.15}$$

Note that this formula represents the isotropic CD spectrum [3], which considers the average CD response of isotropically distributed chiral structures.

References

(1) Berezin, M. Y.; Achilefu, S. *Chemical Reviews* **2010**, *110*, 2641–2684.

(2) Jung, E.; Budzinauskas, K.; Öz, S.; Ünlü, F.; Kuhn, H.; Wagner, J.; Grabowski, D.; Klingebiel, B.; Cherasse, M.; Dong, J.; Aversa, P.; Vivo, P.; Kirchartz, T.; Miyasaka, T.; van Loosdrecht, P. H. M.; Perfetti, L.; Mathur, S. *ACS Energy Letters* **2020**, *5*, 785–792.

(3) Lindorfer, D.; Renger, T. *The Journal of Physical Chemistry B* **2018**, *122*, 2747–2756.

Chapter 3

Structural Disorder as the Origin of Optical Properties and Spectral Dynamics in Squaraine Nano-Aggregates

In contrast to regular J- and H-aggregates, thin film squaraine aggregates usually have broad absorption spectra containing both J-and H-like features, which are favorable for organic photovoltaics. Despite being successfully applied in organic photovoltaics for years, a clear interpretation of these optical properties by relating them to specific excited states and an underlying aggregate structure has not been made. In this work, by static and transient absorption spectroscopy on aggregated n-butyl anilino squaraines, we provide evidence that both the red- and blue-shifted peaks can be explained by assuming an ensemble of aggregates with intermolecular dipole-dipole resonance interactions and structural disorder deriving from the four different nearest neighbor alignments-in sharp contrast to previous association of the peaks with intermolecular charge-transfer interactions. In our model, the next-nearest neighbor dipole-dipole interactions may be negative or positive, which leads to the occurrence of J- and H-like features in the absorption spectrum. Upon femtosecond pulse excitation of the aggregated sample, a transient absorption spectrum deviating from the absorbance spectrum emerges. The deviation finds its origin in the excitation of two-exciton states by the probe pulse. The lifetime of the exciton is confirmed by the band integral dynamics, featuring a single-exponential decay with a lifetime of 205 ps. Our results disclose the aggregated structure and the origin of red- and blue-shifted peaks and explain the absence of photoluminescence in squaraine thin films. Our findings underline the important role of structural disorder of molecular aggregates for photovoltaic applications.

This chapter has been published in the Journal of the American Chemical Society [1]. The following is a reformatted version of the original paper as published. Reprinted with permission from *J. Am. Chem. Soc.* 2022, 144, 42, 19372-19381.

3.1 Introduction

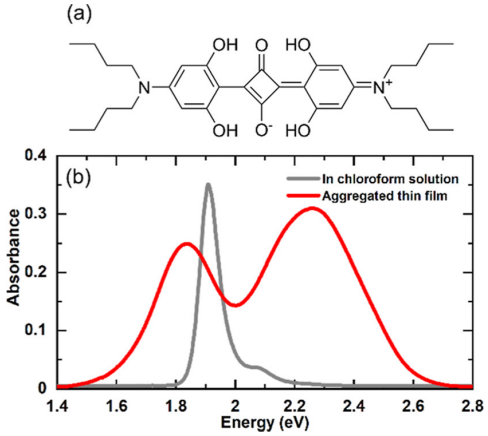

Figure 3.1: Molecular structure and steady-state absorption of nBSQ samples. (a) Chemical skeleton of the monomer nBSQ in the x-y plane of molecular coordinates. (b) Steady-state absorbance spectra of monomeric nBSQ in chloroform solution (gray line) and aggregated thin films on glass substrates (red line).

Aggregated molecular assemblies have attracted considerable interest in many fields of scientific research and technological development [2–7], especially for organic optoelectronic devices [8–11], such as light emitting diodes and solar cells. Their optoelectronic properties depend strongly on the aggregates' structure and morphology, making an understanding of these properties essential to understanding and tuning device performance. In aggregates of molecules with strong optical transitions, the resonance Coulomb interactions between the associated transition dipole moments can yield large spectral shifts, cause changes in absorption linewidths, as well as enhance or quench fluorescent emission. Based on these dipolar interactions of transition dipole moments, two archetypes of aggregates named J- and H-aggregates [12–14] can be formed depending on the relative alignment of the transition dipole moments. In the special case of parallelly aligned transition dipole moments, the slip angle θ between them and the relative position vector connecting two molecules dictates the interaction between them. Importantly, this interaction may either be positive, for $\theta > 54.7°$, or negative, for $\theta < 54.7°$ [13, 15]. This provides a general picture for understanding the spectroscopic properties of molecular aggregates with

parallel transition dipoles. Depending on the slip angle, they may either exhibit a bright state at the high-energy side of the exciton band and a dark state at its low-energy side, as is the case for H-aggregates, or vice versa for J-aggregates.
Although the simple model of J- and H-type aggregates explains the basic spectral properties of many molecular aggregates, there are also many aggregates for which the simple J- and H-picture does not hold and that require a more complicated model [16]. Even for a simple dimer structure, the resonance interaction between chromophores with non-parallel transition dipole moments [17, 18] and charge-transfer interactions [19, 20] may split the exciton band. Also, the aggregate morphology is important: for aggregates with a tubular symmetry, multiple J-bands may occur or even multiple J- and H-bands [21, 22]. Similarly, structural disorder and inhomogeneity of the environment can significantly broaden the spectroscopic response of molecular aggregates. Molecular vibrations further enrich the optical properties. Models including vibrations have been developed based on either dimer- [23–25] or crystal-like aggregation [26, 27] and have been successfully applied to aggregated systems such as TDBC-a cyanine dye-and pseudoisocyanine dyes [28, 29]. In short, there are abundant effects that may complicate aggregate spectra beyond the simple J- and H-band picture. Thus, detailed knowledge of packing, morphology, and additional interactions may be needed for modeling aggregate spectra and optical dynamics.
An unusual aggregation system deviating significantly from the basic J- and H-picture is found for certain squaraine dyes. Due to their unique and easily customizable optical properties [30, 31] this large family of π-conjugated quadrupolar molecules has attracted attention in recent experimental [18, 32–39] and theoretical studies [40–45]. As reported, the molecules can easily form either J- or H-type aggregates depending on their molecular structure [33, 34, 37] and sample preparation conditions [35, 36, 46, 47]. Moreover, squaraines with a symmetric molecular backbone show strong electron-donating and -accepting properties, and both intra- and inter-molecular charge transfer could play an important role in the optical spectra of squaraine aggregates [48]. Recently, a family of n-alkyl aniline squaraines (see Figure 3.1(a)) was synthesized and engineered [49, 50] for organic solar cells which can reach relatively high power conversion efficiencies. The monomeric squaraines contain a strong hydrogen bond network forming a very rigid planar skeleton and can

be referred to as a donor-acceptor-donor system (D-A-D). When forming aggregated solid films, both “J-” and “H-like” transitions were observed simultaneously, while the samples lacked any photoluminescence (see Figures 3.1(b), 3.6 and ref [50]). Note that the terms “J-/H-like” are used for simplicity to assign the features in the absorption spectrum that are red- and blue-shifted relative to the monomer absorption peak.

Surprisingly, despite many efforts and successes made for solar cell application, little is known about the nature of the electronic states in these aggregates and the mechanisms of their formation and structure. To explain the experimentally observed broad optical transitions and lack of photoluminescence, an intermolecular charge transfer model [48] based on a simple dimer analysis has been proposed. However, until now, no direct experimental evidence of charge separation has been observed, and it is not clear how the aggregated structure is related to the intermolecular charge separation in longer and disordered aggregates. Recently, a similar dimer system was modeled [51], suggesting that strong quadrupolar interactions can explain a "red-shifted H-aggregate".

Missing aspects of the quest to understand the optical properties of n-alkyl anilino squaraines are the effects of aggregate size and structural disorder. As previous studies [48, 51] are based on the sophisticated but computationally costly essential states model [52] that includes intermolecular charge transfer, the aggregate size that may be considered in the numerical analysis is very limited. In this study, we will use a much simpler exciton model, in which only dipolar resonance interactions between the molecules are taken into account, a physically plausible form of structural (packing) disorder is considered, and intermolecular charge transfer is ignored. This model is a further simplification with respect to previous studies using the essential states model without charge-transfer interactions [51, 53]. This allows us to model long aggregates and to systematically study the effects of structural disorder, enabling us to show that this simple model explains the measured steady state and broadband transient absorption spectra of thin films of the rigid planar molecule 2,4-bis[4-(N,N-dibutylamino)-2,6-dihydroxyphenyl]-squaraine (nBSQ).

The aggregate excitons decay single exponentially with a lifetime of around 200 ps and show photobleaching and two-exciton absorption in both red- and blue-shifted absorption regions, suggesting a single aggregate system. Not only the steady-state

absorption but also the transient response is in good agreement with the proposed model if two-exciton states are properly included. Our results indicate that nBSQ thin films consist of disordered nanoscale aggregates with excitons delocalized over approximately 10 molecules, stimulating new thoughts about the role of structural disorder for engineering optical properties of molecular aggregates.

3.2 Structural Model and Theory

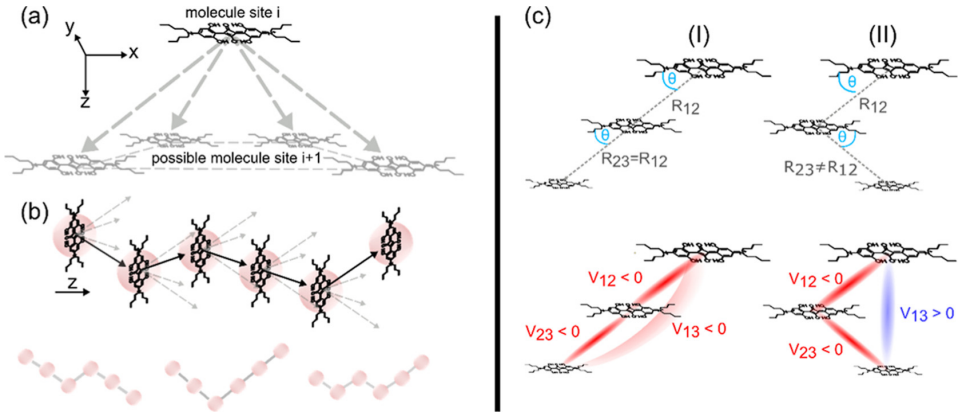

Figure 3.2: Proposed structural model of nBSQ aggregates. (a) For the sequential construction of an aggregate, a new molecule is allowed to occupy one of four spots relative to the previous molecule. (b) Random sequential construction of aggregates yields a disordered aggregate chain. Every construction yields a different structure. (c) Two types of trimers-straight (I) and kinked (II)-demonstrate the influence of structure on the dipolar interaction between the next-nearest neighbors.

The aggregate model proposed here has two main ingredients, namely (i) a specific form of structural disorder and (ii) dipole-dipole resonance (excitation transfer) interactions between the molecules that make up the aggregate. The symmetry of nBSQ molecules (Figure 3.1(a)) acts as a starting point to simulate an aggregate's disordered structure. A single molecule contains two n-butyl-functionalized anilino rings, which behave as electron donors, and a central squaric acid-derived group, which acts as an electron acceptor. The whole D-A-D-like molecule has a D_{2h} symmetry around the squaric center. The molecule's symmetric charge distribution results in the absence of a permanent electric dipole moment. Furthermore, a strong hydrogen

bond network between the phenol hydroxyl groups and the carbonyl oxygen atoms confines the molecule's skeleton into a rigid plane. Thus, both the π-conjugated orbitals and the Coulomb interaction between charge sites steer molecular aggregation. For visualization, the concept is explained using the x,y,z-coordinate system as in Figure 3.2(a,b).

The symmetry of nBSQ and the position of its charges allow us to predict the packing of molecules inside an aggregate. First, neighboring molecules will align their planes parallel to each other. Second, they will be shifted in both the x- and y-direction to optimize their ground-state Coulomb interaction. The resulting translation vector $\vec{R}_{i,i+1}$ between the nearest neighbors can be parameterized as (Δx, Δy, Δz), with Δx, Δy, Δz > 0. Also, due to rotational symmetry, $\vec{R}_{i,i+1}$ is not unique, but for every positive value of Δx(Δy), the negative equivalent -Δx(-Δy) can also be used to construct $\vec{R}_{i,i+1}$. This leads to four possible positions for the next neighbor, with four different $\vec{R}_{i,i+1}$ ($\pm\Delta$x, $\pm\Delta$y, Δz) in a given coordinate system (see Figure 3.2(a)). Note that the slip angle θ between the molecular backbone (which also gives the direction of the transition dipole moment) and $\vec{R}_{i,i+1}$ is the same for all four configurations.

We use this consideration to sequentially construct a disordered aggregate chain. The construction starts with the first molecule being placed in the origin of the coordinate system. The second molecule will be placed with respect to the first in one of the four possible positions described above. This assignment is random. This procedure extends to all other molecules: the next molecule will always be randomly placed with respect to the previously placed adjacent molecule, choosing one of the four possible relative positions. Generally, $\vec{R}_{i,i+1}$ does not have to coincide with $\vec{R}_{i+1,i+2}$, preventing any long-range order and giving rise to structural disorder. Since the Δz-value is constant throughout the construction, the aggregate will always "grow" along the z-direction, forming a disordered aggregate chain. Figure 3.2(b) shows several possible configurations for the case of a hexamer.

Due to the randomized construction, each aggregate has a different structure. Therefore, a macroscopic object like a thin film must be simulated by an ensemble of different aggregates, each constructed independently of the other.

We next turn to the Hamiltonian that describes the optical properties of the proposed structural model. Each molecule is considered to be a two-level system, correspond-

ing to a ground state $|g\rangle$ and a localized excitation $|i\rangle = b_i^\dagger |g\rangle$, where $b_i^\dagger(b_i)$ is the Pauli operator that creates (annihilates) an exciton on molecule i. The basis considered here is spanned by the one-exciton states $|i\rangle$ and two-exciton states $|i\rangle \otimes |j\rangle$ with i $\neq$ j. Two-exciton states are optically dark with respect to transitions from the ground state but become bright for transitions from the one-exciton states, therefore contributing to photoinduced absorption. For the steady-state absorption spectrum, only the one-exciton states are needed, while the transient absorption also probes two-exciton states. In this basis, the Hamiltonian is written as

$$H = \sum_i (E_0 + \Delta E + \delta_i) b_i^\dagger b_i + \sum_{i \neq j} V_{ij} b_i^\dagger b_j \tag{3.1}$$

commonly known as a Frenkel exciton Hamiltonian [54, 55].

The energy difference between the two molecular levels is denoted as E_0, and its value is obtained from monomer spectra in solution. The exact nature of the electronic transition in nBSQ molecules is associated with the symmetric ground and antisymmetric zwitterionic states but is not required for the present simulation. The solution to the crystal energy shift is denoted by ΔE. The excitation energy of each molecule will be slightly different due to the molecule's local environment. This variation is modeled by including a static disorder δ_i, which is sampled from a Gaussian distribution with a standard deviation σ and zero mean. For simplification, vibronic components in the Hamiltonian are neglected as both its spectral transition strength (Figure 3.1(b)) and the associated couplings are small in squaraine dyes [48, 51].
The excitations on different sites are coupled through the resonant coupling V_{ij}. We assume that this interaction is dominated by dipole-dipole interactions and employ the point-dipole approximation

$$V_{ij} = \frac{\mu_i \mu_j}{4\pi\epsilon_0 \epsilon_r R_{ij}^3} \left(1 - 3\cos^2(\theta_{ij})\right) \tag{3.2}$$

where μ_i denotes the transition dipole moment (oriented along the molecular backbone) on site i, $\vec{R}_{i,j} = |\vec{r}_i - \vec{r}_j|$ is the distance between the two molecules, and θ_{ij} is the slip angle between the transition dipole moments and the relative position of both molecules, $\vec{R}_{i,j}$.

This simple interaction scheme shows the influence of structural disorder, unperturbed by other effects, on the aggregate's optical features. Even in a simple system like a trimer, the structural disorder has a profound influence on the interaction, as portrayed in Figure 3.2(c). The two trimers shown in Figure 3.2(c) distinguish two possible alignment cases: *straight* (left) and *kinked* (right). Although both structures feature the same slip angle θ between the nearest neighbors, the next-nearest neighbors' alignment ($\theta_{1,3}$) deviates a lot. While the straight structure always reproduces the same next-nearest angle ($\theta_{1,3} = \theta$), the kinked alignment always changes the angle ($\theta_{1,3} \neq \theta$). This altered angle significantly changes the interaction $V_{1,3}$, potentially even switching it from negative ("J-like") to positive ("H-like"). Moreover, if θ is sufficiently close to the magic angle of 54.7°, the magnitude of the next-nearest neighbor interaction even becomes comparable to the nearest neighbor interaction and influences the optical properties significantly. As "kinks" are more likely, the longer the aggregate gets, the more the non-nearest neighbor interactions become significant. This leads to competing interactions of "J-like" and "H-like" characters, creating a much more complex system than regular J- or H-aggregates.

The absorption spectrum is most easily calculated in the eigenbasis of the Hamiltonian given in eq 3.1 which is obtained by numerical diagonalization [54]. The absorption spectrum is then calculated as follows

$$A(\epsilon) \propto \left\langle \sum_k \mu_k^2 \epsilon_k f(\epsilon - \epsilon_k, \sigma) \right\rangle \tag{3.3}$$

where μ_k and ϵ_k are the transition dipole moment and eigenenergy associated with eigenstate k of the Hamiltonian, respectively. The brackets $\langle\rangle$ denote the ensemble average over many randomly generated disorder realizations, and $f(\epsilon, \sigma)$ is a Gaussian line shape function centered at $\epsilon = 0$ and with a standard deviation of σ. More information on this calculation can be found in Supporting Information, section 3.8.2.

The transient absorption spectra were calculated considering a sequence of a pump pulse and a probe pulse. The pump pulse can bring an aggregate from its ground state into a one-exciton state. The probe pulse may result in a transition from this one-exciton state into a two-exciton state (excited-state absorption) or in stimulated

emission from the one-exciton state back to the ground state. The transient absorption spectrum, being the difference between the probe absorption spectrum and the steady-state absorption spectrum, thus has three contributions: bleaching of the transitions between the ground state and the one-exciton states (negative), stimulated emission of the one-exciton state excited by the pump pulse (negative), and excited-state absorption (positive). A full explanation of the used framework can be found in ref [55] as well as in Supporting Information, section 3.8.2.
To account for dynamical processes, we consider two different exciton occupation populations after photoexcitation by the pump pulse. For short time delays, we estimate the exciton population to reside in the bright state which gets excited by the pump pulse. For longer time delays, we consider a relaxed exciton population which resides in the lowest energy exciton state following a Boltzmann distribution. As the latter exciton occupation does not yield a good fit (see Figure 3.7), we will from now on only address the exciton population at short time delays unless mentioned differently. Similar to the absorption spectrum, the resulting transient spectra are averaged over a large ensemble of disorder realizations.

3.3 Computational Methods

The transition dipole moment μ used to evaluate the interaction strength was calculated from the measured attenuation spectrum of monomeric nBSQ, yielding a high value of 15.6 Debye-a reasonable value given the equally high values for gas-phase time-dependent density functional theory calculations (12.6 Debye, see section 3.8.3 of the Supporting Information) as well as essential state model calculations (19.9 Debye). This yields an interaction strength prefactor $\eta = \frac{\mu^2}{4\pi\epsilon_r\epsilon_0}$ of roughly 150 eVÅ^3. The transition dipole moment of nBSQ is large in contrast to other molecular dyes, for example, porphyrin ($\approx$ 6 Debye) [56, 57] and perylene ($\approx$ 8 Debye) [20], which is consistent with the higher extinction coefficient [50].
The peak of the absorption spectrum of nBSQ in chloroform at 1.91 eV was chosen as the on-site energy E_0. Best fitting spectra were obtained when the static-energy disorder was sampled from a Gaussian distribution with a standard deviation σ of 0.05 eV and a zero mean to account for differences in the monomeric environment inside an aggregate. The stick spectrum was convolved with a narrow Lorentzian

line shape with a full width at half maximum (fwhm) of 0.05 eV.
The size of the simulated aggregate ensemble was determined empirically by increasing it to 10^6 aggregates. The resulting density of states and absorbance converged for all aggregate lengths between 3 and 20 molecules if one ensemble contained at least 5×10^4 independently generated aggregates. Hence, 5×10^4 was chosen as the most effective ensemble size. A comprehensive list of all model parameters used in the simulation can be found in Table 3.1 in Supporting Information, section 3.8.2.

3.4 Experimental Methods

3.4.1 Samples

The nBSQ dye was synthesized and processed to thin films following the previously published procedure [50], where spin-casted and thermally annealed thin film samples were extensively characterized by spectroscopic ellipsometry and X-ray diffraction. For spectroscopy measurements in solution, nBSQ was dissolved in chloroform, and the solutions were sonicated to ensure complete dissolution. The aggregated thin film was obtained by spin coating onto float glass substrates with a film thickness of ca. 15 nm and thermally annealed at 90 °C under an inert atmosphere to obtain the most stable, fully aggregated sample. Further characterization is provided in the Supporting Information, section 3.8.1.

3.4.2 Steady-State Absorption and Fluorescence Measurements

The static absorption spectra were measured using a Lambda 1050 absorption spectrometer (Perkin & Elmer) at ambient conditions ($\approx$ 22 °C). For solution sample measurements, an nBSQ stock solution in chloroform was diluted to a concentration of around 1.5×10^{-6} mol l^{-1} and measured in a cuvette with a 5 mm optical path length. Thin film absorption spectra have been corrected for the substrate response.

An LS-55 fluorescence spectrometer (Perkin & Elmer) was used for fluorescence measurements using 620 nm excitation for the monomeric solution and 650 nm for the thin films.

3.4.3 Ultrafast Transient Absorption Spectroscopy

Femtosecond white light spectroscopy was conducted using a spectrometer based on a 125 kHz, Yb:KGW regenerative amplifier laser system (PHAROS, Light Conversion) [58]. Band-pass filtered pulses from a non-collinear optical parametric amplifier (NOPA, Light Conversion) were used for pumping the sample with a temporal width of 100-150 fs at 1.72 eV (720 nm). To prevent laser degradation of the aggregated films, the excitation pulse energy was attenuated to around 2 nJ per pulse and slightly focused onto the sample with a spot size of around 200 µm in diameter. For the probe, a 1450 nm laser beam is tightly focused into a 2 mm thick sapphire plate to generate a white light supercontinuum. The white light beam was spectrally filtered, limiting the range to 500-800 nm. The transient spectra were detected using a silicon-based diode array mounted in a polychromatic spectrometer (HARPIA, Light Conversion). To minimize pump scattering into the detector, the polarization of the pump beam was set perpendicular to that of the probe, and a polarizer was placed in front of the detector.

3.5 Results and Discussion

3.5.1 Steady-State Absorption

The absorbance of monomeric nBSQ in chloroform solution (gray line in Figure 3.1(b)) shows a maximum absorption peak at around 650 nm (1.91 eV), corresponding to the optical HOMO to LUMO transition (S0 $\rightarrow$ S1) [59, 60]. The maximum absorption peak has a molar extinction coefficient of around 4×10^5 M^{-1} cm^{-1} [50]. A relatively weak shoulder peak at around 590 nm (2.1 eV) is assigned to the vibronic progression (0-1). The main absorption peak carries a fwhm of around 0.1 eV. In contrast to the monomer, the aggregated thin film exhibits two broad absorption peaks (red line in Figure 3.1(b)), one centered at around 1.84 eV (fwhm $\approx$ 0.25 eV) and another centered at around 2.26 eV (fwhm $\approx$ 0.4 eV). In contrast to the monomer's absorption spectrum, the higher-energy peak is blue-shifted by around 0.36 eV, while the lower-energy peak is red-shifted by around 0.06 eV. Such a large energy separation between the two peaks must be beyond vibronic coupling. Another intricate aspect is the total quenching of photoluminescence in the aggregated thin film (see Sup-

porting Information, section 3.8.4, Figure 3.5), indicating that the red-shifted peak cannot be ascribed to a regular J-band coinciding with the bottom of the exciton band. Other explanations such as H-aggregation mixing with red-shifted monomers or Davydov-splitting can be safely ruled out as well due to the absence of observable photoluminescence. Our observations are in line with previous reports [48, 50].
Figure 3.4(a) shows how the simulated spectrum using the proposed model with structural disorder and dipolar resonant interactions is in agreement with the measured spectrum. The simulation reproduces both the position and the width of both spectral features, where the width is found to be dominated by the structural disorder.
The optimized structural parameters are N = 10 molecules, with Δx = 3 Å, Δy = 1 Å, and Δz = 3.9 Å. The latter values deviate from the single-crystal XRD [50]-derived lattice parameters (Δx = 3.52 Å, Δy = 1.93 Å, and Δz = 3.34 Å), suggesting a different structure in thin films and single crystals. The resulting slip angle θ between the molecular axis and the translation vector is 53.3°, which yields a nearest-neighbor interaction energy of -0.08414 eV. Note that the Madelung energy includes both the nearest and non-nearest neighbor interactions and thus will be much bigger. Additionally, the much smaller value for Δy compared to the single crystal results in a slightly bigger slip angle, favoring H-like interactions and increasing the impact of structural disorder.
An important finding of our simulations is that the density of states (gray area) extends below the absorption edge, resulting in low-energy dark states. This is consistent with the observed lack of photoluminescence, as the low-energy dark states are of exciton-band character, providing a fast relaxation channel and therefore following Kasha's rule. While disorder, in general, is predicted to increase the photoluminescence efficiency of H-aggregates [61], this effect seems not pronounced enough to be visible in our simulation due to the ensemble character of the model, in which most aggregates do have a purely dark lowest energy state. While our model provides an intuitive understanding of the lack of photoluminescence in the thin film sample, other effects might increase the quenching further. The ensemble character of the model provides an efficient platform for reabsorption of emitted photons, which further increases concentration quenching. Forming of other quasiparticles like polarons or excimers as well as adiabatic processes like spin-flips might further enhance this

effect, but are outside the scope of this study.

3.5.2 Transient Absorption

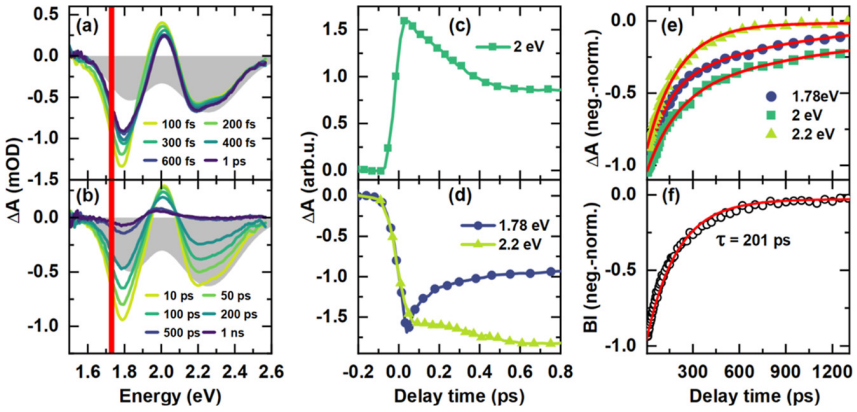

Figure 3.3: Dispersion-corrected transient absorption spectra at selected delay times and dynamics. The red bar indicates the pump energy. (a) Transient spectra in a short delay time range. (b) Transient spectra in a long delay time range. The gray area indicates the negative absorption profile as a rescaled reference. (c-f) Relaxation dynamics observed at different energies. (c) Short time range at 2.0 eV. (d) Short time range at 1.8 and 2.2 eV. (e) Long time range at 1.78, 2.0 eV (flipped for comparison), and 2.2 eV, renormalized. (f) Band integral dynamics as obtained from eq 3.3. Dots are experimental data, and red lines are fitted with exponential functions.

To further investigate the origin of the excitonic transitions and their dynamics, we performed transient absorption spectroscopy. In these experiments, the aggregated nBSQ thin film was excited on the low-energy side of the lowest absorption band (1.722 eV/720 nm) and probed by broadband white light (1.5-2.6 eV/500-800 nm). The measured white light dispersion-corrected transient absorption spectra are presented in Figure 3.3(a,b) for selected delay times. At earlier delay times, there are four main observations: (1) bleaching of both the lower- and higher-energy peaks appears simultaneously upon excitation, indicating that they stem from the same species and share a common ground state; (2) the amplitude ratio between both peaks differs from the steady-state absorption data; (3) a positive peak appears in the middle of the spectral range at around 2 eV, with a narrower linewidth than the bleach signals; (4) dynamics of the two bleaching signals are different. Similar results were obtained when we exited the aggregated film with a higher energy of 2.43 eV

(510 nm) (see Supporting Information section 3.8.5, Figure 3.6).
Figure 3.3(c-e) shows three representative decay curves taken at 1.8, 2.0, and 2.2 eV, respectively, for both short and long delay times. The sub-ps dynamics for the high-energy region is considerably different from the other regions, as the signal is even slowly increasing for the first 800 fs. The non-exponential shape and duration of the growth suggest a more complex mechanism, possibly due to the relaxation of the exciton population into lower-energy states.
Fitted exponential functions (see Figure 3.3(e)) indicate that long-time dynamics at 2.2 eV roughly follows a mono-exponential decay with a lifetime of 205 ps, while the other two require at least bi-exponential decay functions. The sub-picosecond rise of the dynamics as well as the nature of the second relaxation channel seen only at long delay times and for a selected energy range cannot intuitively be explained in the context of the exciton-band model of non-interacting aggregate chains and suggests more complex interactions like energy transfer between aggregates, Coulomb screening effects, or charge-transfer interactions.
To gain further insights into the exciton recombination processes, the band integral (BI) [62, 63] over the whole observed spectral region at different delay times was calculated from the raw data by using the formula

$$BI(t) = \int_{1.55\ \mathrm{eV}}^{2.38\ \mathrm{eV}} \frac{\Delta OD(\epsilon, t)}{\epsilon} d\epsilon \tag{3.4}$$

Figure 3.3(f) shows the resulting dynamics. The BI dynamics can be fitted by a single-exponential decay with a time constant of 201 ps, similar to the high-energy dynamics. Therefore, the lifetime of excitons in the aggregated nBSQ film is close to 200 ps, which is much longer than in other molecular aggregates [33, 64] (usually 10-100 ps) formed by squaraines with relatively flexible molecular structures (with a less pronounced or even no hydrogen bond network); the more rigid molecular backbone of nBSQ may prevent deformation-assisted relaxation pathways.
As the transient response is more complex than just long-lived bleaching of the steady-state absorption at the lower- and higher-energy sides, our simulations must also consider the two-exciton absorption and stimulated emission contributions, as described in the Structural Model and Theory section.
Figure 3.4(b) shows the measured and simulated transient absorption spectrum at

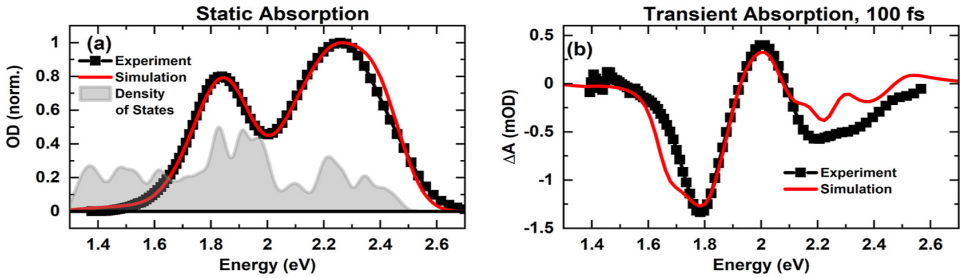

Figure 3.4: Comparison of the measured and simulated steady-state (a) and transient (b) absorption spectrums of thin film nBSQ. Panel (a) shows the density of states in addition to the absorbance spectrum. Both broad absorption humps are replicated by the simulation, while the density of states below the absorption edge shows the presence of dark states. Panel (b) shows the transient absorption signal at 100 fs after photoexcitation. The decomposition of the transient absorption in terms of ground-state bleach, two-exciton absorption, and stimulated emission is found in the Supporting Information, section 3.8.6, Figure 3.7.

100 fs after photoexcitation. A decomposition of the simulated spectrum can be found in Supporting Information, section 3.8.7. The simulated spectrum qualitatively reproduces the main features of the experimental spectrum: (1) simultaneous bleaching of both lower- and higher-energy regions, (2) a higher negative contribution of the low-energy side compared to the higher-energy side, and (3) a positive signal in between.

Deviations between the simulation and experiment can be seen: (i) on the low-energy shoulder of the low-energy hump. Apparently, the measured stimulated emission is much more suppressed than the simulated one. This could be due to reabsorption inside the thin film. (ii) The high-energy signal seems to be too low in the simulation. (iii) The measured data shows a substructure in the transient signal at higher energies, which is also present to an even higher extent in the simulated spectrum. The substructure may be smoothened by including vibrational modes or explicit modeling of a bath, but this is beyond the scope of this paper.

We have not been able to fit longer time transients by a changed occupation distribution as described above. This indicates a more important role of additional, weaker interactions. Examples might be charge-transfer interactions as well as Förster energy transfer between aggregates, which could explain the multitude of relaxation channels seen in the experimental data.

The two-level approximation employed here is mostly valid for disordered one- di-

mensional chains. It is known, however, that monomer squaraine dyes have a dark second-excited state, which is optically forbidden from the ground state while having a large transition dipole moment from the first excited state [52]. This dark state has much lower energy than the probe pulse ($\approx$ 1.17 eV). Furthermore, the relative contribution to the transient absorption spectrum resulting from transitions from the superradiant exciton state to the third level of various molecules scales inversely proportional to the aggregate size N [65]. Hence, the effect of these dark states on the results presented here is expected to be small.

Although many different configurations of the slip angle θ and the number of monomers in an aggregate N were simulated here, only the best-fit parameters for θ and N yield a satisfying fit to the steady-state absorption spectra. While θ influences the spectrum by changing the relative strength of the nearest- and non-nearest neighbor interactions, N affects the spectrum in many ways. The aggregate size influences the width of the signals as well as the relative contribution of high-energy bright states (see Supporting Information, section 3.8.7 and Figure 3.8(a)). A possible reason lies in the "edge effect" of a decreasing amount of non-nearest neighbor interactions when approaching the edge of an aggregate chain. Since "H-like" interactions can only occur between the non-nearest neighbors, near the edge, "H-like" interactions become scarce, resulting in more low-energy states. Further understanding of this effect requires a statistical analysis, which is outside the scope of this work.

During our simulation study, we found that the static-energy disorder parametrized by σ and the width of the Lorentzian lineshape Γ only slightly improved the fit. The main broadening of the two humps in the absorption spectrum must therefore be due to the structural disorder in the aggregates (see also Figure 3.8(b)). Based on the sensitivity of the simulation to θ and N, which is comparable to aggregate lengths of other molecules [14, 66, 67], the best fit results are very robust.

Overall, both the steady-state and initial transient absorption of nBSQ thin films can be explained using the proposed model with only dipolar excitation transfer interactions and structural stacking disorder with reasonable translation distances, not too far away from the lattice parameters found for single crystals. Our data show that structural disorder alone can account for all features of the steady-state absorption spectrum, the lack of photoluminescence of the red-shifted aggregate peak, as well as the large linewidths of both absorption bands. To achieve this, the lattice

parameters have been refitted to enhance H-like couplings in the excitonic model. A continuous transient response to photoexcitation over the whole region of absorption underlines that, while there is a multitude of aggregates, both humps originate from the same set of aggregates.

The intrinsic simplicity of the model provides a solid tool for fast simulations of the absorption spectrum and facilitates reverse engineering of structure-property relations. As the computational cost is small compared to more sophisticated techniques, finding fitting parameters for the disordered structure model can be done even on personal computers without the need of clusters or other sources of high computational output. Moreover, we do not need to impose the single-crystal structure onto the thin film, allowing us to find structures which might describe non-crystalline structures better.

The limitations of the proposed model arise from the greatly simplified molecular interaction. The excitonic model considered here can be extended with vibronic coupling, which leads to asymmetric line shapes of the two peaks. Also, intra- and inter-molecular charge-transfer interactions are not included in this study as they were not needed to model the experimental spectra. This is in contrast to the essential states model used in a previous study [48] where charge transfer was included to explain the two-peak absorption spectrum. In this previous study [48] however, a dimer was considered which is not able to generate the competing J- and H-like couplings found in this paper. Including structural disorder in the essential states model may significantly lower the intermolecular charge-transfer coupling required to obtain a two-peak absorption spectrum.

Adding a modest amount of charge transfer could improve the accuracy of our model at long delay times. Considering the long intrinsic lifetime of charges as well as charge-induced spectral distortions could result in a more satisfying agreement between the simulation and experiment.

The degeneracy of the four different alignments considered in our model might also need further tuning considering the alkyl arms of nBSQ. If a C_{2v} symmetry is chosen instead of a D_{2h} symmetry, the alkyl arm would influence the probability of the four possible alignments and potentially even the alignment vector itself. This consideration could broaden the applicability of the structural disorder model to molecules of lower symmetry. In any case, these more advanced aspects of spectral modeling

are not necessary to describe the molecular system at hand.

The importance of discussing nBSQ aggregates as disordered is underlined by previous studies [50], which have shown that nBSQ thin films are isotropic in-plane. Additionally, the intermolecular distances used in this model are similar to single-crystal data [50], strengthening our claim of a reliable model. A yet pending question is the strong out-of-plane order observed by XRD, as our experimental setup does not allow probing in this direction.

3.6 Conclusions

In conclusion, we have systematically investigated the optical properties of an aggregated thin film of the squaraine derivative nBSQ with a rigid planar molecular structure by using both steady-state and time-resolved spectroscopy methods. The aggregated film showed a complex steady-state absorption spectrum as well as intricate excited-state dynamics. We observed a transient response across the whole absorption spectrum. Through band integration of the transient spectra, we were able to show that the exciton decays with a lifetime of around 200 ps. Using a model with only dipolar excitation transfer interaction and plausible structural (stacking) disorder, we successfully interpreted all observed phenomena in both steady-state and short-time transient absorption spectra, including their exceptionally large linewidth. Our data suggests that disorder alone can qualitatively reproduce all measured optical features. The results and the model analysis presented here can have significant guidance on further control and manipulation of squaraine aggregates for optoelectronic applications.

3.7 Contributions

Robin Bernhardt, Jingyi Zhu and Manuela Schiek conceived the project. Robin Bernhardt, Lukas Rieland and Jingyi Zhu performed the steady-state and transient optical experiments and analyzed the experimental results. Robin Bernhardt and Jingyi Zhu realized the simulations of the steady-state optical properties. Jennifer Zablocki and Arne Lützen synthesized the squaraine molecules. Manuela Schiek and

Klaus Meerholz prepared and characterized the thin film samples. Marick Manrho, Thomas la Cour Jansen and Jasper Knoester provided the simulation of the transient spectra. Paul van Loosdrecht supervised the project.

References

(1) Bernhardt, R.; Manrho, M.; Zablocki, J.; Rieland, L.; Lützen, A.; Schiek, M.; Meerholz, K.; Zhu, J.; Jansen, T. L. C.; Knoester, J.; van Loosdrecht, P. H. M. *Journal of the American Chemical Society* **2022**, *144*, 19372–19381.

(2) Huang, Y.; Xing, J.; Gong, Q.; Chen, L.-C.; Liu, G.; Yao, C.; Wang, Z.; Zhang, H.-L.; Chen, Z.; Zhang, Q. *Nature Communications* **2019**, *10*, 169.

(3) Manzhos, S.; Chueh, C.-C.; Giorgi, G.; Kubo, T.; Saianand, G.; Lüder, J.; Sonar, P.; Ihara, M. *The Journal of Physical Chemistry Letters* **2021**, *12*, 4638–4657.

(4) Tan, J.-H.; Chen, W.-C.; Ni, S.-F.; Qiu, Z.; Zhan, Y.; Yang, Z.; Xiong, J.; Cao, C.; Huo, Y.; Lee, C.-S. *Journal of Materials Chemistry C* **2020**, *8*, 8061–8068.

(5) Kuehne, A. J. C.; Gather, M. C. *Chemical Reviews* **2016**, *116*, 12823–12864.

(6) Saikin, S. K.; Eisfeld, A.; Valleau, S.; Aspuru-Guzik, A. *Nanophotonics* **2013**, *2*, 21–38.

(7) Mei, J.; Leung, N. L. C.; Kwok, R. T. K.; Lam, J. W. Y.; Tang, B. Z. *Chemical Reviews* **2015**, *115*, 11718–11940.

(8) Ostroverkhova, O. *Chemical Reviews* **2016**, *116*, 13279–13412.

(9) Clarke, T. M.; Durrant, J. R. *Chemical Reviews* **2010**, *110*, 6736–6767.

(10) Zhang, L.; Cole, J. M. *Journal of Materials Chemistry A* **2017**, *5*, 19541–19559.

(11) Xu, F.; Testoff, T. T.; Wang, L.; Zhou, X. *Molecules* **2020**, *25*, 4478.

(12) Kasha, M. *Radiation Research* **1963**, *20*, 55–70.

(13) Kasha, M.; Rawls, H. R.; Ashraf El-Bayoumi, M. *Pure and Applied Chemistry* **1965**, *11*, 371–392.

(14) Würthner, F.; Kaiser, T. E.; Saha-Möller, C. R. *Angewandte Chemie International Edition* **2011**, *50*, 3376–3410.

(15) Gierschner, J.; Park, S. Y. *Journal of Materials Chemistry C* **2013**, *1*, 5818–5832.

(16) Spano, F. C.; Silva, C. *Annual Review of Physical Chemistry* **2014**, *65*, 477–500.

(17) Kistler, K. A.; Pochas, C. M.; Yamagata, H.; Matsika, S.; Spano, F. C. *The Journal of Physical Chemistry B* **2012**, *116*, 77–86.

(18) Zhong, C.; Bialas, D.; Collison, C. J.; Spano, F. C. *The Journal of Physical Chemistry C* **2019**, *123*, 18734–18745.

(19) Hennessy, M. H.; Pascal, R. A.; Soos, Z. G. *Molecular Crystals and Liquid Crystals Science and Technology. Section A.* **2001**, *355*, 41–63.

(20) Gisslén, L.; Scholz, R. *Physical Review B* **2009**, *80*, 115309.

(21) Eisele, D. M.; Cone, C. W.; Bloemsma, E. A.; Vlaming, S. M.; van der Kwaak, C. G. F.; Silbey, R. J.; Bawendi, M. G.; Knoester, J.; Rabe, J. P.; Vanden Bout, D. A. *Nature Chemistry* **2012**, *4*, 655–662.

(22) Didraga, C.; Pugžlys, A.; Hania, P. R.; von Berlepsch, H.; Duppen, K.; Knoester, J. *The Journal of Physical Chemistry B* **2004**, *108*, 14976–14985.

(23) Fulton, R. L.; Gouterman, M. *The Journal of Chemical Physics* **1964**, *41*, 2280–2286.

(24) Fulton, R. L.; Gouterman, M. *The Journal of Chemical Physics* **1961**, *35*, 1059–1071.

(25) Yang, M. *Journal of Molecular Spectroscopy* **2006**, *239*, 108–114.

(26) Briggs, J. S.; Herzenberg, A. *Journal of Physics B: Atomic and Molecular Physics* **1970**, *3*, 1663–1676.

(27) Briggs, J.; Herzenberg, A. *Molecular Physics* **1971**, *21*, 865–879.

(28) Eisfeld, A.; Briggs, J. S. *Chemical Physics* **2002**, *281*, 61–70.

(29) Eisfeld, A.; Briggs, J. S. *Chemical Physics* **2006**, *324*, 376–384.

(30) Ajayaghosh, A. *Accounts of Chemical Research* **2005**, *38*, 449–459.

(31) Liu, T.; Liu, X.; Wang, W.; Luo, Z.; Liu, M.; Zou, S.; Sissa, C.; Painelli, A.; Zhang, Y.; Vengris, M.; Bondar, M. V.; Hagan, D. J.; Van Stryland, E. W.; Fang, Y.; Belfield, K. D. *The Journal of Physical Chemistry C* **2018**, *122*, 3994–4008.

(32) Law, K. Y.; Chen, C. C. *The Journal of Physical Chemistry* **1989**, *93*, 2533–2538.

(33) Chen, H.; Farahat, M. S.; Law, K.-Y.; Whitten, D. G. *Journal of the American Chemical Society* **1996**, *118*, 2584–2594.

(34) Dimitriev, O. P.; Dimitriyeva, A. P.; Tolmachev, A. I.; Kurdyukov, V. V. *The Journal of Physical Chemistry B* **2005**, *109*, 4561–4567.

(35) Deing, K. C.; Mayerhöffer, U.; Würthner, F.; Meerholz, K. *Physical Chemistry Chemical Physics* **2012**, *14*, 8328–8334.

(36) Chen, G.; Sasabe, H.; Lu, W.; Wang, X.-F.; Kido, J.; Hong, Z.; Yang, Y. *Journal of Materials Chemistry C* **2013**, *1*, 6547–6552.

(37) Zhang, Y.; Kim, B.; Yao, S.; Bondar, M. V.; Belfield, K. D. *Langmuir* **2013**, *29*, 11005–11012.

(38) Mayerhöffer, U.; Würthner, F. *Chemical Science* **2012**, *3*, 1215–1220.

(39) McKerrow, A. J.; Buncel, E.; Kazmaier, P. M. *Canadian Journal of Chemistry* **1995**, *73*, 1605–1615.

(40) Xu, J.; Zhang, H.; Wang, L.; Liang, G.; Wang, L.; Shen, X.; Xu, W. *Monatshefte für Chemie - Chemical Monthly* **2010**, *141*, 549–555.

(41) Wang, X.; Xu, J.; Li, M.; Fang, D.; Chen, B.; Wang, L.; Xu, W. *RSC Advances* **2013**, *3*, 5227–5237.

(42) AL-Fahdan, N. S.; Asiri, A. M.; Irfan, A.; Basaif, S. A.; El-Shishtawy, R. M. *Journal of Molecular Modeling* **2014**, *20*, 2517.

(43) Kaczmarek-Kedziera, A.; Kędziera, D. *Theoretical Chemistry Accounts* **2016**, *135*, 214.

(44) Divya, V. V.; Suresh, C. H. *ChemistrySelect* **2019**, *4*, 3387–3394.

(45) Kaczmarek-Kędziera, A.; Żuchowski, P. S.; Kędziera, D. *Scientific Reports* **2020**, *10*, 19670.

(46) Balzer, F.; Kollmann, H.; Schulz, M.; Schnakenburg, G.; Lützen, A.; Schmidtmann, M.; Lienau, C.; Silies, M.; Schiek, M. *Crystal Growth & Design* **2017**, *17*, 6455–6466.

(47) Zablocki, J.; Arteaga, O.; Balzer, F.; Hertel, D.; Holstein, J. J.; Clever, G.; Anhäuser, J.; Puttreddy, R.; Rissanen, K.; Meerholz, K.; Lützen, A.; Schiek, M. *Chirality* **2020**, *32*, 619–631.

(48) Hestand, N. J.; Zheng, C.; Penmetcha, A. R.; Cona, B.; Cody, J. A.; Spano, F. C.; Collison, C. J. *The Journal of Physical Chemistry C* **2015**, *119*, 18964–18974.

(49) Zheng, C.; Penmetcha, A. R.; Cona, B.; Spencer, S. D.; Zhu, B.; Heaphy, P.; Cody, J. A.; Collison, C. J. *Langmuir* **2015**, *31*, 7717–7726.

(50) Zablocki, J.; Schulz, M.; Schnakenburg, G.; Beverina, L.; Warzanowski, P.; Revelli, A.; Grüninger, M.; Balzer, F.; Meerholz, K.; Lützen, A.; Schiek, M. *The Journal of Physical Chemistry C* **2020**, *124*, 22721–22732.

(51) Zheng, C.; Zhong, C.; Collison, C. J.; Spano, F. C. *The Journal of Physical Chemistry C* **2019**, *123*, 3203–3215.

(52) Terenziani, F.; Painelli, A.; Katan, C.; Charlot, M.; Blanchard-Desce, M. *Journal of the American Chemical Society* **2006**, *128*, 15742–15755.

(53) D'Avino, G.; Terenziani, F.; Painelli, A. *The Journal of Physical Chemistry B* **2006**, *110*, 25590–25592.

(54) Fidder, H.; Knoester, J.; Wiersma, D. A. *The Journal of Chemical Physics* **1991**, *95*, 7880–7890.

(55) Bakalis, L. D.; Knoester, J. *The Journal of Physical Chemistry B* **1999**, *103*, 6620–6628.

(56) Ageeva, T. A.; Bush, A. A.; Golubev, D. V.; Gorshkova, A. S.; Kamentsev, K. E.; Koifman, O. I.; Rumyantseva, V. D.; Sigov, A. S.; Fomichev, V. V. *Journal of Organometallic Chemistry* **2020**, *922*, 121355.

(57) Oviedo, M. B.; Sánchez, C. G. *The Journal of Physical Chemistry A* **2011**, *115*, 12280–12285.

(58) Jung, E.; Budzinauskas, K.; Öz, S.; Ünlü, F.; Kuhn, H.; Wagner, J.; Grabowski, D.; Klingebiel, B.; Cherasse, M.; Dong, J.; Aversa, P.; Vivo, P.; Kirchartz, T.; Miyasaka, T.; van Loosdrecht, P. H. M.; Perfetti, L.; Mathur, S. *ACS Energy Letters* **2020**, *5*, 785–792.

(59) Momicchioli, F.; Tatikolov, A. S.; Vanossi, D.; Ponterini, G. *Photochemical & Photobiological Sciences* **2004**, *3*, 396–402.

(60) Mayerhöffer, U.; Gsänger, M.; Stolte, M.; Fimmel, B.; Würthner, F. *Chemistry – A European Journal* **2013**, *19*, 218–232.

(61) Spano, F. C. *The Journal of Chemical Physics* **2005**, *122*, 234701.

(62) Quick, M.; Kasper, M.-A.; Richter, C.; Mahrwald, R.; Dobryakov, A. L.; Kovalenko, S. A.; Ernsting, N. P. *ChemPhysChem* **2015**, *16*, 3824–3835.

(63) Sharma, V.; Aharon, S.; Gdor, I.; Yang, C.; Etgar, L.; Ruhman, S. *Journal of Materials Chemistry A* **2016**, *4*, 3546–3553.

(64) De Miguel, G.; Ziółek, M.; Zitnan, M.; Organero, J. A.; Pandey, S. S.; Hayase, S.; Douhal, A. *The Journal of Physical Chemistry C* **2012**, *116*, 9379–9389.

(65) Knoester, J. *Physical Review A* **1993**, *47*, 2083–2098.

(66) Bakalis, L. D.; Knoester, J. *Journal of Luminescence* **2000**, *87-89*, 66–70.

(67) Arias, D. H.; Stone, K. W.; Vlaming, S. M.; Walker, B. J.; Bawendi, M. G.; Silbey, R. J.; Bulović, V.; Nelson, K. A. *The Journal of Physical Chemistry B* **2013**, *117*, 4553–4559.

3.8 Supplementary Information

3.8.1 Basic Information and Characterizations of Molecule nBSQ

The XRD properties of an identical film have been reported in Ref.[1], confirmation of the sample used in the experiment was conducted by comparing ellipsometry data.

IUPAC nomination: 2,4-Bis[4-(N,N-dibutylamino)-2,6-dihydroxyphenyl]-squaraine.

^{1}H NMR: (500 MHz, chloroform-d) Δ[ppm] = 10.98 (s, 4H), 5.78 (s, 4H), 3.37-3.30 (m, 8H), 1.67-1.58 (m, 8H), 1.36 (h, ^{3}J = 7.4 Hz, 8H), 0.97 (t, ^{3}J = 7.4 Hz, 12H).

^{13}C NMR: (126 MHz, chloroform-d) Δ[ppm] = 181.5, 162.9, 161.2, 158.0, 102.5, 93.8, 51.6, 30.2, 20.4, 14.3

MS (ESI+ high-resolution mass spectrometry (HRMS)): m/z calculated for $C_{32}H_{44}N_2O_6$ $M\bullet^+$: 552.3194, found: 552.3195.

Elemental analysis: calculated for $C_{32}H_{44}N_2O_6$: C: 69.54; H: 8.02; N: 5.07, found: C: 69.41; H: 8.18; N: 4.98.

UV-vis: (chloroform) λ_{max} = 650 nm, ε= 386 000 M^{-1} cm^{-1}.

3.8.2 Calculation of Absorption and Transient Absorption Spectra

The absorption spectrum of Fig. 3.4(a) is obtained as follows. We define the transition dipole operator between the ground and excited state as $\hat{\mu} = \sum \mu_i (b_i + b_i^\dagger)$, only including transitions between the ground state and one-exciton states and between the one- and two-exciton states. The transition dipole operator is then rotated to the numerically obtained eigenbasis of the Hamiltonian given in Eq. 3.1. The eigenbasis of the Hamiltonian satisfies $H\left|k\right\rangle = \epsilon_k \left|k\right\rangle$, where $\left|k\right\rangle$ is the k-th eigenstate and ϵ_k the corresponding eigenenergy. It should be noted here that k lables the eigenstates of both the one- and the two-exciton bands.
The absorption spectrum is then given by the following expression [2, 3]

$$I(\omega) = \left\langle \sum_k \epsilon_k |\hat{\mu_{gk}}|^2 \frac{1}{\sigma_{abs}\sqrt{2\pi}} e^{-\frac{(\omega-\epsilon_k)^2}{2\sigma_{abs}^2}} \right\rangle \tag{3.5}$$

where $\hat{\mu_{gk}} = \langle g|\,\hat{\mu}\,|k\rangle$ is the transition dipole moment between the ground state and the k-th eigenstate of the Hamiltonian, ϵ_k is the energy of the k-th eigenstate, and σ_{abs} is the standard deviation of the Gaussian line shape, assumed equal for all exciton transitions. The brackets denote averaging over the structural disorder and polarization of the incoming light. The average over polarization assumes an isotropic distribution of aggregates on the surface.
The transient absorption spectrum is calculated for both a short- and long-waiting time between the pump and probe pulses T_2. To obtain the expression for the transient absorption spectrum at short waiting times we use third-order response theory which leads to [2, 4]

$$\begin{aligned}
&\Delta A(\omega_1, \omega_2) \\
&= -\int d\omega_1' \int d\omega_2' \hat{I}_{pu}(\omega_1 - \omega_1') \hat{I}_{pr}(\omega_2 - \omega_2') \times \left\langle \sum_k \frac{|\hat{\mu}_{gk}|^2 \Gamma}{(\omega_1' - \epsilon_k)^2 + \Gamma^2} \right. \\
&\left. \left\{ \sum_{k'} \frac{|\hat{\mu}_{gk'}|^2 \Gamma}{(\omega_2' - \epsilon_{k'})^2 + \Gamma^2} + \sum_{k'} \delta_{k,k'} \frac{|\hat{\mu}_{gk'}|^2 \Gamma}{(\omega_2' - \epsilon_{k'})^2 + \Gamma^2} - \sum_{k''} \frac{|\hat{\mu}_{k,k''}|^2 \Gamma}{(\omega_2' + \epsilon_k - \epsilon_{k''})^2 + \Gamma^2} \right\} \right\rangle
\end{aligned} \tag{3.6}$$

where ω_1 and ω_2 denote the pump and probe frequencies respectively and $\hat{I}_{pu}(\omega)$ and $\hat{I}_{pr}(\omega)$ are the line-shape functions of the pump and probe respectively. The

pump spectrum $\hat{I}_{pu}$ has been approximated by a Gaussian line shape with a mean energy 1.722 eV and a standard deviation of 0.05 eV in accordance to the experiment - all states in this energy region can be excited. The probe spectrum $\hat{I}_{pr}$ was approximated as a uniform distribution, e.g., a constant intensity for all frequencies. In Eq. 3.6 the indices k and k' label one-exciton states and k'' labels two-exciton states. The matrix elements of $\hat{\mu}$ for transitions between one- and two-exciton states in the site basis are found using the relation $\langle n, m| \hat{\mu} |n, q\rangle = \langle m| \hat{\mu} |q\rangle$. The matrix elements in the eigenbasis are then obtained using $\mu_{k,k''} = \langle k| \hat{\mu} |k''\rangle$.
The three terms inside the curly brackets in Eq. 3.6 correspond to the contributions from ground-state bleach, stimulated emission, and two-exciton absorption respectively. Eq. 3.6 is used to obtain the model transient absorption spectrum for nBSQ as is shown in Fig. 3.3(b).
For long waiting times T_2, we assume that between the two pulses, the population relaxes to a Boltzmann distribution of the exciton states. Hence the equation for the transient absorption spectrum becomes

$$\Delta A(\omega_1, \omega_2) = -\int d\omega_1' \int d\omega_2' \hat{I}_{pu}(\omega_1 - \omega_1') \hat{I}_{pr}(\omega_2 - \omega_2') \times \left\langle \sum_{k>g} \frac{1}{Z} e^{-\frac{(\epsilon_k - \epsilon_g)}{k_b T}} \left\{ \sum_{k'} \frac{|\hat{\mu}_{gk'}|^2 \Gamma}{(\omega_2' - \epsilon_{k'})^2 + \Gamma^2} + \sum_{k'} \delta_{k,k'} \frac{|\hat{\mu}_{gk'}|^2 \Gamma}{(\omega_2' - \epsilon_{k'})^2 + \Gamma^2} - \sum_{k''} \frac{|\hat{\mu}_{k,k''}|^2 \Gamma}{(\omega_2' + \epsilon_k - \epsilon_{k''})^2 + \Gamma^2} \right\} \right\rangle \tag{3.7}$$

where Z is the partition function and T is the temperature. The resulting long-time spectrum for nBSQ is shown in Fig. 3.7. From Fig. 3.7 it becomes clear that the long-time TA spectrum is not explained well by a Boltzmann distribution and a more sophisticated approach is needed.

Table 3.1: Summary of model parameters used throughout this paper.

Model Parameter	Value
E_0	1.91 eV
ΔE	-0.05 eV
$\|\mu\|$	15.6 D
ϵ_r	1
Δx	3 Å
Δy	1 Å
Δz	3.9 Å
σ_{abs}	0.085 eV
Γ	0.05 eV
σ_{static}	0.05 eV
$N_{samples}$	10^6
$N_{molecules}$	10
T	293 K
$\langle \hat{I}_{pu} \rangle$	1.722 eV
σ_{pu}	0.05 eV
$\hat{I}_{pr}$	Uniform

3.8.3 (Time-Dependent) Density Functional Theory Calculations

The geometry of the core of the squaraine chromophore with the aliphatic tails removed was minimized using gas phase Density Functional Theory (DFT) calculations with the ωB97X-D3 exchange correlation functional [3] and the def2-TZVPP basis [5] in the ORCA 4.1.0 program package [6]. The lowest excitation energy was then determined using Time-Dependent DFT without invoking the Tamm-Dancoff approximation [7]. The S0 to S1 excitation energy was found to be 2.52 eV and the transition-dipole 12.6 Debye.

3.8.4 Steady State Photoluminescence Measurements

PL of the monomer in the aggregated thin film of nBSQ and solution were measured with excitation wavelength of 650 nm (1.9 eV) and 550 nm (2.25 eV), respectively. Strong photoluminescence of monomer was observed while it is completely quenched in the aggregated thin film, as shown in Fig. 3.5 below. Note, that this graph serves only as an illustration, since a solution is compared to a thin film.

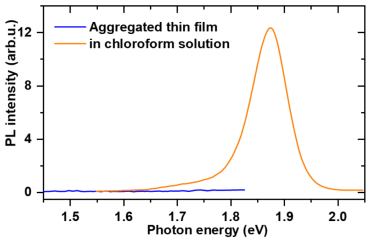

Figure 3.5: Photoluminescence spectra of aggregated and monomer nBSQ. The aggregated thin film (blue) and the monomeric solution in chloroform (orange) both have a maximum optical density of 0.2. The photoluminescent signal of the aggregated thin film is lower than the detection threshold in the expected emission range between 1.5 eV and 1.8 eV.

3.8.5 Transient Absorption Spectra with Excitation of the High Energy Peak at 2.43 eV

Similar spectral shape and dynamics were observed as those excited by 1.73 eV, slightly different ratio between the lower and higher energy was observed, which is due to possible sample inhomogeneity. Fig. 3.6 shows the transient spectra.

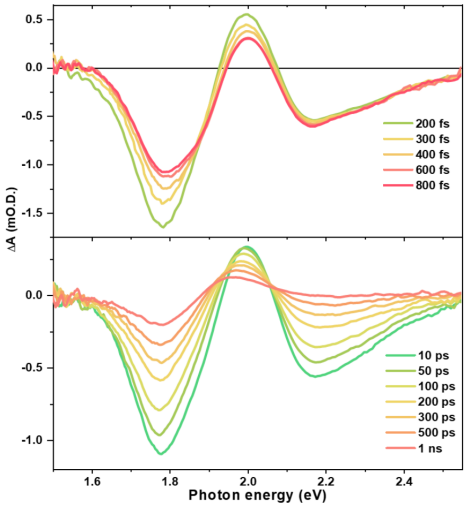

Figure 3.6: Transient absorption spectra of aggregated nBSQ thin film obtained by excitation at 512 nm (2.43 eV). The upper panel shows the first ps time range responses and the lower panel shows responses in ns time range.

3.8.6 Decomposition of the Simulated Transient Absorption Spectra

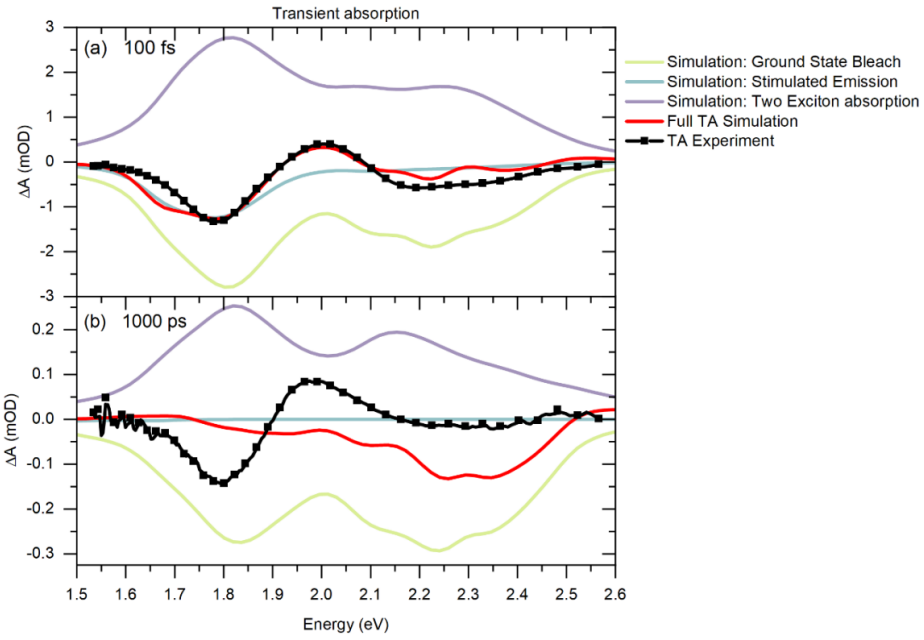

Figure 3.7: Decomposition of the simulated nBSQ transient absorption spectra at a short delay time of 100 fs (a) compared to a long delay time of 1000ps (b). For short delay time (a) the experiment (black squares) shows to minima at 1.8 eV and 2.2 eV respectively, and a peak at 2 eV. The simulated transient absorption spectrum (red solid) is obtained using Eq. 3.7 and follows the same peak structure. At the short time scale of 100 fs the excitation did not yet decay to the dark states resulting in a non-zero stimulated emission signal (blue solid). At long delay times (b), the experiment (black squares) shows a dominant bleach signal at 1.8 eV, a significant two-exciton absorption around 2 eV, and a lack of peaks at higher energies. Our model correctly predicts the lack of stimulated emission (blue solid) at 1000 ps as a result of relaxation to low-energy dark states. The simulated transient absorption spectrum (red solid) and does not concur with the experimental spectra but shows a dominant bleach signal at high energies instead. From this mismatch between experiment and simulation it becomes clear that the long-time dynamics are not captured well by our exciton model and a more sophisticated approach is needed. For example, the transient absorption spectrum may be altered significantly by including inter-molecular charge-transfer states in the Hamiltonian [8, 9].

3.8.7 Simulation of Static Absorption for Different Aggregate Sizes

To understand more the importance of the aggregate size, Fig. 3.8(a) shows the simulated absorbance spectra of nBSQ for different aggregate sizes. The translation vector in all simulations are constant and equal the best fit parameters for n = 10. Both the spectral position and the relative amplitude of the two peaks change severely with the aggregate size. For small aggregate sizes the red-shifted peak is dominant. Increasing the size will lead to a stronger blue-shifted peak, which is dominant for n $>$ 7. The blue-shift also increases with aggregate size.
This can be understood by the increasing amount of non-nearest neighbors. Even though the distance is constantly increasing, the amount of molecules which are further away and likely have a "H-like" angle is increasing with the aggregate size, yielding a stronger overall "H-like" coupling in the Hamiltonian.
Further, Fig. 3.8(b) demonstrates the necessity of disorder to reproduce the optical phenomena obtained from the simulations. In both ordered cases, e.g., staircase and zigzag, the absorbance spectrum and density of states (DOS) reduces to trivial aggregation spectra with a fixed number of n states for n molecules per aggregate. In the staircase configuration all molecules are stacked according to the translation vector (dx,dy,dz), allowing only J-like interactions between molecules. This is reflected by the red-shifted spectrum in Fig. 3.8(b) (red). The relatively narrow DOS region indicates a modest coupling between nearest neighbors, underlining the importance of non-nearest neighbor interaction in the other scenarios. In the zigzag configuration all molecules are stacked with alternating translation vectors (dx,dy,dz) and (-dx,-dy,dz), highly favoring H-like interactions between next-nearest neighbors. As a result, the zigzag configuration shows a blue shifted spectrum in Fig. 3.8(b) (blue). In contrast to the staircase scenario, the H-like non-nearest neighbor contributions increase the exciton band width quite severely, as can be seen by the much broader DOS region.

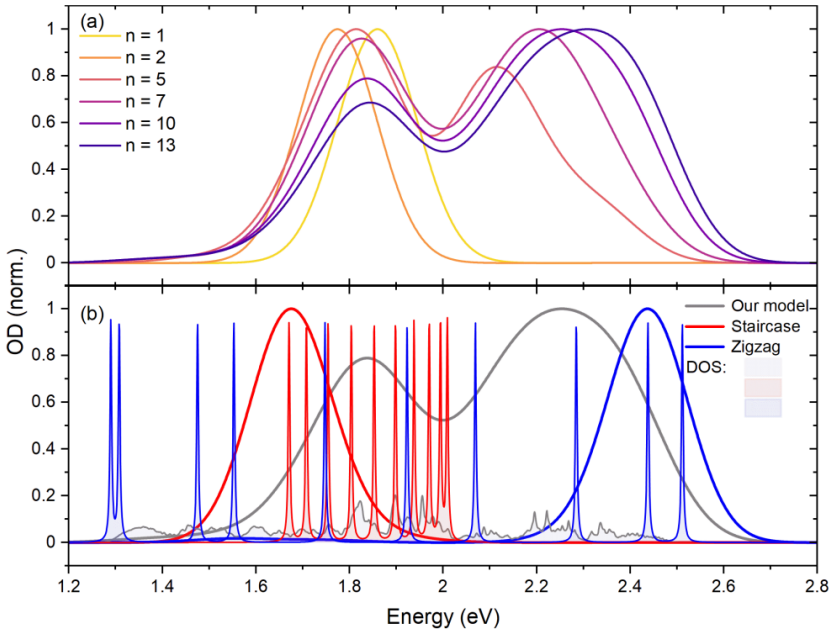

Figure 3.8: (a) simulated absorbance spectra of nBSQ for different aggregate sizes. The best fit "lattice" parameters for n = 10 was used for all presented simulations. (b) Simulated absorbance and DOS spectra for n = 10 for our model, as well as a pure staircase (red) and zigzag (blue) arrangement, devoid of any disorder.

References

(1) Zablocki, J.; Schulz, M.; Schnakenburg, G.; Beverina, L.; Warzanowski, P.; Revelli, A.; Grüninger, M.; Balzer, F.; Meerholz, K.; Lützen, A.; Schiek, M. *The Journal of Physical Chemistry C* **2020**, *124*, 22721–22732.

(2) Bakalis, L. D.; Knoester, J. *The Journal of Physical Chemistry B* **1999**, *103*, 6620–6628.

(3) Lin, Y.-S.; Li, G.-D.; Mao, S.-P.; Chai, J.-D. *Journal of Chemical Theory and Computation* **2013**, *9*, 263–272.

(4) Silbey, R. J. *Journal of the American Chemical Society* **1996**, *118*, 12872–12872.

(5) Weigend, F.; Ahlrichs, R. *Physical Chemistry Chemical Physics* **2005**, *7*, 3297–3305.

(6) Neese, F. *WIREs Computational Molecular Science* **2012**, *2*, 73–78.

(7) Hirata, S.; Head-Gordon, M. *Chemical Physics Letters* **1999**, *314*, 291–299.

(8) Hoffmann, M.; Schmidt, K.; Fritz, T.; Hasche, T.; Agranovich, V. M.; Leo, K. *Chemical Physics* **2000**, *258*, 73–96.

(9) Yamagata, H.; Pochas, C. M.; Spano, F. C. *The Journal of Physical Chemistry B* **2012**, *116*, 14494–14503.

Chapter 4

Exploring the Impact of Intermolecular Charge Transfer and Charge Separation on Transient Optical Properties of Aggregated nBSQ and nBSQ:PCBM Blend Thin Films

This chapter investigates the role of intermolecular charge transfer (ICT) as well as charge separated (CS) states for the transient optical properties of aggregated nBSQ featuring the characteristic double hump steady-state absorption spectrum. We conduct ultrafast transient absorption spectroscopy to probe photoinduced processes in both a pristine nBSQ thin film and in a 2:3 donor-acceptor weight ratio bulk heterojunction blend of nBSQ and $PC_{61}BM$. We observe a derivative-like spectral footprint for both films, which we associate with a photoinduced Stark shift, giving rise to an electroabsorption (EA) signal. For the pristine nBSQ thin film, the strong EA indicates that intermolecular CT states are steering the transient response, especially for delay times longer than the Frenkel exciton lifetime of around 200 ps. Our data show this strongly pronounced photoinduced EA signal to the best of our knowledge for the first time in a single chromophore system. The rise of the EA signal in the blend film after high photoenergy excitation suggests that it is induced by charge separation at the interface of nBSQ and PCBM. Similar rising dynamics have been observed when nBSQ is directly excited at lower photoenergies, although less pronounced, indicating a similar charge separation mechanism. The fast sub-picosecond separation time suggests a delocalized wave function based charge separation mechanism. Our results demonstrate that both intrinsic ICT and injected CS states raise strong transient signals in aggregated nBSQ thin films, and that non-Frenkel-exciton states have to be considered to understand the optical properties of aggregated nBSQ beyond the simple structural disorder model presented in chapter 3.

4.1 Introduction

Kasha theory of Coulomb-coupled molecular aggregates has enjoyed a lot of success since its first proposal more than 60 years ago [1–3]. While it successfully predicted and rationalized the optical properties of many molecular aggregates, it is only a valid approximation if the orbital overlap between neighboring chromophores is small. For aggregates where the orbital overlap is not negligible, the system can no longer be described merely by Frenkel excitons coupled by transition dipole moment interactions, but other contributions such as intermolecular charge transfer (ICT) must be considered [3]. Interactions of hybridized Frenkel/CT excitons have been shown to be able to significantly influence the optical properties of molecular aggregates [4–8]. In many organic or hybrid systems, interfacial charge transfer can also drastically affect the transient properties. This is most notable due to the photoinduced Stark effect, yielding a transient electroabsorption (EA) signal in various donor-acceptor systems [9–16].

In the context of squaraine molecules, especially nBSQ, the role of intermolecular charge transfer states for the absorption properties of molecular aggregates has received a lot of attention on its own [17–23]. While we could show in chapter 3 that the steady-state as well as the early-time spectral transient properties can be understood without considering intermolecular charge transfer states, the dynamical progression of the transient optical signals deviates from a simple Frenkel exciton scheme. In light of this shortcoming, this chapter seeks to investigate the transient footprint of intermolecular charge transfer states as well as charge separation.

To probe the nature of the transient features, we conduct ultrafast transient absorption spectroscopy at different pump wavelengths on two thin films exhibiting the characteristic double hump in the absorption spectrum. One film is a pristine nBSQ-film, whose optical properties are partially shown in chapter 3, while the second sample is a blend of nBSQ and the fullerene-derivate $PC_{61}BM$ (PCBM), which has attracted interest for organic photovoltaic applications [24–29]. The absorptive properties of the nBSQ and PCBM components are complementary, as PCBM is absorbing predominantly at relatively high photon energies in the UV region, while the absorption of nBSQ covers almost the entire visible region as well as a tiny fraction of the infrared region. This allows us to selectively excite one of the two compo-

nents, and therefore observe how different it is in terms of exciton and charge carrier dynamics for the aggregates of nBSQ when we only pump either PCBM or nBSQ. We observe a clear and long-lived derivative-like spectral footprint, which seems universal in both films for any photoexcitation energy. We associate this feature as a photoinduced Stark shift, giving rise to an electroabsorption (EA) signal. To the best of our knowledge, the pristine nBSQ thin film is the first small molecule system consisting of a single chromophore which demonstrates this strong photoinduced EA signal. We assign this EA to semi-delocalized intermolecular charge transfer states, which steer the transient dynamics of the system, especially for delay times longer than the Frenkel exciton lifetime of around 200 ps.
When we excite the blend with higher energy photons, the transient absorption spectrum of the blend thin film is dominated by the electroabsorption signal. The rise of this signal, in contrast to the prompt decay in the pristine nBSQ film, suggests that it is not induced by intermolecular charge transfer inside the nBSQ, but from the charge separation at the interface between nBSQ and PCBM. This charge separation induces a dipolar field in the vicinity of the CS state, yielding a Stark shift. Exciting nBSQ results in an EA signal which partially shows a similar rise, in accordance with the charge separation process. As a result, we assume that the mechanism of charge separation at the nBSQ/PCBM interface should remain identical regardless whether nBSQ or PCBM is excited. The fast charge separation time < 1 ps conforms to a delocalized wave function charge separation process. Our results demonstrate the unique effect of ICT states for nBSQ aggregates as well as charge separation, which both strongly affect the optical properties.

4.2 Methods

4.2.1 Samples

A description synthesis of nBSQ and fabrication of the pristine nBSQ thin film can be found in section 3.5.1. To prepare the 2:3 weight ratio nBSQ:PCBM blend film, nBSQ (homemade by the group of Prof. Lützen at University of Bonn) and PCBM (Solenne BV) was dissolved in amylene-stabilized chloroform (Sigma Aldrich) in a weight ratio of 2:3 and yielding a total concentration of 15 mg/ml. The blend solution was then

spin-coated onto a float glass substrate in a glovebox under Nitrogen atmosphere. After the spin-coating, the ca. 30 nm thick blend thin film was transferred onto a hot plate in the same glovebox and was annealed at 90 °C for 90 minutes to ensure a stable and fully aggregated sample.

4.2.2 Steady-State Absorption Measurements

Steady-state absorbance spectra were recorded using a Lambda 1050 absorption spectrometer (PerkinElmer) at ambient conditions (≈ 22 °C). Thin film absorption spectra have been corrected for the substrate response via mounting a bare glass substrate in the light path of the reference beam.

4.2.3 Transient Absorption Spectroscopy

Femtosecond transient absorption spectroscopy was conducted using the same setup described in section 3.5.3. 715 nm (1.73 eV), 510 nm (2.43 eV) and 400 nm (3.1 eV) have been chosen as excitation wavelengths to selectively excite either only nBSQ (715 nm, 510 nm) or only PCBM (400nm) with a temporal resolution of 100-150 fs. While the two lower photon energy pump beams were generated in the optical parametric amplifier as described in the previous chapter, the 400 nm pump has been generated via second harmonic generation of the 800 nm fundamental beam in a β-BBO crystal, leading to a narrower spectral profile (FWHM ≈ 5 nm). All pump beams have been attenuated to roughly 2.7 nJ per pulse.

4.3 Results

4.3.1 Steady-state Absorption

The steady-state absorption spectra of the pristine nBSQ and blend films investigated are shown in Fig. 4.1, together with the spectrum of a pure PCBM thin film. The absorption spectrum of the blend can be divided into two regimes: lower energies below 2.5 eV, where the absorption arises mostly from nBSQ molecules, and higher energies above 2.5 eV, where PCBM dominates the absorption spectrum. Especially in the higher energy regime, the shapes of the absorbance spectra of the blend and the PCBM thin film look remarkably similar.

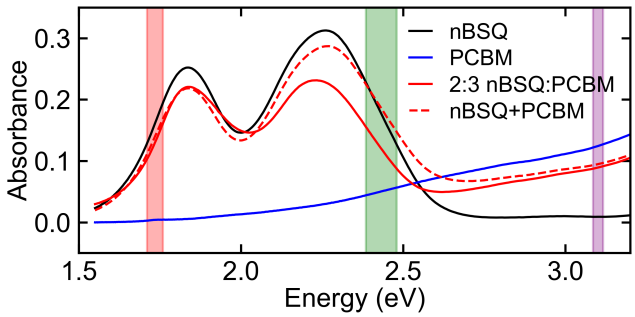

Figure 4.1: (a) Steady-state absorbance spectra of a pure nBSQ thin film annealed at 90°C (black), a PCBM thin film (blue), nBSQ:PCBM (2:3) blend thin film annealed at 90°C (red) and the rescaled sum of the two pure thin films (dashed line in red). The vertical bars around at 1.73 eV (715 nm), 2.43 eV (510 nm), and 3.1 eV (400 nm) indicate the three different photon energies/wavelengths chosen for photoexcitation in the transient absorption spectroscopy measurements conducted in this study.

In the lower energy regime, the different degrees of aggregation in the pure nBSQ and the blend film become evident. On first glance, the 2:3 nBSQ:PCBM blend portrays a similar absorbance spectrum to the pure nBSQ thin film, including the characteristic broad double hump absorbance profile. While the peak positions of the double hump spectra of pure and blend films are very similar, the relative amplitude of the blue-shifted peak with respect to the red-shifted peak is reduced in the 2:3 blend, even though the blue-shifted peak includes a background contribution from the absorbance of the PCBM. The difference becomes more evident when comparing the blend's absorbance spectrum to the sum of the two pure film's absorbance spectra (dashed red line in Fig. 4.1). Furthermore, only the low energy hump has the exact spectral position in both samples at an energy of 1.837 eV, while the high energy hump of the blend film at 2.234 eV is slightly red-shifted by 28 meV with respect to the pristine nBSQ thin film (2.262 eV). Since both position and relative amplitude of the high energy absorption hump are sensitive to the aggregation size (see section 3.8.7), this suggests a slightly lower degree of aggregation compared to the pristine nBSQ thin film. Overall, the presence of PCBM in the blend seems to change the steady-state optical properties of the nBSQ component only slightly, suggesting big donor and acceptor domains.

4.3.2 Transient Absorption Spectra

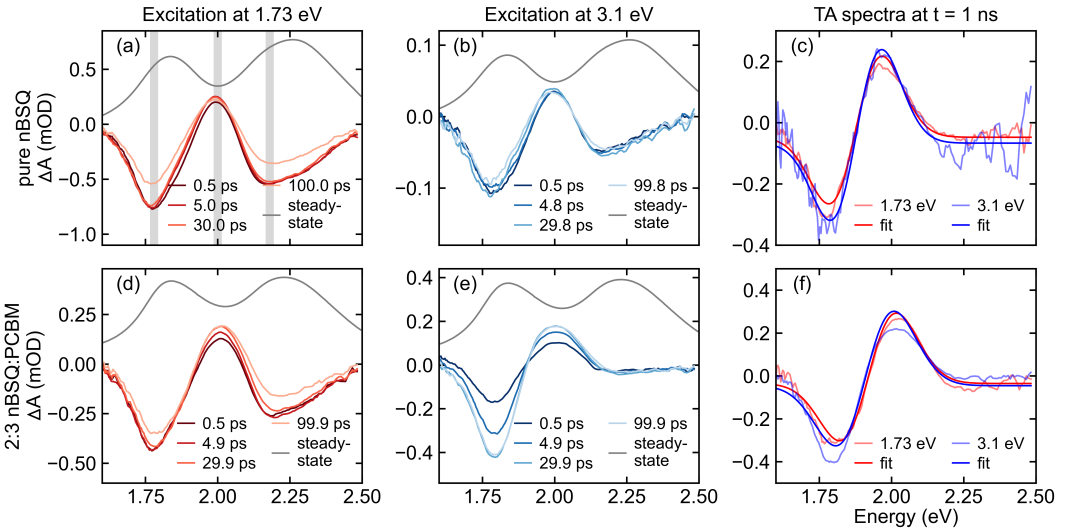

Figure 4.2: Transient absorption spectra of a pure nBSQ thin film and a 2:3 nBSQ:PCBM thin film for photoexcitations at 1.73 eV (a,d) and 3.1 eV (b,e), with a fluence of 280 mW/cm^2. The steady-state absorbance spectra of the corresponding film is shown as reference, and are not to scale. Grey bars in (a) indicate the spectral positions of the main transient features. (c,f) Original and fitted transient spectra for a long delay time of 1 ns of the pure nBSQ thin film, and the 2:3 blend, respectively. For better comparability, amplitudes of each spectrum have been manually rescaled before fitting and do not reflect actual amplitudes.

The transient spectra for the pure nBSQ and the blend thin film are shown in Fig. 4.2. The transient spectra of pure nBSQ, as seen in Fig. 4.2(a) and Fig. 4.6 in the Supplementary Information, corresponds to the transient response shown in the previous chapter. As reported before, the transient spectrum does not resemble a pure ground state bleach (GSB) spectrum. The amplitude of the low energy bleach feature is unproportionally large compared to the high energy bleach, and a photoinduced absorption (PIA) signal appears in between the two humps at around 2 eV.
Surprisingly, there is a feasible transient response of the pure nBSQ thin film upon photoexcitation at 3.1 eV (Fig. 4.2(b)), even though the steady-state absorbance of the thin film in this photon energy region is only 0.009, which is roughly 17 times weaker than the absorbance around 1.73 eV. Accounting for the increased photon

flux of lower energy photons at constant fluence, the difference in absorbed photons should amount to a factor of roughly 32. This is much larger than the observed relative amplitude of the low energy bleach signal at roughly 0.1 mOD, compared to 0.7 mOD peak amplitude observed for photoexcitation at 1.73 eV. The surprisingly large amplitude of the 3.1 eV photoexcitation transient response might indicate that the absorbance at high photon energies might have significant out-of-plane polarization, which can increase the absorption of the samples in a non-collinear pump-probe geometry. Besides the surprisingly high amplitude of the transient signal under high energy photoexcitation, the shapes of the transient absorption spectra are remarkably similar to each other. This suggests the both photoexcitation energies populate the same excitonic state shortly after photoexcitation.

For lower energy photoexcitation at 1.73 eV, the transient absorption spectra of the 2:3 nBSQ:PCBM blend thin film (Fig. 4.2(b)) are remarkably similar to the ones of the pristine nBSQ thin film. Both the positive photoinduced absorption peak at medium energies as well as the low and high energy bleach signals are highly comparable to the transient features of pure nBSQ. Moreover, the signal is largely indifferent to photoexcitation at either hump of the nBSQ absorption profile (see Fig. 4.6, SI). This is in line with the expectation that photoexcitation at 1.73 eV predominantly excites the nBSQ component in the blend film directly, yielding an almost identical spectral response with respect to the pure nBSQ thin film.

The transient response of the 2:3 blend deviates from the pure nBSQ thin film for a higher energy photoexcitation at 3.1 eV, which we associate with the direct excitation of PCBM (Fig. 4.2(d)). Instead of the three features observed before (indicated by grey vertical bars in (Fig. 4.2(a))), only two strong features appear: a bleach-like signal at around 1.8 eV as well as a photoinduced absorption signal at around 2 eV, both features considerably broad. These dominating features are in line with the low energy bleach signal and the mid-energy photoinduced absorption of the pristine film spectra, while the high energy bleach peak at 2.2 eV is only faintly present (see Fig. 4.7 in the SI).

These transient features yield a first-derivative-like shape of the transient absorption, which is similar in shape to the long delay time spectra at 1 ns of the other three measurements, which all demonstrate a derivative-like feature of a gaussian line with a central energy between 1.87 and 1.91 eV, which is close to the peak position of the

red-shifted hump, as well as the peak position of the monomer absorbance of nBSQ. As this shape emerges at delay times significantly longer than the exciton lifetime (roughly 200 ps, see section 3.6.1), it must be of non-Frenkel-exciton origin. The spectral similarity of the blend's transient response to the long lifetime, non-Frenkel exciton response of the pristine nBSQ thin film suggests that exciting PCBM at 3.1 eV does not yield an (Frenkel) excitonic response of nBSQ. Due to the HOMO-LUMO energy alignment of the two components, the origin of the transient response might be of charged nature. This interpretation is further underlined by the evident rise time of both spectral features, which is visible only for 3.1 eV photoexcitation of the blend film.
Due to its affiliation with charge separation and the derivative-like spectral shape, we ascribe the long delay time transient feature observed in all measurements to be induced by electroabsorption, as has been observed often before, mostly in the context of organic donor:acceptor blends [9–11, 30]. Further proof for this claim can be found from the dynamics of the transient response, which will be discussed in the following section.

4.3.3 Dynamics

Fig. 4.3(a,b) shows the overall dynamics of the high energy bleach signal for two different excitation energies. On longer timescales (>10 ps) all high energy bleach curves exhibit a monotonic decay and can be fitted by a single exponential decay function. A summary of the fit parameters of the high energy bleach signals is presented in Table 4.1 ("HB"). Especially for the low photon energy excitation at 1.73 eV, high energy bleach signals of the pure nBSQ film and the blend films show a high degree of similarity in terms of lifetimes, with decay times of 219(±5) ps and 199(±7) ps, respectively. As the high energy ground state bleach is regarded as a direct probe for the exciton lifetime (see section 3.6.1), we attribute the fitted decay times to the exciton lifetimes of the sample. The slightly shorter lifetime of the excitons in the blend suggests that there might be additional or modified relaxation channels due to the presence of PCBM.
The slightly shorter exciton lifetime of the blend compared to the pristine nBSQ thin film is also observed for 3.1 eV photoexcitation (252(±13) ps vs. 175(±31) ps). Note

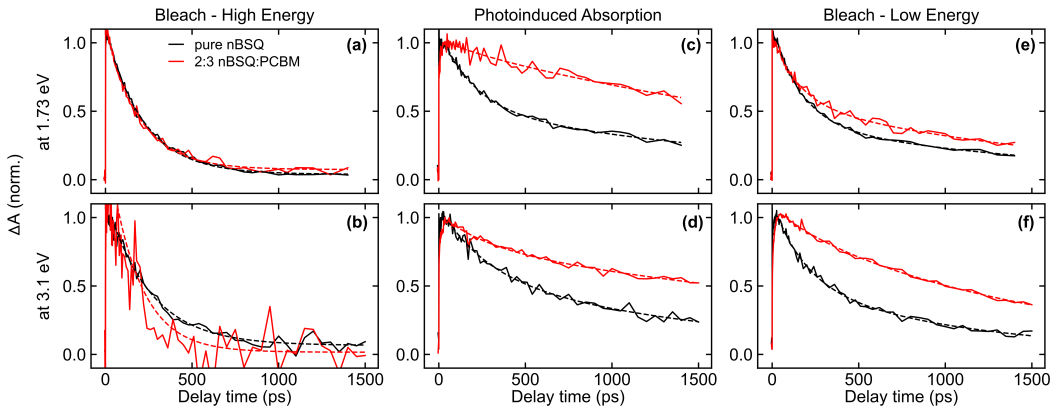

Figure 4.3: Transient dynamics of the three main features (vertical bars in Fig. 4.2(a)) of the pure nBSQ thin film (black) and 2:3 nBSQ:PCBM blend thin films (red) for photoexcitation energies of 1.73 eV and 3.1 eV. Dashed lines show the fits of the long delay time dynamics. The decay lines were obtained by integrating a 10 nm band around the maximum of each feature. Bleach dynamics have been normalized to positive values for easier comparison to the PIA signal

that the blend's very weak high energy bleach signal results in noisy, but detectable dynamics. Due to the instantaneous appearance of the high energy bleach signal, photoexcitation of the blend at 3.1 eV also immediately excites nBSQ, even though the contribution is minor compared to the non-Frenkel exciton related transient features at lower energies.

Unlike the high energy bleach dynamics, the dynamics of both PIA and low energy bleach signals show significant differences between pure nBSQ film and blend. For excitation at 1.73 eV (Fig. 4.3(c)), the dynamics of the PIA signal of the blend clearly deviates from that of the pure nBSQ film's signal, as the signal decays much slower. A similar trend is observed for the low energy bleach signal (Fig. 4.3(e)) for delay times longer than the exciton lifetime, once the contribution from the GSB vanishes. For higher energy photoexcitation (3.1 eV), both PIA and low energy bleach signal of the blend show much longer lifetimes compared to those of the pristine nBSQ thin film.

Table 4.1: Long Time Dynamics of the pure nBSQ Thin Film and the Blend Thin Film ("HB": high energy bleach, "LB": low energy bleach, "PIA": photoinduced absorption). Δ denotes the confidence interval of the fitting parameter above.

Pure nBSQ Thin Film

Data	A_1	t_1(ps)	A_2	t_2(ps)
HB, 1.73 eV	1.06	219	0.0393	—
Δ	0.01	5	0.0052	—
PIA, 1.73 eV	0.568	198	0.53	2090
Δ	0.04	25	0.049	390
LB, 1.73 eV	0.704	165	0.421	1640
Δ	0.019	9	0.024	160
HB, 3.1 eV	1.08	252	0.0657	—
Δ	0.02	12	0.0112	—
PIA, 3.1 eV	0.473	260	0.61	1590
Δ	0.132	88	0.148	470
LB, 3.1 eV	0.578	187	0.535	1090
Δ	0.058	29	0.07	150

Blend Thin Film

Data	A_1	t_1(ps)	A_2	t_2(ps)
HB, 1.73 eV	1.01	199	0.0742	—
Δ	0.02	7	0.0076	—
PIA, 1.73 eV	0.0455	188	0.984	2830
Δ	0.0648	573	0.082	660
LB, 1.73 eV	0.469	150	0.577	1700
Δ	0.037	28	0.047	260
HB, 3.1 eV	1.58	175	0.0163	—
Δ	0.15	31	0.0462	—
PIA, 3.1 eV	0.222	259	0.8074	3410
Δ	0.053	101	0.062	697
LB, 3.1 eV	0.105	223	0.974	1510
Δ	0.045	141	0.053	100

The differences between these transient features of pure nBSQ and blend thin film is reflected in the obtained fit parameters. All high energy bleach signals could be fitted using a single exponential All PIA and low energy bleach signals measured could be fitted using biexponential decay functions yielding two vastly different decay times ($\tau_{fast} \approx 200$ ps; $\tau_{slow} \approx 2$ ns)(see Table 4.1 "LB" and "PIA"). For the low energy bleach and PIA of the pure film at 1.73 eV photoexcitation, the relative amplitudes of the fast (A_f) and slow component are similar ($A_{f,PIA}^{nBSQ,1.73eV} = 0.52(\pm 0.04)$, $A_{f,LB}^{nBSQ,1.73eV} = 0.63(\pm 0.02)$). The relative amplitudes of the fast components are drastically reduced for the corresponding blend features ($A_{f,PIA}^{blend,1.73eV} = 0.04(\pm 0.06)$, $A_{f,LB}^{blend,1.73eV} = 0.45(\pm 0.04)$).

Similar observations can be made for photoexcitation at 3.1 eV. While the relative amplitude of the faster decay component of the pristine nBSQ film is roughly within the same range as the slower decay component ($A_{f,PIA}^{nBSQ,3.1eV} = 0.44(\pm 0.12)$, $A_{f,LB}^{nBSQ,3.1eV} = 0.52(\pm 0.05)$), the slower decay component becomes dominant for the blend ($A_{f,PIA}^{blend,3.1eV} = 0.21(\pm 0.05)$, $A_{f,LB}^{blend,3.1eV} = 0.1(\pm 0.04)$).

As the decay time corresponds well to the exciton lifetime extracted for the high energy bleach features, we assign the fast component of the dynamics of low energy bleach and photoinduced absorption to Frenkel-exciton related, and the slower component to be charged-state related. This is in line with the lower relative amplitude of the fast component of the blend dynamics at high energy photoexcitation, as only a limited amount of nBSQ molecules should be excited.

Furthermore, the similar dynamics at the spectral positions of the low energy bleach and PIA at long delay times throughout all measurements are in agreement with the assignment of electroabsorption signal [10].
The origin of the electroabsorption signal becomes more evident from the early time

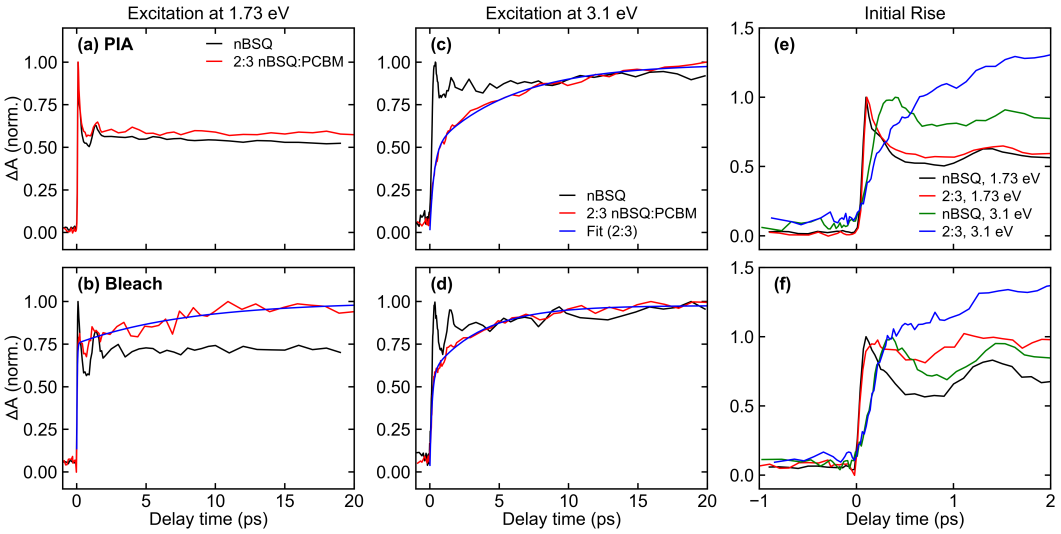

Figure 4.4: (a-d) Early delay time dynamics of the two EA related features (top row: bleach, bottom row: PIA) of the pure nBSQ thin film (black) and 2:3 nBSQ:PCBM blend thin films (red) for photoexcitation energies of 1.73 eV and 3.1 eV. Where applicable, the growth of the dynamics has been fitted. (e,f) Comparison of the initial rise of the signal around time zero for the low energy bleach and the photoinduced absorption, respectively.

dynamics, as reported in Fig. 4.4. Both the low energy bleach (Fig. 4.4(a,c)) as well as the PIA (Fig. 4.4(b,d)) of the pristine nBSQ thin film (black lines) demonstrate an instantaneous response to photoexcitation at either 1.73 eV or 3.1 eV. Following the initial excitation, no further rise in the signal can be observed. On the contrary, the respective dynamics of the blend (red lines) demonstrate a rise in the first picoseconds after initial photoexcitation. This is especially pronounced for the 3.1 eV excitation, showing unambiguously that the majority of excitation happens in PCBM, with the rise time signaling a charge transfer from the PCBM into the nBSQ [10, 31].
The rise of the low energy bleach and PIA features in the blend when excited at 3.1 eV can be accounted for by a fit function including two rising components of different rise times, see section 4.7.3. For the blend's PIA/bleach at 3.1 eV, the two

rise times are 153(±8) fs/295(±13) fs and 3.65(±0.36) ps/5.79(±0.42) ps. Both rise times have similar relative amplitudes. It is worth noting that the faster rise component is edging the time-resolution of the experiment and is partially in line with the "rise" of the dynamics of the pure nBSQ film. Therefore, the faster rise time might not represent a reliable quantitative measure for a physical process.

The blend's dynamics at 1.73 eV excitation are more complicated, as only the PIA signal shows a rising component, while a prompt response is clearly visible. Consequently, the PIA dynamics can be fitted by an instantaneous response giving more than 75% of the signal, in addition to a rising component with a rise time of 8.1(±2.6) ps.

The simultaneous appearance of a rising signal akin to the PCBM-excitation induced dynamics and an instantaneous response suggests that the electroabsorption signal of the blend at 1.73 eV photoexcitation comes from two different sources: an intrinsic charged state inside nBSQ, as well as another state injected from the interface with PCBM.

The difference between the intrinsic and injected electroabsorption signal is further

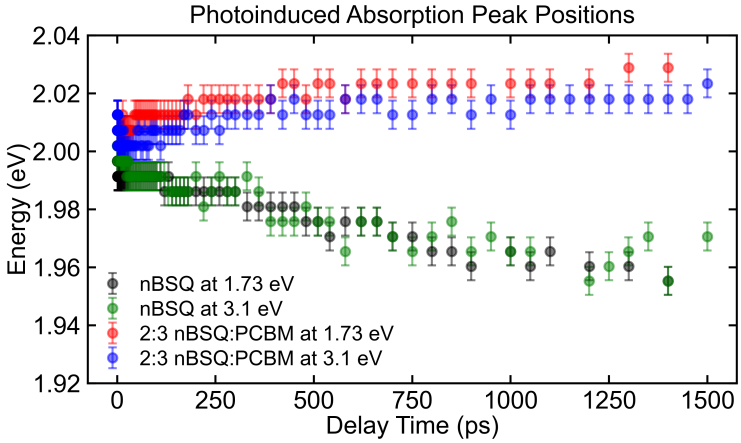

Figure 4.5: Comparison of the peak positions of the photoinduced absorption signal as a function of delay times for both pure nBSQ and blend thin films, for photoexcitations of 1.73 eV and 3.1 eV. Before extracting the peak positions, the TA spectra were smoothed using a Savitzky-Golay-filter to yield a clearer visualization without fundamental changes to the shape of the TA spectra and the position of the corresponding peaks.

highlighted by the peak positions of the PIA signal as a function of time, as seen

in Fig. 4.5. While the energies of photoexcitation seem to not significantly influence the peak positions over time, clearly different trends can be observed for the blend and the pure nBSQ film. While both PIA signals are initially very close to 2 eV, the pure nBSQ thin film's PIA signal shows a consistent red-shift in energy with progressing delay time. This shift might either arise from the diminishing contribution of the low energy ground state bleach for longer delay times, or from reduced photoinduced electric fields, either due to charge migration or recombination [31] of the intrinsic charged states. In contrast, the blend shows a miniscule blue-shift over the first 500 ps, eventually stopping for longer delay times. These opposite trends underline the different spectral signatures of the intrinsic and injected charged state populations.

4.4 Discussion

The photoinduced electroabsorption signal of the low energy hump seems to be a universal component of the transient response of nBSQ thin films adopting the "double hump" aggregate structure, in both pristine nBSQ and the 2:3 weight ratio nBSQ:PCBM blend. The derivative-like feature is strongly present in all datasets collected, and its amplitude is comparable to the ground state bleach and two-exciton absorption signal of Frenkel-excitons, as discussed in chapter 3.

Photoinduced electroabsorption signals are commonly associated with charge separated states in organic donor-acceptor blends [9, 10, 31, 32], as well as dye-sensitized solar cells [16], bacterial reaction centers [33], and polymer blends [12]. In the context of organic donor-acceptor blends in particular, the electroabsorption signal has been explained by the local dipolar field of a separated electron-hole pair acting on its surrounding. Therefore, we can discuss the EA-affiliated dynamics in the context of charge-separation [9, 10, 31].

The vastly different time scales of the two rising component of the EA-affiliated signals after photoexcitation at 3.1 eV indicate two charge-separation-related processes. The sub-ps time scale of the fast charge separation process, which is partially shorter than the instrument response function of the experiment, is in agreement with the time scale of delocalized wave function charge separation previously reported for different donor-acceptor blends [9, 10, 34]. The slower rising component has been

assigned to the increased electric field caused by further propagation of the hole away from the interface giving rise to a larger photoinduced EA response [10]. Alternatively, the slower rise time might be related to delayed dissociation of tightly bound CT states at the interface into CS states or diffusion of the excitons towards the interface [31].
The decay of the CS-related EA signal observed in the blend film might originate from several mechanisms: Both geminate and non-geminate recombination, trap filling, and charge diffusion. The latter might be unrealistic given the reported low hole mobility of the blend [35, 36]. Further studies might be able to resolve the exact mechanism.
Contrary to the well reported EA footprint in donor-acceptor blends, the appearance of a strong EA signal for the pristine nBSQ thin film is not a commonly observed phenomenon. To the best of our knowledge, pristine nBSQ thin films are the only small molecule systems consisting of a single chromophore showing a strong transient EA response.
In the absence of an electron acceptor, intermolecular charge transfer states represent a suitable candidate for the origin of the EA response [17]. As mentioned by Gelinas *et al.* [10], Scarongella *et al.* [37], and Gasparini *et al.* [31], transient EA signals are only significant if the electron-hole pair is sufficiently separated and not tightly bound to neighboring molecules. This condition is met both for non-nearest neighbor CT-states as well as CS-states. In the context of pristine nBSQ, this insinuates that the ICT states responsible for the strong EA signal are not tightly bound nearest neighbor ICT states, but ICT states extended over several molecules. This underlines once more that nBSQ aggregates adopting the "double hump" absorption profile are large-scale aggregates far beyond simple dimer considerations.
Our data do not provide a clear assignment of the decay mechanism(s) of the ICT states. The decay of the ICT states is comparable to the decay of the CS states in the blend in terms of lifetime. Thus, trap filling might be a common relaxation mechanism. However, ICT states may also undergo geminate recombination or dissociation into separated charges.
Curiously, the spectral position of the EA signal is confined to energies close to the low energy hump and the monomer absorbance energy of nBSQ, both in the pristine nBSQ and blend thin film. This is in accordance with the strong susceptibility of

J-aggregating systems to Stark shifts, which have been observed before [32, 38, 39]. This observation is in line with the disordered chain-like aggregate model discussed in chapter 3, which also yields J-like aggregation footprints as part of the aggregate ensemble. The absence of a simultaneous EA response of the H-peak remains elusive, as the electric field might affect low and high energy excitonic states differently due to modified Coulomb interactions, like weaker Coulombic coupling of neighboring molecules [40]. Further theoretical investigation is needed to fully understand electric field induced effects on the different humps.

Overall, the strong transient influence of the ICT states complements previous shortcomings of the structural disorder model (see section 3.8.6), which can only reproduce early time transient spectra, but cannot reproduce the dynamics and progression of the spectrum. This suggests that for the transient response of aggregated nBSQ thin films, intermolecular charge transfer indeed plays an important role, especially for time scales longer than 200 ps.

To support our claims regarding the unique electroabsorption of ICT states in pristine nBSQ thin films and CS states in the nBSQ:PCBM blend, further experimental evidence is needed. In the following, we list potentially helpful experimental methods which are beyond of scope for this study.

Two-photon absorption spectroscopy might resolve why nBSQ aggregates show an excitonic response at 3.1 eV photoexcitation. Steady-state Stark spectroscopy might further validate the EA assignment of the transient features and could reveal the EA response of the high energy hump. Furthermore, widening the spectral range of the transient absorption measurements might collect more compelling evidence for the nature of the charged states in the blend film. Extending the TA study into the infrared region allows the probing of potential photoinduced absorption signals of polarons, while extending into the UV region might enable the observation of spectral features of PCBM. Monitoring the temperature dependence of the rise time might also reveal the nature of the slow rise time of the EA signal in the blend film, as purely delocalized wave function driven charge separation has been observed to be temperature independent [10], while dissociation of interfacial CT states has a distinct temperature dependence [41].

Since the rate of non-geminate recombination is population dependent, a fluence-dependent transient absorption study might reveal the exact nature of the CS state

decay. Such a study was not possible using our setup, due to the low signal-to-noise ratio and the degradation of the sample when it is exposed to intense 400 nm light(see Fig. 4.8).

4.5 Conclusions

In conclusion, we have systematically conducted ultrafast transient absorption spectroscopy on pristine nBSQ and nBSQ:PCBM blend films to reveal the impact of ICT and CS states for the transient properties of aggregated nBSQ. All transient spectra demonstrate a signal akin of an electroabsorption signal around the low energy hump, irrespective of the photoexcitation energy and the presence of PCBM. Our results suggest that electroabsorption is a universal feature of the transient response of aggregated nBSQ thin films, and that intermolecular charge transfer states play an important role for the ultrafast dynamics. Aggregated nBSQ thin films are the first known single-chromophore system portraying this strong photoinduced EA response.
For the blend of nBSQ and PCBM, we observe that the Frenkel exciton lifetime of nBSQ is not strongly influenced by the presence of PCBM, while CS states emerge due to the donor-acceptor interactions. The transient EA response of the blend originates from both the ICT states inside the nBSQ component as well as spatially separated electron-hole pairs inducing a Stark effect in their environment. The fast rise time of the CS response indicates a delocalized wave function driven charge separation. Our study underlines the importance of non-Frenkel-exciton states for the optical properties of nBSQ aggregates beyond the steady-state absorption.

4.6 Contributions

Robin Bernhardt, Jingyi Zhu and Manuela Schiek conceived the project. Robin Bernhardt, Lukas Rieland, Jingyi Zhu and Tianyi Wang performed the steady-state and transient optical experiments and analyzed the experimental results. Jennifer Zablocki and Arne Lützen synthesized the squaraine molecules. Manuela Schiek, Dirk Hertel and Klaus Meerholz prepared and characterized the thin film samples. Paul van Loosdrecht supervised the project.

References

(1) Kasha, M. *Radiation Research* **1963**, *20*, 55–70.

(2) Kasha, M.; Rawls, H. R.; Ashraf El-Bayoumi, M. *Pure and Applied Chemistry* **1965**, *11*, 371–392.

(3) Hestand, N. J.; Spano, F. C. *Chemical Reviews* **2018**, *118*, 7069–7163.

(4) Kazmaier, P. M.; Hoffmann, R. *Journal of the American Chemical Society* **1994**, *116*, 9684–9691.

(5) Hoffmann, M.; Soos, Z. G. *Physical Review B* **2002**, *66*, 024305.

(6) Hoffmann, M.; Schmidt, K.; Fritz, T.; Hasche, T.; Agranovich, V. M.; Leo, K. *Chemical Physics* **2000**, *258*, 73–96.

(7) Yamagata, H.; Pochas, C. M.; Spano, F. C. *The Journal of Physical Chemistry B* **2012**, *116*, 14494–14503.

(8) Hestand, N. J.; Yamagata, H.; Xu, B.; Sun, D.; Zhong, Y.; Harutyunyan, A. R.; Chen, G.; Dai, H.-L.; Rao, Y.; Spano, F. C. *The Journal of Physical Chemistry C* **2015**, *119*, 22137–22147.

(9) Tamai, Y.; Fan, Y.; Kim, V. O.; Ziabrev, K.; Rao, A.; Barlow, S.; Marder, S. R.; Friend, R. H.; Menke, S. M. *ACS Nano* **2017**, *11*, 12473–12481.

(10) Gélinas, S.; Rao, A.; Kumar, A.; Smith, S. L.; Chin, A. W.; Clark, J.; van der Poll, T. S.; Bazan, G. C.; Friend, R. H. *Science* **2014**, *343*, 512–516.

(11) Koch, M.; Myahkostupov, M.; Oblinsky, D. G.; Wang, S.; Garakyaraghi, S.; Castellano, F. N.; Scholes, G. D. *Journal of the American Chemical Society* **2017**, *139*, 5530–5537.

(12) Umar, A. R.; Dorris, A. L.; Kotadiya, N. B.; Giebink, N. C.; Collier, G. S.; Grieco, C. *The Journal of Physical Chemistry C* **2023**, *127*, 9498–9508.

(13) Tran, N. L.; Elkins, M. H.; McMeekin, D. P.; Snaith, H. J.; Scholes, G. D. *The Journal of Physical Chemistry Letters* **2020**, *11*, 10081–10087.

(14) Orrit, M.; Bernard, J.; Zumbusch, A.; Personov, R. I. *Chemical Physics Letters* **1992**, *196*, 595–600.

(15) Kanemoto, K.; Domoto, S.; Hashimoto, H. *The Journal of Physical Chemistry C* **2014**, *118*, 17260–17265.

(16) Meister, M.; Baumeier, B.; Pschirer, N.; Sens, R.; Bruder, I.; Laquai, F.; Andrienko, D.; Howard, I. A. *The Journal of Physical Chemistry C* **2013**, *117*, 9171–9177.

(17) Hestand, N. J.; Zheng, C.; Penmetcha, A. R.; Cona, B.; Cody, J. A.; Spano, F. C.; Collison, C. J. *The Journal of Physical Chemistry C* **2015**, *119*, 18964–18974.

(18) Bernhardt, R.; Manrho, M.; Zablocki, J.; Rieland, L.; Lützen, A.; Schiek, M.; Meerholz, K.; Zhu, J.; Jansen, T. L. C.; Knoester, J.; van Loosdrecht, P. H. M. *Journal of the American Chemical Society* **2022**, *144*, 19372–19381.

(19) Wiegand, T.; Smith, H.; Ryczek, C.; Cruz, A.; Cody, J.; Collison, C. J.; Burson, K. *The Journal of Physical Chemistry C* **2022**, *126*, 14791–14800.

(20) Sanyal, S.; Painelli, A.; K. Pati, S.; Terenziani, F.; Sissa, C. *Physical Chemistry Chemical Physics* **2016**, *18*, 28198–28208.

(21) Zhong, C.; Bialas, D.; Collison, C. J.; Spano, F. C. *The Journal of Physical Chemistry C* **2019**, *123*, 18734–18745.

(22) Shen, C.-A.; Bialas, D.; Hecht, M.; Stepanenko, V.; Sugiyasu, K.; Würthner, F. *Angewandte Chemie* **2021**, *133*, 12056–12065.

(23) Kim, J. H.; Liess, A.; Stolte, M.; Krause, A.-M.; Stepanenko, V.; Zhong, C.; Bialas, D.; Spano, F.; Würthner, F. *Advanced Materials* **2021**, *33*, 2100582.

(24) C. Deing, K.; Mayerhöffer, U.; Würthner, F.; Meerholz, K. *Physical Chemistry Chemical Physics* **2012**, *14*, 8328–8334.

(25) Spencer, S.; Cody, J.; Misture, S.; Cona, B.; Heaphy, P.; Rumbles, G.; Andersen, J.; Collison, C. *The Journal of Physical Chemistry C* **2014**, *118*, 14840–14847.

(26) Spencer, S. D.; Bougher, C.; Heaphy, P. J.; Murcia, V. M.; Gallivan, C. P.; Monfette, A.; Andersen, J. D.; Cody, J. A.; Conrad, B. R.; Collison, C. J. *Solar Energy Materials and Solar Cells* **2013**, *112*, 202–208.

(27) Chen, G.; Sasabe, H.; Lu, W.; Wang, X.-F.; Kido, J.; Hong, Z.; Yang, Y. *Journal of Materials Chemistry C* **2013**, *1*, 6547–6552.

(28) Brück, S.; Krause, C.; Turrisi, R.; Beverina, L.; Wilken, S.; Saak, W.; Lützen, A.; Borchert, H.; Schiek, M.; Parisi, J. *Physical Chemistry Chemical Physics* **2014**, *16*, 1067–1077.

(29) Zablocki, J. *PhD Thesis, University of Bonn* **2022**.

(30) Cabanillas-Gonzalez, J.; Virgili, T.; Gambetta, A.; Lanzani, G.; Anthopoulos, T. D.; de Leeuw, D. M. *Physical Review Letters* **2006**, *96*, 106601.

(31) Gasparini, N.; Camargo, F. V. A.; Frühwald, S.; Nagahara, T.; Classen, A.; Roland, S.; Wadsworth, A.; Gregoriou, V. G.; Chochos, C. L.; Neher, D.; Salvador, M.; Baran, D.; McCulloch, I.; Görling, A.; Lüer, L.; Cerullo, G.; Brabec, C. J. *Nature Communications* **2021**, *12*, 1772.

(32) Wiederrecht, G. P.; Giebink, N. C.; Hranisavljevic, J.; Rosenmann, D.; Martinson, A. B. F.; Schaller, R. D.; Wasielewski, M. R. *Applied Physics Letters* **2012**, *100*, 113304.

(33) Ma, F.; Romero, E.; Jones, M. R.; Novoderezhkin, V. I.; Yu, L.-J.; van Grondelle, R. *The Journal of Physical Chemistry Letters* **2021**, *12*, 5526–5533.

(34) Bakulin, A. A.; Hummelen, J. C.; Pshenichnikov, M. S.; van Loosdrecht, P. H. M. *Advanced Functional Materials* **2010**, *20*, 1653–1660.

(35) Zheng, C.; Jalan, I.; Cost, P.; Oliver, K.; Gupta, A.; Misture, S.; Cody, J. A.; Collison, C. J. *The Journal of Physical Chemistry C* **2017**, *121*, 7750–7760.

(36) Chen, G.; Si, C.; Zhang, P.; Wei, B.; Zhang, J.; Hong, Z.; Sasabe, H.; Kido, J. *Organic Electronics* **2017**, *51*, 62–69.

(37) Scarongella, M.; De Jonghe-Risse, J.; Buchaca-Domingo, E.; Causa', M.; Fei, Z.; Heeney, M.; Moser, J.-E.; Stingelin, N.; Banerji, N. *Journal of the American Chemical Society* **2015**, *137*, 2908–2918.

(38) Eilmes, A. *Chemical Physics Letters* **2001**, *347*, 205–210.

(39) Nakata, K.; Kobayashi, T.; Tokunaga, E. *Optical Review* **2010**, *17*, 346–351.

(40) Hestand, N. J.; Spano, F. C. *The Journal of Chemical Physics* **2015**, *143*, 244707.

(41) Marcus, R. A. *The Journal of Chemical Physics* **1956**, *24*, 966–978.

4.7 Supplementary Information

4.7.1 Transient Absorption Spectra upon 2.43 eV Photoexcitation

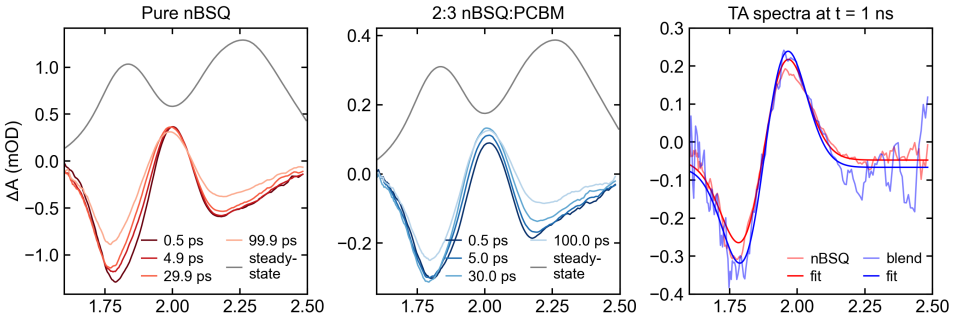

Figure 4.6: Transient Absorption Spectra of both the pure nBSQ and the blend film upon photoexcitation at 2.43 eV, exciting the higher energy absorption hump. The right plot shows the long delay time responses, which describes a derivative-like shape along with fits, in agreement to the data presented in Fig. 4.2

4.7.2 High Energy Bleach of nBSQ:PCBM blend after 3.1 eV Photoexcitation

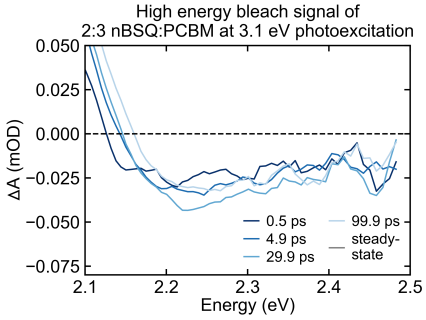

Figure 4.7: Enlarged transient absorption spectrum of the high energy bleach signal of the 2:3 nBSQ:PCBM blend as seen in Fig. 4.2, showing the faint bleach signal.

4.7.3 Photostability of Aggregation

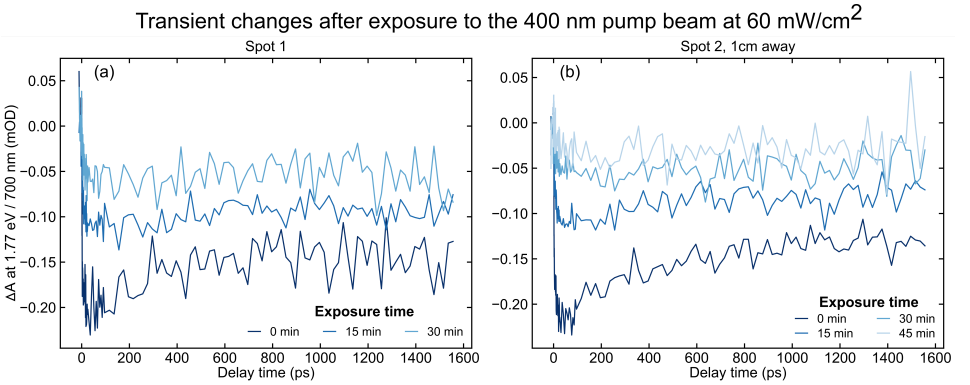

Figure 4.8: Transient changes accompanying the steady-state changes in 2:3 nBSQ:PCBM in two different spots. Repeated scans of the same bleach signal at 1.77 eV (700nm) show a decrease in amplitude of the signal. The decaying of the signal is irreversible, but strictly limited to the spot size of the pump laser, as moving from the first spot of exposure (a) to the second spot 1 cm away (b) can recover the initial amplitude of the signal.

4.7.4 Fit Results of the Dynamic Traces

The long time dynamics of both thin films have been fitted with either mono-exponential or biexponential decay functions (see Table 4.1). When there is no t_2 mentioned, the fit function takes the form

$$y(t) = A_1 \cdot e^{\frac{-t}{t_1}} + A_2. \tag{4.1}$$

Otherwise, the fit function is described as

$$y(t) = A_1 \cdot e^{\frac{-t}{t_1}} + A_2 \cdot e^{\frac{-t}{t_2}}. \tag{4.2}$$

For the blend thin film short time dynamics, two rise functions describe the fit function as

$$y(t) = A_1(1 - e^{\frac{-t}{t_1}}) + A_2(1 - e^{\frac{-t}{t_2}}). \tag{4.3}$$

The error of each fit parameter is denoted as Δ underneath the reported value.

Table 4.2: Short Time Dynamics of the Blend Thin Film.

Data	$\mathbf{A_1}$	$\mathbf{t_1}$ **(ps)**	$\mathbf{A_2}$	$\mathbf{t_2}$ **(ps)**
PIA (1.73 eV)	0.754	0.036	0.245	8.09
Δ	0.012	0.004	0.032	2.657
PIA (3.1 eV)	0.572	0.153	0.404	3.647
Δ	0.013	0.008	0.012	0.355
Bleach (3.1 eV)	0.485	0.295	0.505	5.79
Δ	0.011	0.013	0.011	0.419

Chapter 5

Resolving Aggregate Structure, Exciton Interactions and Ultrafast Dynamics in Thin Films of Chiral Squaraine Molecules

While chirality is a prevalent character of numerous biological and synthetic organic molecules, its selective absorption of circularly polarized light, known as circular dichroism (CD), is typically small due to intrinsically weak coupling between magnetic and electric dipoles. However, thin films of aggregated, enantiopure prolinol-derived squaraine molecules (ProSQ-C16) exhibit an unusually large excitonic CD signal, although the underlying mechanism remains elusive. In this study, we employ steady-state and ultrafast transient absorption spectroscopy to investigate the nature and dynamics of excitons in aggregates of enantiopure and racemic ProSQ-C16 thin films. Transient responses of enantiopure thin films for different excitation energies strongly indicate that a single type of aggregate dominates the linear optical response. This results in a strong red-shifted (J-like) and weak blue-shifted (H-like) absorption band. On the other hand, the transient properties of the racemic thin film deviate from this pattern and remain largely ambiguous. The short lifetime and coherent oscillations present in the dynamics of the transient absorption signal reveal that the early time dynamics are governed by a dark intermediate state, likely of intermolecular charge transfer nature. This non-radiative relaxation path explains the unusually weak fluorescence of the predominately J-like behaving aggregate. Our findings unambiguously show that chirality has a strong impact on the excitonic optical and dynamical response, and underline the significance of non-Frenkel exciton states for the optical properties of anilino squaraine dyes.

5.1 Introduction

The photophysical properties of aggregated natural and synthetic molecular dyes are governed by their excitonic states [1, 2]. These excitonic states are a result of intermolecular interactions [3], which are steered by the packing of the chromophors. Classical molecular exciton theory covers Coulombic interactions (Frenkel excitons) and the formation of archetypical H- and J-aggregates as well as "oblique" aggregates (Davydov splitting [4]). However, both vibronic coupling and intermolecular charge transfer can significantly impact the photophysical properties [5].
Aggregates of quadrupolar anilino squaraine dyes exhibit distinct excitonic absorption signatures within the visible to deep-red spectral range. These exciton states depend on the spatial alignment of the π-conjugated molecular backbones, which is steered by non-chromophoric terminal functionalization patterns. They can be predominately of Frenkel-excitonic nature [6–10] or are hybridized with intermolecular charge transfer [9, 11, 12] and for chiral functionalization also show excitonic circular dichroism [13–18].
Chirality is a symmetry property primarily referring to the structural non-superimposability of an object with its mirror image, which can give rise to optical activity (circular birefringence (CB) and circular dichroism (CD)), as well as circular polarized light emission and spin polarization effects (e.g., chirality-induced spin selectivity (CISS)) [19, 20].
For natural chiral molecular and supramolecular systems, CD is typically a weak effect because it arises from coupling of magnetic and electric dipoles of nearby molecules, which is inherently weak in molecular materials due to their small size compared to the wavelength of visible light [21, 22]. The chiroptical response of engineered materials such as liquid crystals [23], periodic nanostructures [24] and chiral metamaterials [25] is spectroscopically almost indistinguishable from intrinsic CD, even though it arises from a different physical origin, as it is based on spatial dispersion rather than interactions of magnetic and electric dipoles [24], and most importantly it is often several orders of magnitude larger than intrinsic CD. Nevertheless, the development of strongly intrinsically CD-active organic semiconductors for chiroptical applications is an undauntedly active field of research [26–30].
In this context, a group of prolinol-derived anilino squaraines (ProSQs) emerged,

demonstrating a giant intrinsic excitonic CD in dispersed aggregates and thin films [31, 32]. In particular, annealed thin films of enantiopure ProSQ carrying a sixteen carbon atom long terminal alkyl chain (ProSQ-C16) showed an optical dissymmetry factor of ± 0.75 - by far the highest value for small molecule assemblies [32].
Moreover, even the linear absorbance of enantiopure ProSQ-C16 thin films is beyond archetypical H- and J-aggregation. While a strong J-like red-shift of the main absorption band compared to the monomer is observed for this thin film, the fluorescence is surprisingly weak. Furthermore, the line shape of this main absorption band is not symmetric, and a low-amplitude absorbing continuum extending to the weaker blue-shifted absorption band is observed. These optical and excitonic properties of aggregated enantiopure ProSQ-C16 thin films can further be tuned by interaction with a gold substrate layer, leading to exciton-plasmon coupling which strongly enhances delocalization of the excitons [33].
Due to the lack of a conclusive structural model, the underlying structure-property relationship related to these optical properties has not been resolved so far. Two different scenarios have been proposed for dispersed aggregates involving either intermolecular charge transfer or a network of coexisting aggregates [31], which asks for more experimental evidence.
In this study, we conduct ultrafast transient absorption spectroscopy on racemic and enantiopure (both (*R,R*) (left-handed prolinol side groups) and (*S,S*) (right-handed prolinol side groups)) thin films of ProSQ-C16 on glass substrates to provide a deeper insight into the excitonic properties and the structural nature of their aggregation. Via transient absorption spectroscopy we confirm a J-aggregate-like character of the main absorption line and the connection of the J- and H-like absorption lines via a shared ground state, corresponding to a single aggregate for both enantiopure thin films. It has been previously shown that a single type of aggregate requires intermolecular charge transfer to be accounted for [31].
The transient absorption dynamics reveal that inside this aggregate, an efficient non-radiative decay channel exists that converts the first excited singlet state into an optically dark intermolecular state. This transition might explain the lack of fluorescence, potentially due to a conical intersection between the initially excited and an intermediate dark state.
The racemic thin film exhibits, as expected, no excitonic CD, however, also the linear

and transient absorption properties are affected by multiple types of aggregates. Our study sheds new light on the importance of chirality for linear and transient excitonic properties in molecular aggregates and highlights the significance of charge transfer interactions for the linear, chiral and transient optical properties.

5.2 Methods

5.2.1 Samples

The squaraine dyes (*S,S*)- and (*R,R*)-ProSQ-C16 used for thin film preparation were synthesized following literature procedures [31, 32]. Thin films of ProSQ-C16 have been processed on pieces of float glass (25×25 mm^2, VWR objective slides) similar to previously published procedures [32]. Both (*S,S*)-enantiopure, (*R,R*)-enantiopure as well as racemic ((*S,S*)- 1:1 (*R,R*)-) ProSQ-C16 solutions in amylene stabilized chloroform (c = 3 mg/ml) have been used to produce thin films in ambient atmosphere by spincasting, followed by thermal annealing on a hotplate (surface temperature 180°C) for 30 min to ensure aggregation.
ProSQ-C16 layer thicknesses have been determined by spectroscopic ellipsometry (see section 5.7.1 in the Supplementary Information for details) to be as follows: (*S,S*) = 22 nm(±4 nm); (*R,R*) = 28 nm(±4 nm); (*RAC*) = 29 nm(±4 nm).
Further steady-state optical sample characterization comprising CD spectra and complex refractive indices can be found in Fig. 5.7.

5.2.2 Steady-State and Transient Absorption

Both steady-state and transient absorption spectroscopy measurements were conducted using a setup based on a 125 kHz, 15 W Yb:KGW regenerative amplifier laser system (PHAROS, Light Conversion) [34]. For transient measurements, bandpass filtered pulses from a non-collinear optical parametric amplifier (TOPAS, Light Conversion) were used for pumping the sample with a temporal width of 100-150 fs at 1.65 eV (750 nm) and 2.25 eV (550 nm). To prevent laser-induced degradation of the aggregated films, we allowed fluences of 20 to 800 W/cm^2 and loosely focus the pump beam onto the sample with a spot size of around 160 µm in diameter. For both the probe and steady-state measurements, a 1450 nm pulsed laser beam

was tightly focused into a 2 mm thick sapphire plate to generate a white light supercontinuum. The white light beam was spectrally filtered, limiting the range to 1.37-2.48 eV (500-900 nm). Spectra were detected using a silicon-based diode array mounted in a polychromatic spectrometer (HARPIA, Light Conversion and SHAMROCK, Andor). To minimize pump scattering into the detector, the polarization of the pump beam was set to be perpendicular to that of the probe, and a polarizer was placed in front of the detector to filter out most of the residual intensity of the pump beam.

5.3 Results

5.3.1 Steady-State Absorption

The annealing of the samples at high temperatures ensures J-like aggregation for both enantiopure and racemic thin films, yielding absorbance spectra dominated by J-like bands around 1.6 eV (ca. 780 nm), as seen in the normalized spectra in Fig. 5.1. For the enantiopure thin films, the well-known structure of a single asymmetric and strong J-band at 1.6 eV and a weaker H-band at 2.25 eV emerges [32, 33]. While the shapes and spectral positions of the main features are consistent throughout both enantiopure thin films, differences between the enantiopure and racemic films become evident. The racemic film absorbs with two visible sub-bands close to each other at 1.615 eV and 1.675 eV, both blue-shifted with respect to the much sharper absorption band in the enantiopure film. Furthermore, the weaker H-band almost disappears in the racemic film, as well as the weakly absorptive continuum connecting the two bands. Instead, a long absorptive tail reaching from the two J-bands to blue-shifted energies emerges. These clearly visible differences in the absorbance spectra are a first indication of the different aggregate packing structure of the racemic thin film. From the uniaxial anisotropy of both enantiopure and racemic thin films, it becomes evident that the H-like transition is basically oriented perpendicular to the plane of the thin films (extra-ordinary components of the complex refractive index). Therefore, this H-band appears only weakly in all normal incidence steady-state and transient transmission measurements discussed in this study, while the J-band seems to be polarized in-plane of the thin film.

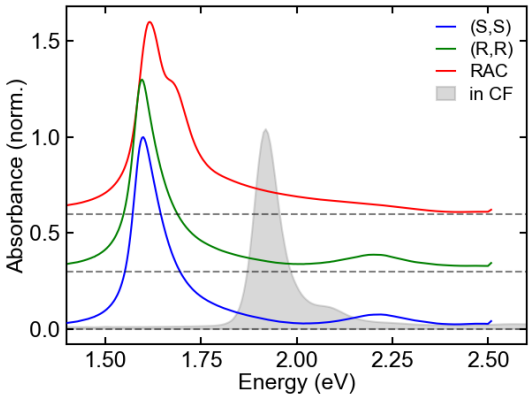

Figure 5.1: Normalized steady-state absorbance spectra of the ProSQ-C16 thin films examined in this study, as well as (*S,S*)-ProSQ-C16 in a chloroform solution as reference (grey spectrum). (S,S)/(R,R) denotes the enantiopure thin film only containing (*S,S*)- or (*R,R*)-ProSQ-C16, and RAC the racemic thin film. The inset shows the molecular structure of (*R,R*)-ProSQ-C16. The (S,S)-ProSQ-C16 has the same backbone as the (R,R) one, only with the C16 carbon chain in the opposite direction, while the racemic one contains half (R,R) and half (S,S) chromophores. The absorbance baseline has been offset by 0.3 and 0.6 for the (*R,R*) and *RAC* thin film, respectively.

5.3.2 Transient Absorption Spectra

To probe the nature of excitons within the thin film more thoroughly, transient absorption measurements are carried out, selectively exciting either the J-band or the H-band of each thin film. The spectral transient response of both thin films can be seen in Fig. 5.2(a-c) for J-band excitation and in Fig. 5.2(d-f) for H-band excitation, along with the steady-state absorbance of the corresponding thin films. In all measurements, the amplitude of the transient response is extraordinarily high, which further underlines the extremely strong light-matter interaction in ProSQ-C16 aggregates.

The transient response of the enantiopure films to excitation of the J-band (Fig. 5.2 (a,b)) is dominated by strong negative bleach signal around the J-band, coupled to blue-shifted photo-induced absorption (PIA) signals, as observed before [33]. This is in line with the well-established footprint of J-aggregates [35], where the negative bleach signal carries both ground-state bleach (GSB) and stimulated emission (SE) contributions. It is important to note that the spectral properties of each sample

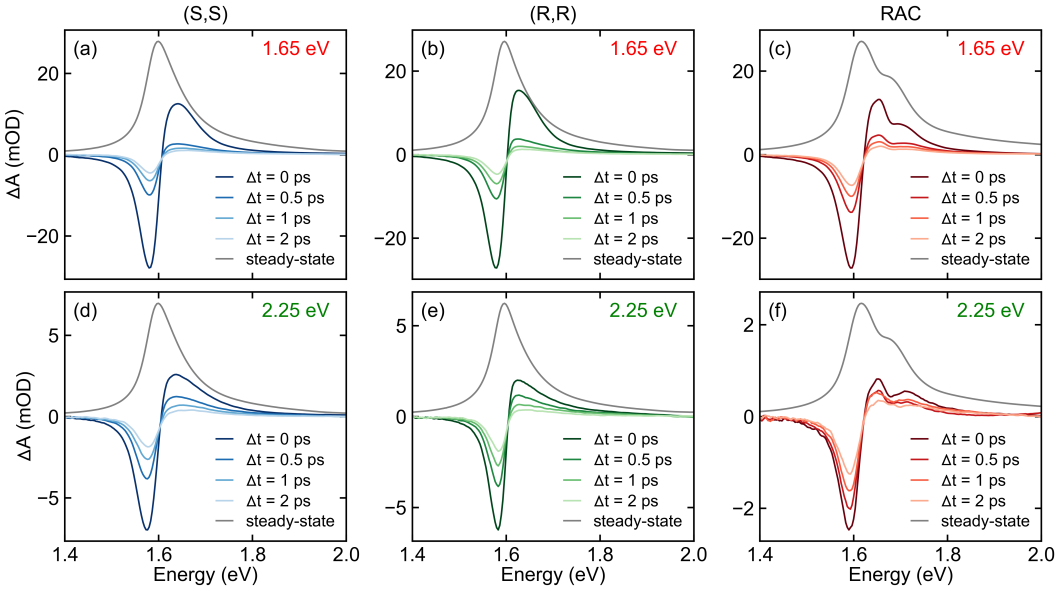

Figure 5.2: Transient absorption spectra upon photoexcitation at 1.65 eV (750 nm) (a-c) and at 2.25 eV (550 nm) (d-f) for selected delay times for a fluence of 400 W/cm^2. Blue colors show the transient absorption spectra of (*S,S*)-ProSQ-C16 thin film (a,d), green colors the (*R,R*)-ProSQ-C16 thin film (b,e), and red colors the racemic film (c,f). The grey line shows the steady-state absorbance spectrum of the given sample for reference in arbitrary units.

are not sensitive to the fluence of the photoexcitation. The amplitude of the initial transient response remains proportional to the fluence even for very high excitation densities (see Fig. 5.8, SI).

The transient absorption spectral shape of the two enantiopure thin films is remarkably alike, with the only difference being the slightly sharper low energy shoulder of the PIA signal in the (*R,R*)-ProSQ-C16 containing thin film.

Compared to the direct excitation of the J-band at 1.65 eV, photoexcitation at the H-band at 2.25 eV reveals an almost identical transient response around the J-band for both enantiopure films, with the amplitude in line with the weaker absorbance of the H-band compared to the J-band. This strong resemblance suggests that the initially excited exciton state corresponding to the H-band quickly relaxes into the excitonic state corresponding to the J-band. This strongly suggests that the two absorption lines of the enantiopure thin films originate from the same type of aggre-

gate.
The transient response of the racemic thin film on the other hand is more complicated. While both bleach and PIA signals can be identified as for the enantiopure thin films, a substructure in the PIA signal arises between 1.65 eV and 1.8 eV. At least two peaks can be seen in the PIA signal, with peak energies not in line with either of the optical bright states seen in the steady-state absorbance spectrum. A proper assignment of these peaks is difficult, as bleach signals and PIA signals from different excitonic states might overlap.
Exciting the weak H-band of the racemic thin film results in distinct changes to the transient spectra compared to direct excitation of the J-bands. The relative amplitude of the PIA features is strongly reduced when the H-band is excited, and the spectral shape of the PIA sub-peaks is also not consistent with the transient response of J-band excitation. The bleach signal on the other hand looks very consistent across both sets of measurements. This implies an efficient transfer from the H-band to the J-bands to some extent, while the exact distribution of populated excitonic states differ between the 1.65 eV and 2.25 eV photoexcitation conditions. Overall, unlike the enantiopure thin films, the transient response of the racemic thin film cannot be unambiguously assigned as J-aggregate-like.

5.3.3 Transient Absorption Dynamics

Further insights into the excitonic nature of the different aggregate structures are revealed by the dynamics of individual bleach and PIA signals and their fluence dependence, as is shown in Fig. 5.3. Overall, the dynamics in both thin films are rather fast for SQ aggregates [6, 10, 13]. Within this fast response window (< 4 ps), the bleach and PIA signals show different dynamics across all measurements.
All PIA signals decay faster than their bleach counterparts under the same measurement condition. This holds true for all samples, fluences and photoexcitation energies. In the context of two exciton absorption [35], the PIA and SE signals persist as long as the exciton band minimum (J-band) is occupied, while the ground-state bleach persists until the ground-state is occupied again. The mismatch between PIA and bleach dynamics therefore requires an intermediate state, into which exci-

tons can transition.

As expected, the dynamics of the enantiopure thin films are almost identical to each other, once more demonstrating that they share the same aggregate structure. On the contrary, the racemic thin film shows significantly slower dynamics at lower fluences, accelerating significantly with increased fluence. Even though all thin films exhibit fluence-dependent dynamics, it is much more pronounced in the racemic sample.

Further insight can be obtained by fitting of the bleach dynamics of the racemic thin film with multi-exponential decay functions (see section 5.7.4 in the Supplementary Information for all fit results). The fits suggest multiple dynamic contributions with different decay times. The root of the fluence-dependent increase seems to be the consistent increase of the relative amount of excitons undergoing the fast decay. A consistent trend is only observable for the racemic thin film, but not for the enantiopure films, which might indicate different relaxation mechanisms.

Almost elusive in the strong PIA and bleach signals and their dynamics, coherent

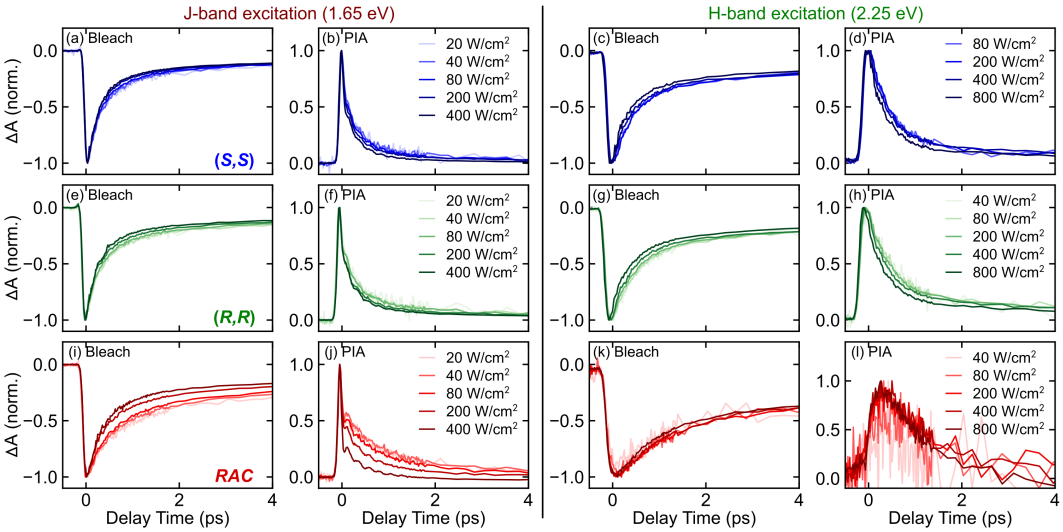

Figure 5.3: Fluence-dependent dynamics of bleach (a,c,e,g,i,k) and photoinduced absorption (b,d,f,h,j,l) signals. Data from (*S,S*) enantiopure thin films are shown in blue, (*R,R*) in green, and racemic in red. Left side spectra represent a photoexcitation at 1.65 eV (750 nm), right side 2.25 eV (550 nm) photoexcitation.

oscillations can be found at the spectral border between the PIA and bleach signals.

These coherent oscillations are visible for all thin films, but only if the J-band is directly excited at 1.65 eV. After careful subtraction of the exponentially decaying population signal, the clearly visible coherent oscillations are presented in Fig. 5.4(a-c), for all three samples. The Fourier-transform of the residuals (Fig. 5.4(d-f)) shows that the oscillations happen at a frequency of 4.3 THz or ca. 144 cm^{-1}, again consistent for all films—suggesting a molecular origin. Similar coherent oscillations at 147 cm^{-1} have been found in monomeric ProSQ-C16 in solution, and were identified as a collective molecular backbone vibration [36].

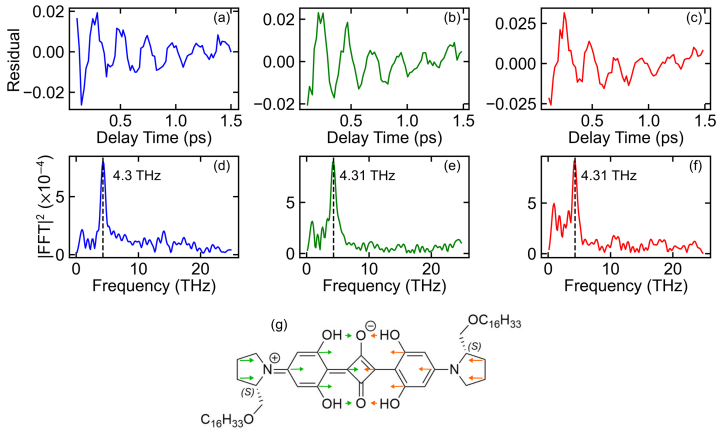

Figure 5.4: Dynamics (a-c) and Fourier-transform frequency spectra (d-f) of the coherent oscillations of the photoinduced absorption signals. The dynamics were obtained at the photon energy showing the largest amount of oscillations. (g) Arrows on the molecular structure of (*S,S*)-ProSQ-C16 indicate the previously reported collective molecular vibration at similar frequencies [36].

5.3.4 Singular Value Decomposition

In order to disentangle the correlated spectral and dynamical properties, singular value decomposition is performed for a series of high fluence measurements. The results for the (*S,S*)-ProSQ-C16 thin film is shown in Fig. 5.5, the corresponding results for the other two samples can be found in Fig. 5.9 in the Supplementary Information.

For datasets obtained by J-band excitation, the first two singular values had a large impact on the transient absorption data. For datasets obtained from H-band excita-

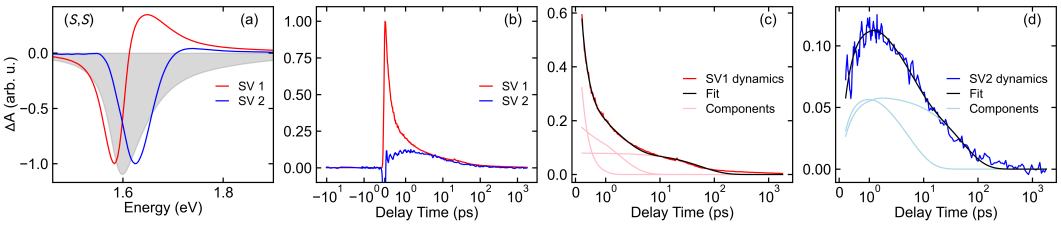

Figure 5.5: Spectra and dynamics of the two relevant singular values obtained from the transient absorption data of the (*S,S*)-ProSQ-C16 thin film excited at 1.65 eV with a fluence of 400 W/cm^2. (a) Spectra of the first two singular values (SV), both demonstrating shifts of the negative features with respect to the inverted absorption maximum. (b) Time traces associated with the singular values. (c) Fit of the dynamics of the first singular value dynamics using three exponential decay functions, each shown. (d) Fit of the second singular value dynamics, with a function containing two initially rising and decaying parts.

tion, the singular value decomposition did not yield constructive results, and therefore will not be discussed. For the enantiopure films, the spectral shape is consistent (Fig. 5.5(a), 5.9(a)): the first singular value looks largely like the J-aggregate-like transient absorption spectra after relatively short delay times, showing both bleach and photoinduced absorption signals; the second singular value's spectral response is dominated by a bleach signal of similar spectral shape to the absorption maximum, but blue-shifted, next to a miniscule photoinduced absorption signal.

Similar to the spectral components, singular value dynamics differ quite strongly from another (Fig. 5.5(b), 5.9(b)). While the first singular value dynamics are of purely decaying nature, a distinct growth can be seen for the second singular value. Additionally, the first singular value dynamics show a smooth decay, while the second dynamics clearly contain oscillations, reminding us of the coherent oscillations that were observed in the dynamics of certain regions of the TA spectra. The spectral position of the coherent oscillations and the second singular value overlap significantly. Note that the strong negative feature of the second singular value dynamics is a decomposition artifact.

To quantify the dynamics of the singular values and their relationship to each other, we fitted the dynamics considering two different fit functions. For the first singular value, at least three exponential decays were needed to fit the dynamics

$$f_1(t) = A_1 \cdot e^{\frac{-t}{\tau_1}} + A_2 \cdot e^{\frac{-t}{\tau_2}} + A_3 \cdot e^{\frac{-t}{\tau_3}}, \tag{5.1}$$

while for the second, the growing and decaying dynamics required a fit function with at least one growing component and two considered exponential decay functions

$$f_2(t) = A_1 \cdot \left(1 - e^{\frac{-t}{\tau_1}}\right)\left((1 - A_2) \cdot e^{\frac{-t}{\tau_2}} + A_2 \cdot e^{\frac{-t}{\tau_3}}\right). \tag{5.2}$$

The fit results are summarized in the table below and can be seen in (Fig. 5.5(c,d), 5.9(c,d)).

Table 5.1: Fit results of the dynamics of the relevant singular values of the transient absorption spectrum of the (*S,S*)-ProSQ-C16 thin film excited at 1.65 eV with a fluence of 6.5 W/cm^2. Δ denotes the confidence interval of the fit parameter above.

Data	$\mathbf{A_1}$	$\mathbf{t_1}$ **(ps)**	$\mathbf{A_2}$	$\mathbf{t_2}$ **(ps)**	$\mathbf{A_3}$	$\mathbf{t_3}$ **(ps)**
SV1	0.342	0.242	0.176	1.75	0.0796	57.1
Δ	0.007	0.009	0.007	0.12	0.0024	3.5
SV2	0.133	0.364	0.524	0.452	-	50.2
Δ	0.004	0.021	0.095	0.046	-	7.2

The multiple exponential decays of the SV1 dynamics indicate multiple relaxation mechanisms of the initially excited states over a variety of time scales. While the shortest component ($\approx$ 0.24 ps) has the dominant contribution, a considerable amount of the excited states relaxes more slowly ($\approx$ 1.75 ps), while an even smaller margin decays only after $\approx$ 57 ps. Similar to the SV1 dynamics, the decay of the SV2 dynamics after the signal rose over roughly 0.36 ps require two components, with a fast ($\approx$ 0.5 ps) and slow ($\approx$ 50 ps) decay of equal amplitude.
The time scales of both the fastest and slowest components of each SV dynamics are closely related to each other. The fast growth of SV2 coincides with the decay of SV1, suggesting a fast transition from a state represented by the first singular value to another associated with the second singular value. The long-time component indicates that both underlying excitonic states also possess a slowly decaying sub-population.
For the racemic thin film (see Fig. 5.9(e-h)), the spectrum of SV1 resembles the initial transient absorption spectra, similar to the enantiopure thin films. On the other hand, the spectrum of SV2 deviates from a simple bleach profile, as the width of the negative feature is significantly narrower than the absorption line. Moreover, the

side peak of the SV2 spectrum is neither in relative position nor relative amplitude consistent to the steady-state absorption spectrum.
Adding to the spectral discrepancies, the SV2 dynamics cannot be fitted using the fit functions applied to the enantiopure SV2 dynamics. This implies that these functions describing the dynamics of the enantiopure film must be enhanced with more complex contributions to accurately represent the racemic thin film's behavior.

5.4 Discussion

From the transient absorption spectra, the J-like character of the enantiopure thin films becomes more evident. The presence of SE and PIA features next to the ground state bleach and their spectral shape are clear indications that the bright state observed as the J-band is indeed at the minimum of the exciton band, which is the fundamental requirement for a J-aggregate. Additionally, the induction of a J-like transient signal after photoexcitation of the H-band represents compelling evidence for the J-band being the lowest exciton-band state.
Our data strongly support a "one aggregate" picture for enantiopure thin films, in which only one single aggregate is responsible for the light-matter interactions at visible-light frequencies. This is in line with the suggestions by Painelli and coworkers [31] that a single aggregate can lead to two absorptive peaks due to intermolecular charge transfer hybridization of excitons in ProSQ aggregates in solution.
Some of the observations made above partially hold for the racemic thin film as well, even though the steady-state and transient spectra appear to be more convoluted. The transient response at the J-band deviates from a perfect J-aggregate-like response, especially for the PIA signal. Furthermore, the spectral shape and amplitude of the PIA signal are dependent on whether the J-band or the H-band is excited. This is a strong indication that, unlike the enantiopure thin films, multiple exciton bands must be responsible for the transient properties of the racemic thin film, and therefore multiple types of aggregates.
Understanding the dynamics of all spectral features needs the consideration of multiple relaxation channels, which is consistent with the dynamics obtained from SVD. We associate the first singular value signal with the occupation of the exciton band minimum (XM), and the second singular value signal with occupation of an interme-

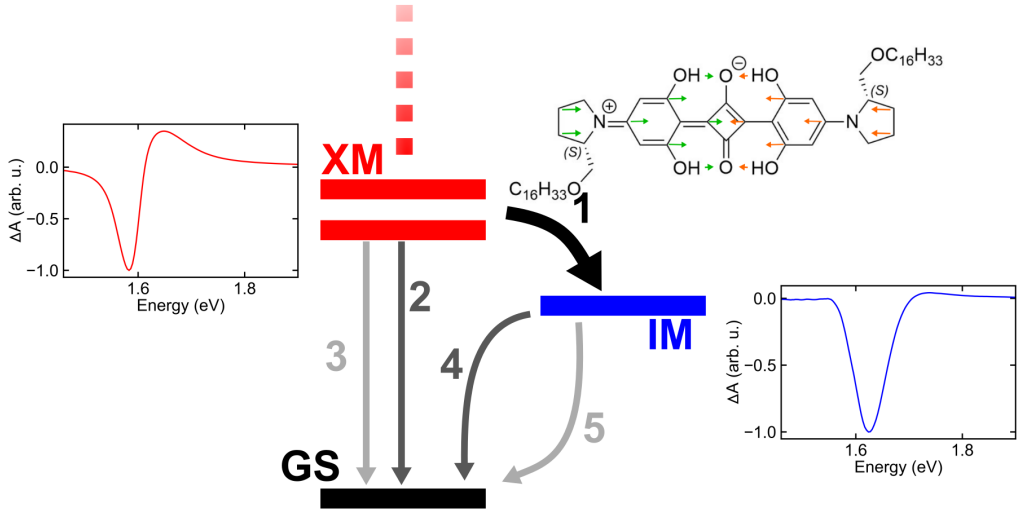

Figure 5.6: Sketch of the exciton relaxation channels of ProSQ-C16 aggregates. The fastest exciton dynamics are observed for a transition from the initially excited state at the low energy edge of the exciton band (XM) into the intermediate state (IM) (**1**), which might be mediated by low energy vibronic coupling. This migration happens extremely fast, while the transition to the ground state (GS) takes significantly longer (**4**,**5**). On longer time scales, exciton cans also directly convert back into the ground state (**2**,**3**).

diate dark state (IM) (see Fig. 5.6). The coinciding decay of the XM-related signal and growth of the IM-related signal strongly suggests an excitonic transition from the XM to the IM state, in line with the mismatch of the bleach and PIA dynamics. However, the XM→IM transition (**1**) cannot rationalize all facets of the dynamics, and multiple slower relaxation dynamics from both XM (**2**,**3**) and IM (**4**,**5**) have to be considered. The low fluorescence yield of the thin films suggests that the slower relaxation channels are mostly non-radiative. These dynamics might arise from recombination at traps or interfaces, or exciton-exciton annihilation processes [37–42]. The nature of the reported intermediate state cannot be resolved by our study, but given the theoretical work done by Painelli and coworkers [31], an intermolecular charge transfer state, which is optically dark on its own [11, 12], represents a suitable candidate.

The short lifetime of the excitons and their transition into a dark state before relaxing back to the ground state deserves special attention due to the fast transition time.

As this transition happens on the sub-ps scale, it can be mediated by a conical intersection [43], outcompeting the radiative transition back to the ground state. While dynamics mediated by conical intersections have been demonstrated and hinted at for various molecular aggregates, including squaraines [18, 44, 45], it is usually discussed as a direct relaxation channel between excited and ground state, and the wave packet motion towards the conical intersection is mediated by high-energy, diatomic vibrations. For the systems at hand, the vibronic mode involved might be the collective molecular vibration observed in this study. Note, that the timescale of the potential conical intersection transition in such a system is slower than in systems which have access to higher energy vibrational modes [18, 44, 45]. To confirm this hypothesis, more theoretical and experimental evidence is needed, which is beyond the scope of this study.

5.5 Conclusions

In conclusion, our study employed steady-state and ultrafast transient absorption spectroscopy to investigate aggregation, as well as the nature and dynamics of excitons in enantiopure and racemic ProSQ-C16 thin films. We observed transient spectra originating from a single type of aggregate in both enantiopure thin films. Our data suggests that the optical response of these thin films is based on a dominant charge-transfer-hybridized aggregate, which features both a strong J-like and a weaker H-like band. On the other hand, the steady-state and transient optical properties of the racemic thin film deviate significantly from a typical J-aggregate-like response.

We report a multitude of dynamical contributions, led by an efficient transition of the photoexcited exciton band inside the J-aggregate of the enantiopure thin film into an optically dark intermediate state, which explains the poor fluorescence observed for these systems. We hypothesize that this intermediate state is of intermolecular charge transfer nature. Based on the time scales and coherent oscillations observed in the transient response of all systems, we suggest that a conical intersection towards the intermediate CT state could provide an efficient non-radiative relaxation channel.

Our findings suggest that non-Frenkel exciton states play a significant role for the optical properties in strongly aggregated systems of chiral ProSQ-C16 molecules and have to be accounted for in order to understand the remarkable chiroptical properties of this extraordinary system. We further highlight the added value of chirality for not only the chiral, but also the linear and transient optical properties. This provides deeper insight and guidance towards finding materials with tailored optoelectronic properties.

5.6 Contributions

Robin Bernhardt and Manuela Schiek conceived the project. Robin Bernhardt, Lukas Rieland and Tianyi Wang performed the steady-state and transient optical experiments and analyzed the experimental results. Marvin Schumacher and Arne Lützen synthesized the squaraine molecules. Manuela Schiek prepared and characterized the thin film samples and performed and analyzed the ellipsometry experiments. Paul van Loosdrecht supervised the project.

References

(1) Saikin, S. K.; Eisfeld, A.; Valleau, S.; Aspuru-Guzik, A. *Nanophotonics* **2013**, *2*, 21–38.

(2) Valencia, A. M.; Bischof, D.; Anhäuser, S.; Zeplichal, M.; Terfort, A.; Witte, G.; Cocchi, C. *Electronic Structure* **2023**, *5*, 033003.

(3) Kasha, M.; Rawls, H. R.; Ashraf El-Bayoumi, M. *Pure and Applied Chemistry* **1965**, *11*, 371–392.

(4) Davydov, A. S. *Soviet Physics Uspekhi* **1964**, *7*, 145.

(5) Hestand, N. J.; Spano, F. C. *Chemical Reviews* **2018**, *118*, 7069–7163.

(6) De Miguel, G.; Ziółek, M.; Zitnan, M.; Organero, J. A.; Pandey, S. S.; Hayase, S.; Douhal, A. *The Journal of Physical Chemistry C* **2012**, *116*, 9379–9389.

(7) Lambert, C.; Koch, F.; Völker, S. F.; Schmiedel, A.; Holzapfel, M.; Humeniuk, A.; Röhr, M. I. S.; Mitric, R.; Brixner, T. *Journal of the American Chemical Society* **2015**, *137*, 7851–7861.

(8) Paternò, G. M.; Moretti, L.; Barker, A. J.; D'Andrea, C.; Luzio, A.; Barbero, N.; Galliano, S.; Barolo, C.; Lanzani, G.; Scotognella, F. *Journal of Materials Chemistry C* **2017**, *5*, 7732–7738.

(9) Balzer, F.; Hestand, N. J.; Zablocki, J.; Schnakenburg, G.; Lützen, A.; Schiek, M. *The Journal of Physical Chemistry C* **2022**, *126*, 13802–13813.

(10) Bernhardt, R.; Manrho, M.; Zablocki, J.; Rieland, L.; Lützen, A.; Schiek, M.; Meerholz, K.; Zhu, J.; Jansen, T. L. C.; Knoester, J.; van Loosdrecht, P. H. M. *Journal of the American Chemical Society* **2022**, *144*, 19372–19381.

(11) Hestand, N. J.; Zheng, C.; Penmetcha, A. R.; Cona, B.; Cody, J. A.; Spano, F. C.; Collison, C. J. *The Journal of Physical Chemistry C* **2015**, *119*, 18964–18974.

(12) Shen, C.-A.; Bialas, D.; Hecht, M.; Stepanenko, V.; Sugiyasu, K.; Würthner, F. *Angewandte Chemie* **2021**, *133*, 12056–12065.

(13) Chen, H.; Farahat, M. S.; Law, K.-Y.; Whitten, D. G. *Journal of the American Chemical Society* **1996**, *118*, 2584–2594.

(14) Rösch, A. T.; Zhu, Q.; Robben, J.; Tassinari, F.; Meskers, S. C. J.; Naaman, R.; Palmans, A. R. A.; Meijer, E. W. *Chemistry – A European Journal* **2021**, *27*, 298–306.

(15) Selby, J.; Holzapfel, M.; Lombe, B. K.; Schmidt, D.; Krause, A.-M.; Würthner, F.; Bringmann, G.; Lambert, C. *The Journal of Organic Chemistry* **2020**, *85*, 12227–12242.

(16) Mass, O. A.; Wilson, C. K.; Roy, S. K.; Barclay, M. S.; Patten, L. K.; Terpetschnig, E. A.; Lee, J.; Pensack, R. D.; Yurke, B.; Knowlton, W. B. *The Journal of Physical Chemistry B* **2020**, *124*, 9636–9647.

(17) Zablocki, J.; Arteaga, O.; Balzer, F.; Hertel, D.; Holstein, J. J.; Clever, G.; Anhäuser, J.; Puttreddy, R.; Rissanen, K.; Meerholz, K.; Lützen, A.; Schiek, M. *Chirality* **2020**, *32*, 619–631.

(18) Freytag, E.; Kreimendahl, L.; Holzapfel, M.; Petersen, J.; Lackinger, H.; Stolte, M.; Würthner, F.; Mitric, R.; Lambert, C. *The Journal of Organic Chemistry* **2023**, *88*, 10777–10788.

(19) Brandt, J. R.; Salerno, F.; Fuchter, M. J. *Nature Reviews Chemistry* **2017**, *1*, 1–12.

(20) Naaman, R.; Waldeck, D. H. *The Journal of Physical Chemistry Letters* **2012**, *3*, 2178–2187.

(21) Shahana Nizar, N. S.; Sujith, M.; Swathi, K.; Sissa, C.; Painelli, A.; George Thomas, K. *Chemical Society Reviews* **2021**, *50*, 11208–11226.

(22) Bertocchi, F.; Sissa, C.; Painelli, A. *Chirality* **2023**, *35*, 681–691.

(23) Mitov, M. *Advanced Materials* **2012**, *24*, 6260–6276.

(24) Gompf, B.; Braun, J.; Weiss, T.; Giessen, H.; Dressel, M.; Hübner, U. *Physical Review Letters* **2011**, *106*, 185501.

(25) Wang, Z.; Cheng, F.; Winsor, T.; Liu, Y. *Nanotechnology* **2016**, *27*, 412001.

(26) Yang, Y.; da Costa, R. C.; Fuchter, M. J.; Campbell, A. J. *Nature Photonics* **2013**, *7*, 634–638.

(27) Schulz, M.; Balzer, F.; Scheunemann, D.; Arteaga, O.; Lützen, A.; Meskers, S. C. J.; Schiek, M. *Advanced Functional Materials* **2019**, *29*, 1900684.

(28) Albano, G.; Pescitelli, G.; Di Bari, L. *Chemical Reviews* **2020**, *120*, 10145–10243.

(29) Wade, J.; Hilfiker, J. N.; Brandt, J. R.; Liirò-Peluso, L.; Wan, L.; Shi, X.; Salerno, F.; Ryan, S. T. J.; Schöche, S.; Arteaga, O.; Jávorfi, T.; Siligardi, G.; Wang, C.; Amabilino, D. B.; Beton, P. H.; Campbell, A. J.; Fuchter, M. J. *Nature Communications* **2020**, *11*, 6137.

(30) Deng, Y.; Wang, M.; Zhuang, Y.; Liu, S.; Huang, W.; Zhao, Q. *Light: Science & Applications* **2021**, *10*, 76.

(31) Giavazzi, D.; F. Schumacher, M.; Grisanti, L.; Anzola, M.; Maiolo, F. D.; Zablocki, J.; Lützen, A.; Schiek, M.; Painelli, A. *Journal of Materials Chemistry C* **2023**, *11*, 8307–8321.

(32) Schulz, M.; Zablocki, J.; Abdullaeva, O. S.; Brück, S.; Balzer, F.; Lützen, A.; Arteaga, O.; Schiek, M. *Nature Communications* **2018**, *9*, 2413.

(33) Quenzel, T.; Timmer, D.; Gittinger, M.; Zablocki, J.; Zheng, F.; Schiek, M.; Lützen, A.; Frauenheim, T.; Tretiak, S.; Silies, M.; Zhong, J.-H.; De Sio, A.; Lienau, C. *ACS Nano* **2022**, *16*, 4693–4704.

(34) Jung, E.; Budzinauskas, K.; Öz, S.; Ünlü, F.; Kuhn, H.; Wagner, J.; Grabowski, D.; Klingebiel, B.; Cherasse, M.; Dong, J.; Aversa, P.; Vivo, P.; Kirchartz, T.; Miyasaka, T.; van Loosdrecht, P. H. M.; Perfetti, L.; Mathur, S. *ACS Energy Letters* **2020**, *5*, 785–792.

(35) Bakalis, L. D.; Knoester, J. *The Journal of Physical Chemistry B* **1999**, *103*, 6620–6628.

(36) Timmer, D.; Zheng, F.; Gittinger, M.; Quenzel, T.; Lünemann, D. C.; Winte, K.; Zhang, Y.; Madjet, M. E.; Zablocki, J.; Lützen, A.; Zhong, J.-H.; De Sio, A.; Frauenheim, T.; Tretiak, S.; Lienau, C. *Journal of the American Chemical Society* **2022**, *144*, 19150–19162.

(37) Malý, P.; Lüttig, J.; Rose, P. A.; Turkin, A.; Lambert, C.; Krich, J. J.; Brixner, T. *Nature* **2023**, *616*, 280–287.

(38) Fazzi, D.; Barbatti, M.; Thiel, W. *Journal of the American Chemical Society* **2016**, *138*, 4502–4511.

(39) Binder, R.; Polkehn, M.; Ma, T.; Burghardt, I. *Chemical Physics* **2017**, *482*, 16–26.

(40) Schubert, A.; Settels, V.; Liu, W.; Würthner, F.; Meier, C.; Fink, R. F.; Schindlbeck, S.; Lochbrunner, S.; Engels, B.; Engel, V. *The Journal of Physical Chemistry Letters* **2013**, *4*, 792–796.

(41) Manna, B.; Ghosh, R.; Palit, D. K. *The Journal of Physical Chemistry C* **2015**, *119*, 10641–10652.

(42) Fan, X.; Wei, A.; Klamroth, T.; Zhang, Y.; Gao, K.; Wang, L. *Physical Review B* **2023**, *107*, 134301.

(43) De Sio, A.; Sommer, E.; Nguyen, X. T.; Groß, L.; Popović, D.; Nebgen, B. T.; Fernandez-Alberti, S.; Pittalis, S.; Rozzi, C. A.; Molinari, E.; Mena-Osteritz, E.; Bäuerle, P.; Frauenheim, T.; Tretiak, S.; Lienau, C. *Nature Nanotechnology* **2021**, *16*, 63–68.

(44) Paterson, M. J.; Blancafort, L.; Wilsey, S.; Robb, M. A. *The Journal of Physical Chemistry A* **2002**, *106*, 11431–11439.

(45) Miguel, G. d.; Marchena, M.; Zitnan, M.; Pandey, S. S.; Hayase, S.; Douhal, A. *Physical Chemistry Chemical Physics* **2012**, *14*, 1796–1805.

5.7 Supplementary Information

5.7.1 Complex Refractive Index and Circular Dichroism Spectra

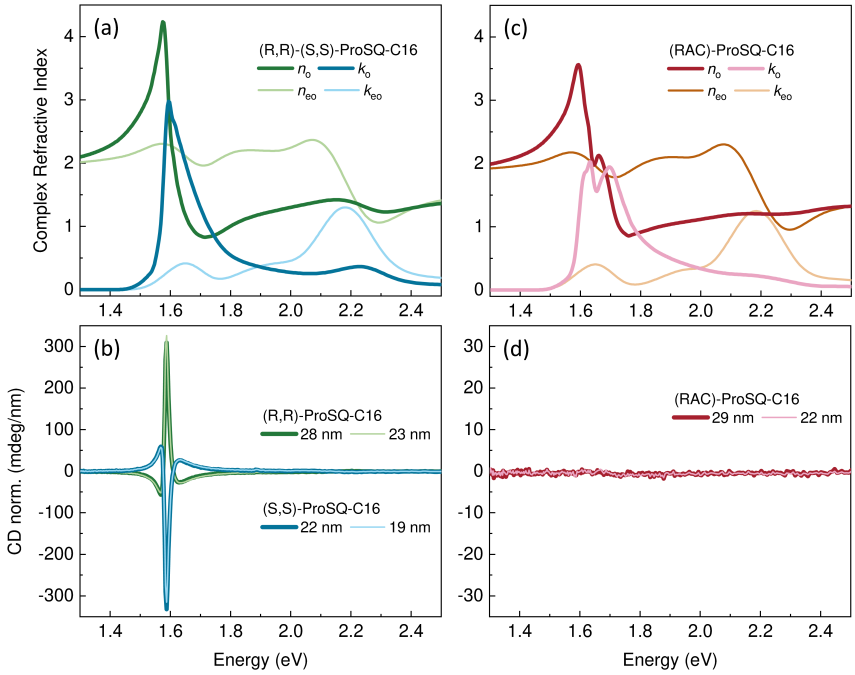

Figure 5.7: Steady-state optical characterization using a single rotating compensator J.A. Woollam M2000-DI ellipsometer with CCD-based detection. Upper row: Effective uniaxial complex refractive indices obtained via a combined multi-sample analysis of Ψ and Δ VASE scans in reflection and normal incidence transmission intensity scans of (a) enantiopure ProSQ-C16 and (c) racemic ProSQ-C16 spincasted and annealed thin films. The ordinary (in-plane) real and imaginary part, n_o and k_o, and the extra-ordinary (out-of-plane) real and imaginary part, n_{eo} and k_{eo}, are plotted. Lower row: Thickness normalized CD spectra extracted from the matrix logarithm of reconstructed normal incidence transmission Mueller matrix measurements of (b) (R,R)- and (S,S)-ProSQ-C16 as well as (d) (RAC)-ProSQ-C16 spincasted and annealed thin films. Layer thicknesses used for the normalization are obtained from standard ellipsometric analysis and are indicated in the legend.

Steady-state optical characterization has been performed using a single rotating compensator J.A. Woollam M2000-DI ellipsometer with CCD-based detection including the software CompleteEASE for data acquisition (version 5) and evaluation (version 6). The uniaxial anisotropic complex refractive indices have been obtained via a

multi-sample analysis combining variable angle spectroscopic ellipsometry (VASE) scans recording Ψ and Δ for angles of incidence from 45° to 75° in steps of 5° as well as normal incidence transmission intensity scans in the spectroscopic range from 192 nm to 1688 nm following a previously described procedure [1]. Note that the float-glass substrate is opaque for wavelength below 350 nm.

The enantiopure thin films, (*R,R*)- and (*S,S*)-ProSQ-C16, are expected to have the same linear optical properties, and therefore, are evaluated jointly to give an effective complex refractive index, as is shown in Figure 5.7(a). Three measurements per sample (2x ellipsometry with 90° azimuthal sample rotation, 1x transmission intensity) from two sets of samples, i.e. two samples with different layer thicknesses for each handedness (N=12) have been fitted simultaneously.

For the racemic thin film (*RAC*)-ProSQ-C16 two samples with different layer thicknesses have been evaluated jointly (N=6) to result the complex refractive index plotted in Figure 5.7(c). Both the enantiopure and the racemic thin film have their maximum extinction (J-like band) oriented within the plane of the film (ordinary components) in the deep-red spectral range, while their second spectral signature (H-like band) within the green is weaker and broader mainly oriented out of the film plane (extra-ordinary components). The maximum extinction of the racemic thin film is split into two sub-bands and the values are certainly lower compared to the enantiopure films: (RAC)-$n_o \approx 3.6$ (2.1) at 778 nm (745 nm) and versus enantiopure-$n_o \approx 4.3$ at 786 nm; (RAC)-$k_o \approx 2.0$ (1.95) at 760 nm (730 nm) versus enantiopure-$k_o \approx 3.0$ at 778 nm.

The circular dichroism (CD) have been obtained from a partial Mueller matrix measurement (first three rows of the Mueller matrix) at normal incidence transmission similar to the previously described procedure [2]. However, this time the full Mueller matrix is reconstructed by an algebraic procedure before calculating the differential Mueller matrix [3]. The CD spectra shown in Figure 5.7(b,d) are thickness normalized given in millidegree per nanometer (mdeg/nm) as the average of the l_{14} and l_{41} divided by the respective layer thickness obtained from the ellipsometric analysis. Note that CD does not equal the ellipticity θ, which is the typical output of a conventional "CD"-spectrometer, but equals CD $= 2 \cdot \theta$ instead, in case of low-value approximation for ellipticity. As expected, the racemic thin film is CD-silent, as shown in Figure 5.7(d), while the enantiopure thin films exhibit a strong CD signal

of opposite sign peaking at 780 nm. Since the CD signal scales linearly with layer thickness, it is of intrinsic excitonic nature, and not overlaid with structural effects. Note that its maximum value around ± 330 mdeg/nm is clearly lower than the record value approaching ± 1000 mdeg/nm reported earlier [2]. This is mainly due to the certainly lower spectral resolution of the CCD-based detection of the M2000 instrument (5 nm bandwidth) used in this study compared to the monochromator-based VASE instrument with adjustable slit-width (less than 2 nm bandwidth) used previously [2]. Furthermore, processing in ambient conditions (instead of inert glove-box conditions previously) can affect the film quality.

5.7.2 Fluence Dependence of Transient Signal Strengths

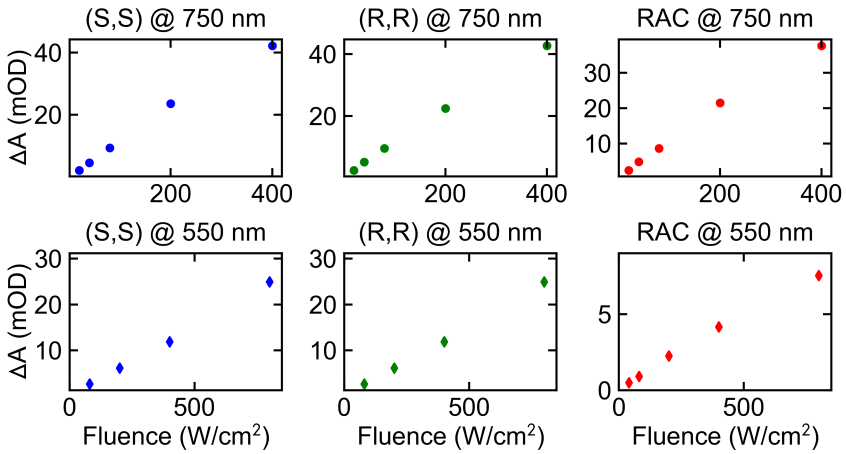

Figure 5.8: Amplitude of the bleach signal as a function of pump pulse fluence for all shown measurements.

5.7.3 Singular Value Decomposition of (*R*,*R*)- and Racemic ProSQ-C16 Thin Films and Fit Results

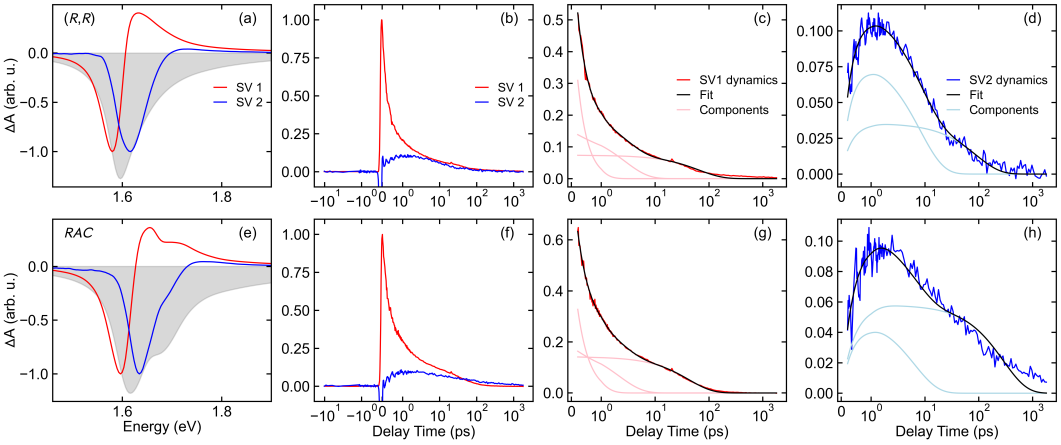

Figure 5.9: Spectra and dynamics of the two relevant singular values obtained from the transient absorption data of the (*R*,*R*)-ProSQ-C16 thin film (a-d) and the racemic thin film (e-h), in accordance to the procedure shown in Fig. 5.5. Note that the fitting function has been the same for all three samples, and that the racemic singular value dynamics yield a less satisfying fit to the model.

Table 5.2: Fit results of SV1

Data	A_1	t_1 (ps)	A_2	t_2 (ps)	A_3	t_3 (ps)
(*S*,*S*)	0.342	0.242	0.176	1.75	0.0796	57.1
Δ	0.007	0.009	0.007	0.12	0.0024	3.5
(*R*,*R*)	0.323	0.338	0.139	2.72	0.0735	65.1
Δ	0.006	0.011	0.006	0.23	0.0029	4.8
RAC	0.339	0.399	0.165	2.13	0.141	42.4
Δ	0.013	0.018	0.012	0.23	0.004	1.9

Table 5.3: Fit results of SV2

Data	A_1	t_1 (ps)	A_2	t_2 (ps)	t_3 (ps)
(*S*,*S*)	0.133	0.364	0.524	0.452	50.2
Δ	0.004	0.021	0.095	0.046	7.2
(*R*,*R*)	0.118	0.344	0.817	0.3	90.7
Δ	0.002	0.015	0.087	0.037	16.6
RAC	0.11	0.432	0.64	0.53	286
Δ	0.004	0.032	0.122	0.024	30

5.7.4 Fit Results

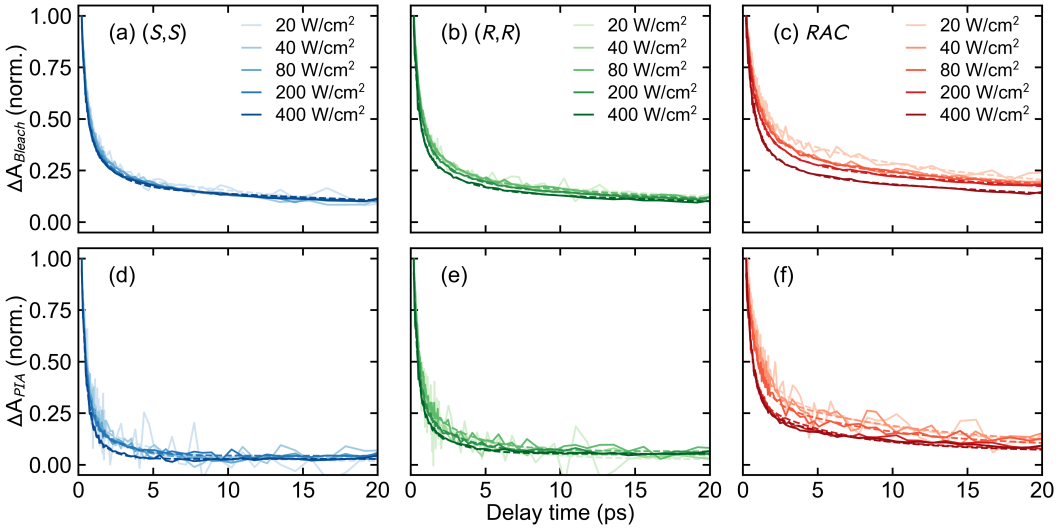

Figure 5.10: Fits (dashed) of the bleach (top) and PIA (bottom) signals for all samples after photoexcitation at 1.65 eV.

Fitting of the bleach dynamics reveals the origin of the fluence dependence. Since dynamics obtained from H-band excitations are distorted by the initial transition into the J-band, only data from J-band excitation is considered. Tables with the fit results are presented below. PIA fits are also added, even though they do not show any consistent patterns. Best fits were obtained by least-squares minimization using a trust region reflective algorithm.

Bleach Dynamics

The bleach dynamics were fitted using the following formula

$$f_1 = A_1 \cdot e^{\frac{-t}{\tau_1}} + A_2 \cdot e^{\frac{-t}{\tau_2}} + A_3 \cdot e^{\frac{-t}{\tau_3}}. \tag{5.3}$$

This formula accounts for three contributions to the dynamics of different decay times. As seen in the tables below, the fluence dependent acceleration of dynamics is not rooted in an increase of the kinetic rates ($1/\tau_i$), but in an increase of the exciton population undergoing the fast relaxation (A_1), at the expense of the slower

transitions (A_2, A_3).

Table 5.4: Bleach dynamics fit results of (*S*,*S*)-ProSQ-C16.

Fit parameter	**20 W/cm^2**	**Δ**	**40 W/cm^2**	**Δ**	**80 W/cm^2**	**Δ**
A_1	0.672	0.00783	0.935	0.000611	0.961	0.00024
t_1 (ps)	0.236	0.00461	0.368	0.000392	0.348	0.000132
A_2	0.546	0.0113	0.34	0.000604	0.33	0.000215
t_2 (ps)	1.05	0.0349	2.24	0.0781	2.18	0.0283
A_3	0.244	0.000239	0.166	0.000124	0.171	4.38e-05
t_3 (ps)	21.7	5.76	37.8	22.1	38.2	7.78
Fit parameter	**200 W/cm^2**	**Δ**	**400 W/cm^2**	**Δ**		
A_1	1.01	0.000361	1.17	0.000643		
t_1 (ps)	0.311	0.00014	0.256	0.000104		
A_2	0.32	0.000295	0.363	0.000367		
t_2 (ps)	1.92	0.0259	1.56	0.0121		
A_3	0.173	3.83e-05	0.177	2.63e-05		
t_3 (ps)	39.7	8.47	39.3	6.4		

Table 5.5: Bleach dynamics fit results of (*R*,*R*)-ProSQ-C16.

Fit parameter	**20 W/cm^2**	**Δ**	**40 W/cm^2**	**Δ**	**80 W/cm^2**	**Δ**
A_1	0.941	0.00232	0.857	0.000689	0.899	0.000308
t_1 (ps)	0.341	0.00129	0.379	0.000508	0.348	0.00019
A_2	0.323	0.00245	0.326	0.000782	0.347	0.000355
t_2 (ps)	1.99	0.221	2.1	0.0827	1.95	0.0248
A_3	0.213	0.00032	0.204	0.00013	0.21	4.26e-05
t_3 (ps)	37.5	37.0	31.1	8.06	33.9	3.61
Fit parameter	**200 W/cm^2**	**Δ**	**400 W/cm^2**	**Δ**		
A_1	0.93	0.000256	1.03	0.000471		
t_1 (ps)	0.36	0.00016	0.308	0.000169		
A_2	0.306	0.000261	0.283	0.00033		
t_2 (ps)	2.16	0.0347	2.08	0.0563		
A_3	0.182	4.23e-05	0.161	6.7e-05		
t_3 (ps)	40.9	8.46	42.7	21.2		

Table 5.6: Bleach dynamics fit results of *RAC*-ProSQ-C16.

Fit parameter	20 W/cm^2	Δ	40 W/cm^2	Δ	80 W/cm^2	Δ
A_1	0.642	0.00212	0.478	0.00235	0.624	0.00075
t_1 (ps)	0.791	0.00699	0.474	0.00315	0.528	0.000965
A_2	0.345	0.00347	0.389	0.00281	0.307	0.000865
t_2 (ps)	37.6	61.6	1.85	0.0624	2.32	0.0732
A_3	0.158	0.00194	0.321	7.42e-05	0.304	5.76e-05
t_3(ps)	5.0	12.5	38.1	3.97	40.5	3.62
Fit parameter	**200 W/cm^2**	**Δ**	**400 W/cm^2**	**Δ**		
A_1	0.656	0.000857	0.799	0.00108		
t_1 (ps)	0.377	0.000795	0.387	0.000664		
A_2	0.393	0.00126	0.294	0.00144		
t_2 (ps)	1.69	0.0271	1.8	0.0773		
A_3	0.29	4.19e-05	0.239	7.27e-05		
t_3(ps)	38.9	3.24	37.5	6.99		

PIA Dynamics

The PIA dynamics were fitted using the following formula

$$f_1 = A_1 \cdot e^{\frac{-t}{\tau_1}} + A_2 \cdot e^{\frac{-t}{\tau_2}} + A_3. \tag{5.4}$$

Note that just like the bleach signal, the dynamics of the PIA signals do not portray a single exponential decay but need at least two components to be fitted.

Table 5.7: PIA dynamics fit results of (*S*,*S*)-ProSQ-C16.

Fit parameter	20 W/cm^2	Δ	40 W/cm^2	Δ	80 W/cm^2	Δ
A_1	1.44	0.0177	1.2	0.00493	1.32	0.00149
t_1 (ps)	0.335	0.002	0.328	0.00151	0.317	0.000308
A_2	0.222	0.00244	0.341	0.00518	0.288	0.00103
t_2 (ps)	4.09	3.78	1.91	0.191	2.09	0.0803
A_3	0.0171	0.000339	0.0346	4.83e-05	0.0278	1.54e-05
Fit parameter	**200 W/cm^2**	**Δ**	**400 W/cm^2**	**Δ**		
A_1	1.4	0.000933	1.55	0.00185		
t_1 (ps)	0.285	0.000132	0.26	0.000253		
A_2	0.277	0.000623	0.324	0.00371		
t_2 (ps)	1.77	0.0314	1.06	0.0189		
A_3	0.0439	6.38e-06	0.0285	5.35e-06		

Table 5.8: PIA dynamics fit results of (*R*,*R*)-ProSQ-C16.

Fit parameter	**20 W/cm^2**	**Δ**	**40 W/cm^2**	**Δ**	**80 W/cm^2**	**Δ**
A_1	1.14	0.0163	1.16	0.00269	1.17	0.0011
t_1 (ps)	0.348	0.00374	0.31	0.000619	0.357	0.000342
A_2	0.287	0.00345	0.347	0.00137	0.298	0.000538
t_2 (ps)	3.69	2.12	2.34	0.118	2.89	0.118
A_3	0.0263	0.000327	0.0473	3.46e-05	0.065	2.09e-05
Fit parameter	**200 W/cm^2**	**Δ**	**400 W/cm^2**	**Δ**		
A_1	1.18	0.000455	1.34	0.00108		
t_1 (ps)	0.347	0.000132	0.274	0.000148		
A_2	0.242	0.000219	0.268	0.000604		
t_2 (ps)	2.89	0.0773	1.83	0.0391		
A_3	0.0523	9.36e-06	0.0532	8.14e-06		

Table 5.9: PIA dynamics fit results of *RAC*-ProSQ-C16.

Fit parameter	**20 W/cm^2**	**Δ**	**40 W/cm^2**	**Δ**	**80 W/cm^2**	**Δ**
A_1	0.775	0.00201	0.787	0.000498	0.877	0.000233
t_1 (ps)	0.827	0.0115	0.809	0.00298	0.66	0.000824
A_2	0.311	0.00232	0.272	0.000461	0.26	0.000202
t_2 (ps)	8.22	6.6	10.7	5.37	8.37	1.18
A_3	0.0928	0.000381	0.0824	0.000221	0.0821	5.73e-05
Fit parameter	**200 W/cm^2**	**Δ**	**400 W/cm^2**	**Δ**		
A_1	0.965	0.000347	1.08	0.000325		
t_1 (ps)	0.436	0.000262	0.443	0.000181		
A_2	0.259	0.000118	0.227	8.18e-05		
t_2 (ps)	5.39	0.254	6.25	0.365		
A_3	0.0724	2.21e-05	0.0642	2.18e-05		

References

(1) Zablocki, J.; Schulz, M.; Schnakenburg, G.; Beverina, L.; Warzanowski, P.; Revelli, A.; Grüninger, M.; Balzer, F.; Meerholz, K.; Lützen, A.; Schiek, M. *The Journal of Physical Chemistry C* **2020**, *124*, 22721–22732.

(2) Schulz, M.; Zablocki, J.; Abdullaeva, O. S.; Brück, S.; Balzer, F.; Lützen, A.; Arteaga, O.; Schiek, M. *Nature Communications* **2018**, *9*, 2413.

(3) Arteaga, O.; Ossikovski, R. *JOSA A* **2019**, *36*, 416–427.

Chapter 6

Simulating the Optical Properties of ProSQ-C16 Thin Films

This chapter details the project undertaken during the author's research residence stay at the Zernike Institute of Advanced Materials, University of Groningen under the guidance of Prof. Thomas Jansen. In this chapter, we perform structural simulations to model the steady-state (chiral) optical properties of ProSQ-C16 thin films that were studied experimentally in chapter 5. Utilizing lightweight modelling, we are able to model larger scale chiral molecular aggregates, far beyond the limitations of recent theoretical studies. The simulated spectra of a simple helix structure can well reproduce the chiroptical spectra of (*R*,*R*)-ProSQ-C16 aggregates in solution, validating the feasibility of the presented approach. Furthermore, we demonstrated that the chiroptical spectra of (*R*,*R*)-ProSQ-C16 thin films can be modelled using only transition dipole moment interactions. A structure consisting of two large-scale coexisting chiral aggregates emerges as a suitable candidate. Moreover, we investigate how the simulated spectra evolve when intermolecular charge transfer is accounted for. In this case, a single chiral aggregate is sufficient to replicate the chiroptical properties of the thin film. Finally, we discuss the presented results in the context of other approaches used in literature.

6.1 Introduction

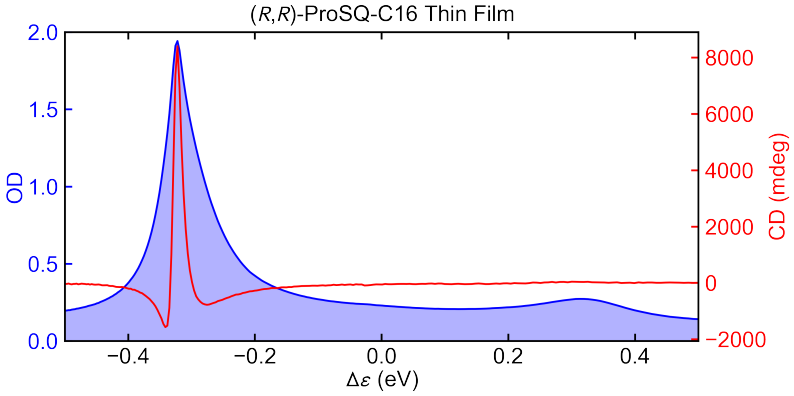

Figure 6.1: Steady-state absorbance (blue) and circular dichroism (red) spectra of an (*R*,*R*)-ProSQ-C16 thin film. The photon energies are plotted relative to the monomer absorption energy.

The intriguing chiral and optical properties of ProSQ-C16 thin films (see Fig. 6.1) have been addressed extensively in chapter 5 as well as in literature [1, 2]. However, a fundamental understanding of the underlying aggregate structure and structure-property relationships of these thin films has not been achieved yet. Painelli and coworkers propose two suitable aggregate structures of enantiopure ProSQ molecules of different alkyl chain lengths in solution [1], introducing once more the idea that intermolecular charge transfer states might strongly affect the optical properties of molecular aggregates [3]. Their approach, based on the essential states model (ESM), was fruitful for aggregates in solution. However, the thin film properties have not directly been addressed in that study. Moreover, the ESM model is inherently complex and computationally demanding, limiting the size of a considered aggregate to only a few molecules. In light of these shortcomings, this chapter aims to reveal the structure-property relationships of enantiopure ProSQ-C16 thin films. This chapter is based on the work conducted during the author's research residence in the group of Prof. Thomas Jansen at the University of Groningen.

In this study, we simulate chiroptical spectra, namely linear absorbance and circular dichroism (CD), using different structural models and intermolecular interactions. The overall simulation schemes utilized in this study can be seen in Fig. 6.2, and

will be explained in more details in the following sections. The simulation architecture consists of three steps: aggregate construction, Hamiltonian parametrization and spectrum calculation. The generalized procedure has been addressed in sections 2.2.1, 2.2.2, and 2.2.3.

Previous reports have shown that the strong CD response of ProSQ-C16 thin films arises not from the intrinsic chirality of each chromophore, but from intermolecular interaction in a chiral structure [2]. Therefore, we propose chiral aggregate structures based on a helix geometry. From each chiral structure constructed, information of chirality can be obtained in the form of the rotation strength, which enters as the key parameter for calculating the CD spectra [4].

For the Hamiltonian framework, Frenkel excitons have been chosen as a starting point. This offers two advantages: simple parametrization and calculation of the Hamiltonian, and an efficient scaling of the structure model up to thousands of molecules. As far as interactions are concerned, two scenarios were considered: purely Coulombic transition dipole moment interactions and intermolecular charge transfer in addition to Coulombic interactions. Each scenario was accounted for by the Hamiltonians introduced in section 2.2.2.

Finally, the spectra are obtained based on the eigenstates of each Hamiltonian and the chiral information of the aggregate structure, following the procedure derived by Lindorfer and Renger [4]. To validate this approach, we first apply these simulations to ProSQ-C16 aggregates in solution, bringing the experimental and simulated absorbance and CD spectra in agreement. Subsequently, we systematically simulate absorption and circular dichroism spectra of different structural candidates and discuss under which circumstances the predictions of the model agree with experimental data. First, the case of the purely Coulombic interaction is investigated, yielding a qualitative agreement to the experimental data if a creeper aggregate coexisting with a helix-structure aggregate is considered. Second, the effects of intermolecular charge transfer on the absorbance and CD spectra are examined, especially how a single structure can replicate the experimental data qualitatively.

The presentation of the simulation results is followed by a discussion of the main achievements, limitations, and shortcomings of this study, and how these results compare to other recent studies [1, 5]. Finally, we summarize our efforts to reveal the chiroptical properties of ProSQ-C16 aggregates in the conclusions part.

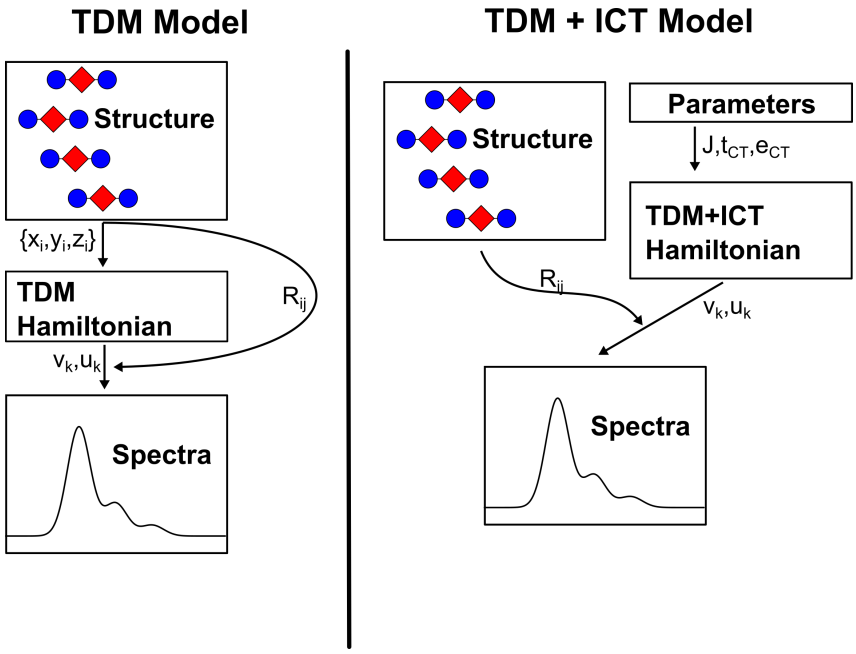

Figure 6.2: Procedures of simulation for the two considered models. (left) The "TDM" model only considers transition dipole moment interactions and is used for simulations 1 and 2. In this model, the molecular positions x_i, y_i, z_i of the aggregate structure (helix in simulation 1, creeper in simulation 2) are used to calculate both the interaction parameters that enter the Hamiltonian, as well as the rotation strength R_{ij}. From the eigenstates v_k and eigenenergies u_k of the Hamiltonian, and rotation strength R_{ij} both absorption and CD spectra can be obtained. The optical properties are therefore completely determined by the structure. (right) The "TDM+ICT" model considers both transition dipole moment interactions and intermolecular charge transfer, and is used for simulation 3. Unlike the "TDM" model, the interactions are not calculated based on the aggregate structure, but are given as free parameters. The aggregate structure is only used to calculate the rotation strength R_{ij}, which is needed to calculate the CD spectrum of the system.

6.2 Results

6.2.1 Simulation 1: ProSQ-C16 in Solution

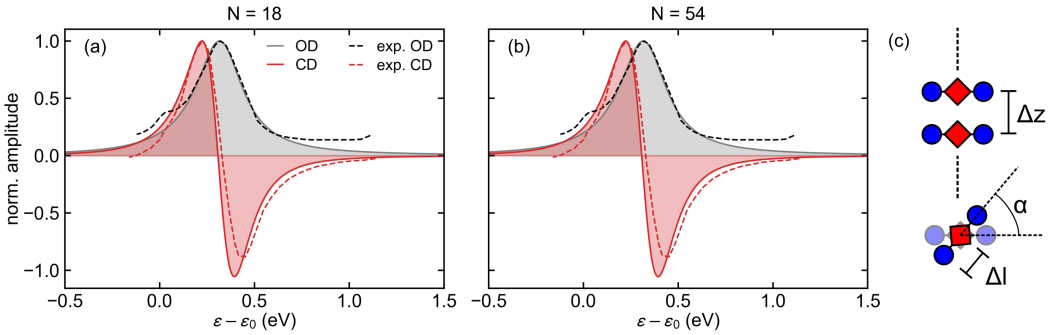

Figure 6.3: Best fit simulation results for the absorbance (grey) and CD (red) spectra of (*R*,*R*)-ProSQ-C16 in acetonitrile solution for N = 18 molecules (a) and 54 molecules (b). Dashed lines indicate the experimental spectra, solid lines the simulated ones. Note that the extended dipole approximation was used. Data obtained from [2]. (c) Parametrization of the helix structure used.

To validate the model and extract first structural parameters, we simulate the absorbance and CD spectra of (*R*,*R*)-enantiomerically pure ProSQ-C16 in acetonitrile solution using the parametrization of a helix structure as described in section 2.2 and Fig. 6.3. The parametrization of each molecule is given by the position of the central oxygen sites as well as the nitrogen sites at the edge of the chromophore. The helix is built so that the center of each molecule is positioned at the center of the helical axis. This results in the positions of the oxygen sites being distributed at cylindrical coordinates $(z,\ r,\ \alpha)$ of $(i \cdot \Delta z,\ 0,\ 0)$ for $i \geq 0$. With respect to the oxygen sites, the nitrogen sites are positioned at a distance of Δl away, symmetrically around the oxygen. With the twisting angle α, the two nitrogen side coordinates can be parametrized as $(i \cdot \Delta z,\ \Delta l,\ i \cdot \alpha)$ and $(i \cdot \Delta z,\ \Delta l,\ i \cdot \alpha + \pi)$, respectively. Following a geometry optimization of the (*R*,*R*)-ProSQ-C16 molecule using the software Avogadro (v1.2.0) [6] and a universal force field (UFF) approach, the parameter Δl was determined to be 6.7 Å.

For this simulation, we only consider transition dipole moment interaction of molecules

i and j and neglect charge transfer interactions, with a Hamiltonian reading

$$H = \sum_i 0\,|i\rangle\langle i| + \sum_{i \neq j} J_{ij}(|i\rangle\langle j| + h.c.). \tag{6.1}$$

The calculation of the transition dipole moment interactions has been conducted based on the molecular positions inside the helix structure as described above, making use of both the point dipole approximation (PDA)

$$J_{ij}^{PDA} \propto \frac{\vec{\mu}_i \cdot \vec{\mu}_j - 3(\vec{\mu}_i \cdot \vec{R})(\vec{\mu}_j \cdot \vec{R})}{|\vec{R}|^3}, \tag{6.2}$$

and the extended dipole approximation (EDA)

$$J_{ij}^{EDA} \propto \left(\frac{q_i^+ q_j^+}{r_i^+ - r_j^+} - \frac{q_i^- q_j^+}{r_i^- - r_j^+} - \frac{q_i^+ q_j^-}{r_i^+ - r_j^-} + \frac{q_i^- q_j^-}{r_i^- - r_j^-} \right). \tag{6.3}$$

Here, μ_i is the transition dipole moment of molecule i (PDA model), which is replaced by the transition charge sites q_i^- and q_i^+ in the EDA. At the same time, the vector connecting two molecules, $\vec{R}$, is replaced by the position of the charge sites r_i^- and r_i^+ (see section 2.2.2 for definitions and more details on the Hamiltonian parametrization). After calculation of the rotation strength of molecules at positions $\vec{r}_i$

$$R_{ij} \propto (\vec{\mu}_i \times \vec{\mu}_j) \cdot (\vec{r}_i - \vec{r}_j), \tag{6.4}$$

the spectra were simulated from stick-spectra using a Lorentzian line shape with a width of 0.1 eV (see section 2.2.3 for further details).

The best fit parameters using the EDA are: $\Delta z = 5.62$ Å and $\alpha = 15°$, and reproduce the steady-state absorption and circular dichroism spectra well, as shown in Fig. 6.3 for N = 18 (a) and 54 (b) molecules long helix aggregates. The experimental optical spectra have been shifted to show the spectra relative to the monomer energy (1.91 eV). The dominant single blue-shifted absorbance peak as well as an accompanying bisignate circular dichroic feature can be qualitatively modelled. This strong blue-shift originates from the interaction between molecules being dominated by the

nearest-neighbor interactions, resulting in positive coupling energies, as long as α is smaller than 90°. For the considered enantiomer, the left-handed helix is yielding the correct sign of the CD spectra, agreeing with the intuitive picture that a left-handed chiral molecule will generate a left-handed chiral superstructure. Although spectral positions and overall line shapes of both the (isotropic) absorbance and CD spectra can be brought into good agreement with the simulation, deviations occur. A minor shoulder peak arises around the monomer energy in the absorbance spectrum, most likely due to residual monomeric molecules in solution, which are not accounted for in these simulations. On the high energy side, the tail of the spectrum shows non-Lorentzian behavior, indicating that disorder or other distorting effects are in play, which also have not been considered beyond the relatively simple model used here.
While the parameters presented above demonstrate the best fit to the data, the overall influence of most parameters on the exact spectra are miniscule. The molecule number N effectively only changes the spacing between aggregate-eigenstates, which does not have a significant impact on the spectral shape for larger aggregate sizes (N>10), given the single bright state and the bisignate nature of CD. On the other hand, the angle α mostly affects the spectral shape and position due to a tuning of the interaction strength. The larger α, the lower the interaction strength between nearest neighbors. For non-nearest neighbors, this effect is even stronger, but these interactions do not significantly influence the resulting spectra. In total, the effect of α on the spectra is not too large and constricted to minor shifts in the exact state energy. Δz has a high impact on the interaction strength and is the main parameter to fit the spectra. Therefore, the confidence in the fitting of Δz should be the highest, while the other parameters are conveniently chosen based on realistic estimations, and can be tuned if necessary.
To confirm the choice of the EDA model over the PDA model, Fig. 6.4 demonstrates the much larger deviation of the PDA model from the experimental data given the same parameters. The strong discrepancy between the needed dimensions of each model clearly shows that the PDA is not a valid approximation of the EDA for these parameters. Since the spectral shift of the PDA spectrum (ca. 1.75 eV) is much larger than the EDA spectrum (ca. 0.25 eV), a fitting PDA spectrum can only be obtained if the interaction strength would be drastically reduced. This could be achieved only if Δz is increased to over 10 Å, leading to a not-tightly-packed lay-

Simulation Parameters	
Parameter	**Value**
N	54 mol.
Δz	5.62 Å
Δl	6.7 Å
α	15°

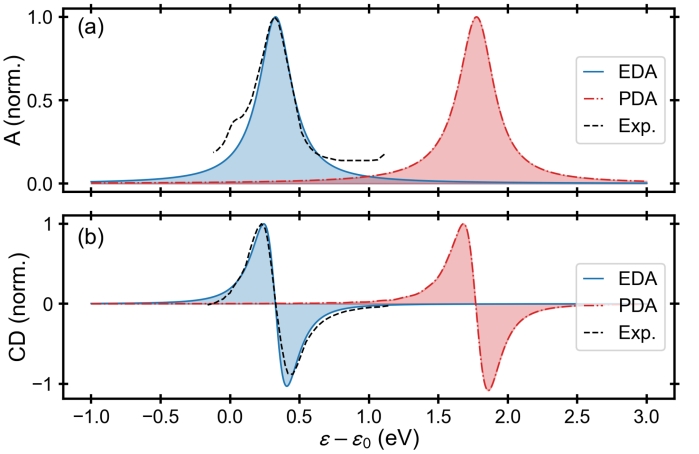

Figure 6.4: Simulation results of the helix aggregate structure with the best-fit parameters of the EDA model, presented on the left. Absorption (a) and CD (b) spectra simulated using best fit parameters and 54 molecules for the EDA (blue) and PDA (red) model. Experimental data is shown in black.

out. Since Δl is even larger than Δz for the simulations presented in Fig. 6.4, it is unsurprising that the interaction energy is vastly overestimated, as the point-dipole approximation should not be valid under those conditions (see section 2.2.2).

6.2.2 Simulation 2: Creeper Aggregates

In order to simulate the optical properties of thin films of (*R*,*R*)-ProSQ-C16, the first structure candidate is termed "creeper aggregate", in accordance to Ref. [5]. In contrast to a helix structure, a creeper structure does not hold the molecules at the center of the axis, but distributes them along the trajectory of a spring instead, with the molecules orienting themselves on the tangent of a circle. This structure enforces a tilted head-to-tail arrangement of the nearest neighbors, which results in a negative interaction energy of the transition dipole coupling, which is expected to result in a J-aggregate-like spectrum.

Parametrization of a creeper structure requires more structural parameters than the helix. We chose the number of molecules N and the length of the chromophore Δl as for the helix and define Δz as the vertical offset per turn of the creeper, R as the

radius of the creeper, and m as the number of molecules per turn of the creeper. Within reasonable parameter estimates, we simulated the chiroptical properties for a large parameter space. An exemplary structure is shown in Fig. 6.5.
Four simulated creeper aggregates with different radii are chosen to demonstrate the

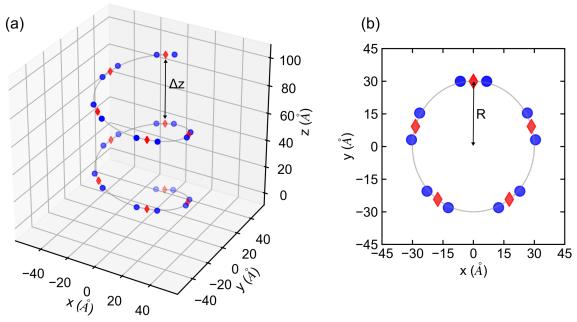

Figure 6.5: Structural configuration of the creeper aggregates used for the simulations. (a) Tilted view on the creeper aggregate structure and the molecular position (red diamond: oxygen site; blue ball: nitrogen site) and a visual representation of the vertical offset parameter Δz. (b) Top view of the tangential alignment of the molecules in the creeper aggregate, with a visual clue for the radius R.

influence of two main parameters: Δz and R. The smallest radius represents a narrow and compact creeper aggregate, with the radius being smaller than the size of a single chromophore. The other radii are integer multiples of the aforementioned radius, and represent a more hollow creeper aggregate, which allows potentially hosting another aggregate in its center. For consistency, the number of molecules per turn (m) and number of overall molecules have been scaled in accordance with the larger radius. This ensures that every creeper is modelled using similar nearest neighbor distances along the spring, and that the creeper makes six turns, a number chosen to balance the proper simulation of inter-ring interaction with the size of the structure. Lastly, m has been offset by -0.5 to ensure that molecules sitting on rings on top of each other do not have a perfect body-to-body geometry, to avoid artificially increased H-like interactions. A summary of the structural parameters is shown the table below.

Table 6.1: Model parameters used for creeper aggregate simulations.

Structure	N	r(Å)	m(mol./turn)
Configuration 1	30	12	4.5
Configuration 2	60	24	9.5
Configuration 3	90	36	14.5
Configuration 4	120	48	19.5

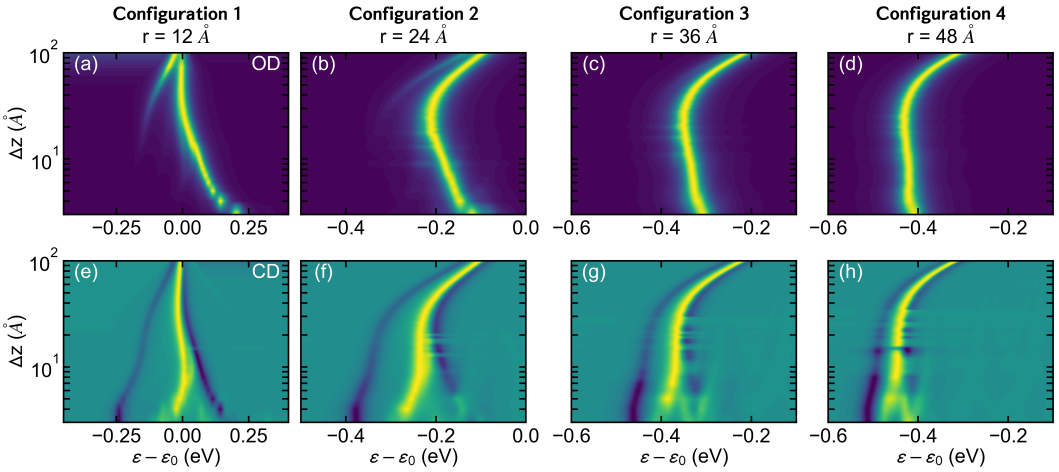

Figure 6.6: Simulated absorption (top row) and CD (bottom row) spectra as a function of vertical offset (Δz) of four exemplary creeper aggregates.

Note that the work flow of this simulation is identical to the one presented in section 6.2.1, with the only difference being the aggregate structure.

In order to probe the effect of Δz, we simulate an array of each of the creeper structures and plot them in a series of contour maps to summarize the effect of the "stretch" of the creeper aggregate and how it relates to different radii. We allow Δz to vary from 3 to 100 Å. Fig. 6.6 shows the overall trend for increasing the stretch of all four configurations. The tight configuration 1 demonstrates the most drastic influence of Δz as the dominant peak changes from a blue-shift to a strong red-shift. The initial blue-shift originates from strong interactions between molecules on nearby rings, which have a more H-like angle, resulting in a positive interaction energy. For larger radii, this interaction competes against a less "kinked" intra-ring interaction,

which increases the negative interaction energy contributions, and trumps the inter-ring interaction, leading to a red-shifted absorption spectrum even for small Δz. For larger Δz values (>20 Å), the absorbance spectrum is dominated by a red-shifted response, as the inter-ring interactions weaken due to the large distance between them. However, a clear side band is arising in all configurations at even lower energies than that of the main band, which is very weak in the absorption spectra of configuration 3 and 4, but can be seen in the CD spectra. The increased split in the more compact configurations suggests that this side peak comes from the Davydov-splitting induced by the non-parallel angles of the nearest-neighbor interactions. As the angle between nearest neighbors is straightened out by larger Δz values, the splitting decreases for larger stretches, before almost merging into a single peak. In order to see the consequences of these spectral trends, Fig. 6.7 shows selected spectral cuts of the contour plots for all configurations.

While the overall trends of the absorption and CD spectra are consistent throughout

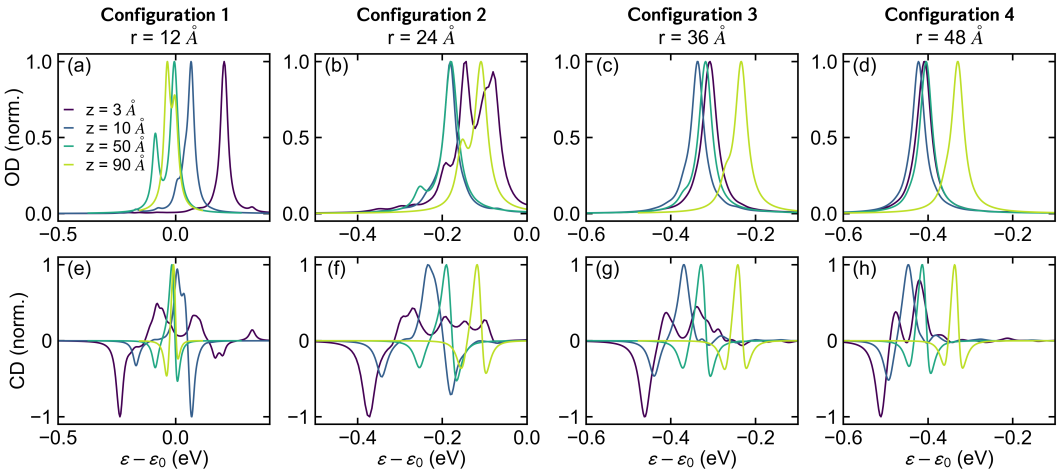

Figure 6.7: Spectral cuts of the simulated absorbance and circular dichroism spectra of different creeper aggregates.

all configurations, the exact spectral shape varies a lot. Model 1 consistently shows contributions from different states throughout all Δz values. For very large Δz values, the contributions come from two states of almost equal strength, and the CD spectrum is dominated by two bisignate features of opposite helicity for each peak seen in the absorption spectrum. This feature is consistent in all configurations, even

though the relative intensity and split between the two dominant peaks is shrinking as the configuration radius increases. For the configuration with the largest R, configuration 4, the two states merge into one state for large Δz values, resulting in one dominant J-like band, which shows a trisignate circular dichroic spectrum, which is comparable with the experimentally obtained CD spectrum of (R,R)-ProSQ-C16 thin films (see also Fig. 6.10).
The resemblance of the wide creeper aggregate with the dominant J-like absorption and trisignate CD feature observed for (R,R)-ProSQ-C16 thin films suggests that the molecules arrange in a geometry where nearest neighbor interactions are mostly head-to-tail and therefore of J-like character with a twisting angle large enough to yield Davydov-split states. Furthermore, a wider creeper aggregate opens the possibility of an internal second aggregate. A suitable candidate to account for the less dominant absorbance and CD response at higher energies than that of the monomer excitons is the helix discussed in the previous section, which has a suitable size to fill the center of the creeper aggregate. Simulations based on this assignment might further improve the model, as the interactions between the helix and the creeper aggregate might significantly alter the optical properties. A simulation of both aggregate structures together is still open to investigation at this time.

6.2.3 Simulation 3: Turning on Intermolecular Charge Transfer

Quantifying intermolecular charge transfer requires detailed knowledge of the orbital overlap of neighboring molecules, which is far beyond the scope of this study. Instead, we disconnect the Hamiltonian from the aggregates structure. To accomplish this, we use the same helix structure that describes the optical properties of ProSQ-C16 in solution, but an independent Hamiltonian with effective parameters not derived from the structure. In this way, we can retain the same helical information as in the first structure—most importantly chiral properties like the rotation strength—while systematically studying the effect of varying intermolecular interactions.
The Hamiltonian used for charge transfer interactions (adopted from section 2.2)

reads

$$H = \sum_i 0\,|i,i\rangle\langle i,i| + \sum_{i\neq k} J(|ii\rangle\langle kk| + h.c.) + \sum_{i\neq j} e_{ij}^{p}\,|i,j\rangle\langle i,j| \\ - \sum_{i,j} t_c(|i,j\pm 1\rangle\langle i,j| + h.c.) - \sum_{i,j} t_c(|i\pm 1,j\rangle\langle i,j| + h.c.). \tag{6.5}$$

Here, $|i,j\rangle$ corresponds to the hole residing on molecule i and the electron on molecule j. The charge hopping parameters t_e and t_h are set to be equal to the general charge hopping parameter t_c. $e_{ij}^{p} = e^{p} - \epsilon' \frac{1}{i-j}$ is the CT state energy given by the polaron energy e^{p} and the Coulomb well depth ϵ'. The Coulomb well depth is set to a reasonably large value of $\epsilon' = 2$ eV, ensuring that only the CT-state with an electron-hole distance of a single molecule have an appropriate energy to couple to Frenkel states. To minimize finite-size effects, the number of molecules in each helix was set to N = 50.

The key parameter investigated in this study is the charge transfer hopping parameter t_c, especially its role in re-distributing oscillator strengths and shifting energies already affected by transition dipole moment coupling, both J-(J<0) and H-(J>0) aggregates. To investigate the impact of charge transfer excitons of a given energy e_{CT}, we simulated the absorption and circular dichroism spectra for a whole array of charge transfer hopping parameter from 0 eV to 0.1 eV. We have considered a transition dipole interaction energy of ± 0.05 eV, allowing the simulation to cover both the weak ($|J|> |t_c|$) and strong ($|J|< |t_c|$) coupling regime. The conditions of each configuration are summarized in the table below.

Table 6.2: Model parameters used for ICT simulations.

Model	**J (eV)**	**e$_{CT}$ (eV)**
Configuration 1	0.05	0
Configuration 2	0.05	0.2
Configuration 3	-0.05	-0.2
Configuration 4	-0.05	0

Model 1 and 2 represent an H-like transition dipole moment interaction, with the energy of the nearest neighbor CT-state either 0.1 eV lower (1) or higher (2) than the optical bright purely Frenkel state at ca. 0.1 eV ($2J$). Complementary, config-

urations 3 and 4 handle the case of a J-like transition dipole moment interaction of the same amplitude, with the CT-state energy being either 0.1 eV lower (3) or higher (4) than the optical bright pure Frenkel state at ≈ -0.1 eV ($2J$) relative to the monomer.

Fig. 6.8 shows the resulting spectra as contour plots for the four considered configu-

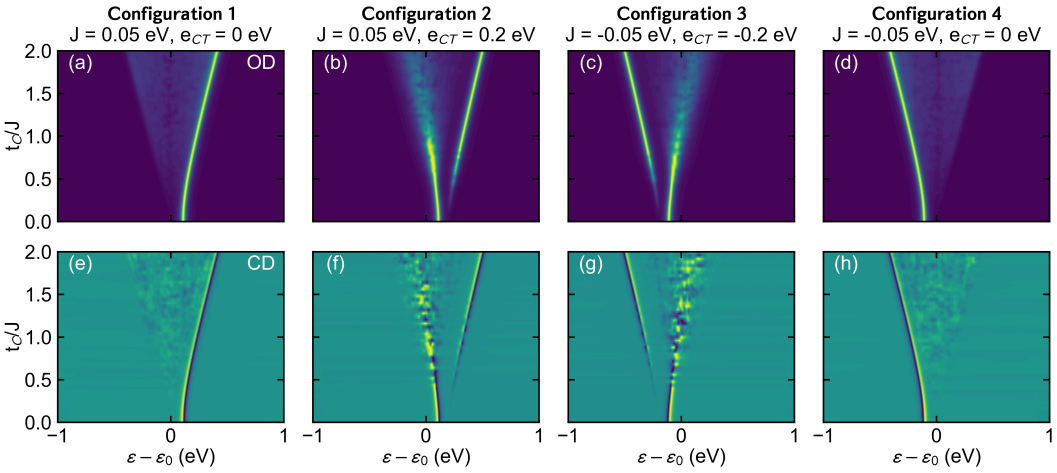

Figure 6.8: Spectral impact of charge transfer hopping parameter t_c on aggregated J- and H-aggregates; (a-d) Contour plots of the absorbance spectra as a function of t_c. (e-h) Contour plots of the circular dichroic spectra as a function of t_c.

rations. Overall, configurations 1 and 4 appear as mirror images of each other, as do configurations 2 and 3. As the interaction scheme should be symmetric with respect to the sign of the interactions and energies involved, this is well expected (see section 2.2.2). Comparing configurations 1 and 2, the influence of the energetics of the CT energy becomes pronounced. In configuration 1, increasing the charge transfer hopping energy leads to a consistently more pronounced blue-shift of the dominantly absorbing peak, while a band of weakly absorptive states appear at lower energies. The width of this band seems to rise linearly with the value of the charge transfer hopping parameter.

In terms of circular dichroism, most of the CD signal appears to be still bisignate, and located at the dominantly absorbing H-peak, while a residual CD signal is seemingly randomly spread inside the slightly absorptive band at lower energies. This monotonic behavior with increasing charge transfer hopping is not replicated for con-

figuration 2. Here, a splitting appears even for small charge transfer hopping energies below the transition dipole moment interaction energies, in which the dominantly absorbing H-peak is red-shifted, with another single blue-shifted band appearing with respect to the initial H-peak. Once t_c is approaching more significant values of around 0.02 eV, the absorption strength of the two peaks is redistributed towards the blue-shifted side peak, which eventually becomes the dominant absorptive state for t_c values above 0.04 eV. At the same time, the initially dominant, red-shifted peak seems to spread its oscillation strength to energetically nearby states. This results in a washed-out band of absorption, which contrary to configuration 1 is not homogeneously spread. This absorption band carries a considerable, yet unstructured amount of the total circular dichroism signal, while the dominantly absorptive peak is demonstrating the same bisignate feature as in configuration 1. These observations are also valid for a respective comparison between configuration 3 and configuration 4.

More detailed insights can be found by comparing selected simulated absorption and

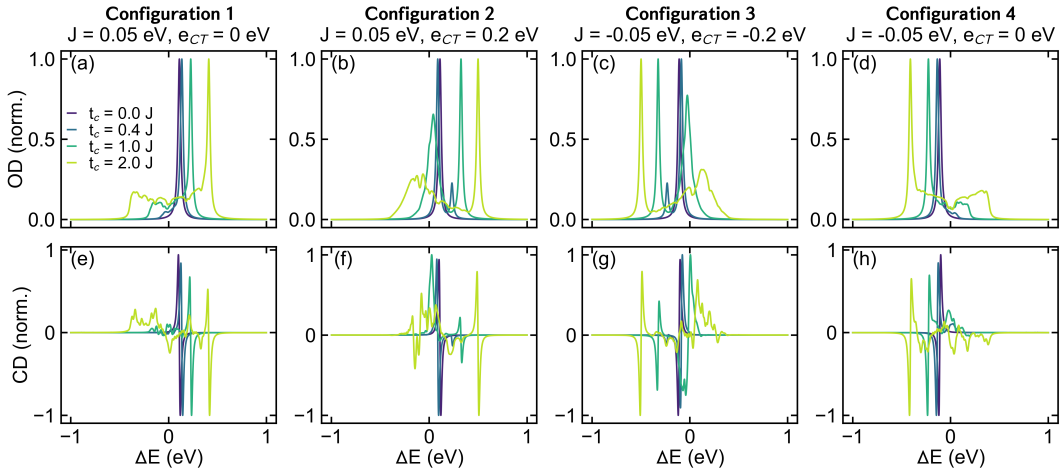

Figure 6.9: Spectral cuts out of Fig. 6.8 for t_c values of 0, 0.02, 0.05 and 0.1 eV; (a-d) Absorbance spectra of the different configurations; (e-h) CD spectra.

CD spectra with each other, as seen in Fig. 6.9. While the line shape of the main absorption peak and its related CD line shape is consistent in all spectra, the exact distribution of oscillator strength and circular dichroic contributions in the extended, less absorptive band shows strong fluctuations. The line shapes of the absorption

spectra are subject to random fluctuations, especially in configurations 2 and 3. This holds true for configurations 1 and 4 as well, but to a lesser extent. For all configurations, the CD spectra demonstrate significantly higher fluctuations in the spectra, which do not seem to follow any rational for the spectral range of the slightly absorptive band. This feature might be an artifact of the mapping of the "non-chiral" CT-Frenkel hybrid states on the chiral structure, which might be worsened by finite size effects, as in a disorder-free configuration, long distance contributions to the rotation strength have to be considered. This complication may be tackled by adding disorder to the structure and using a configuration of a higher dimensional aggregate in the future. Even with the limitations in the simulated spectra, we can draw some conclusions on how intermolecular charge transfer might be present in thin films of (*R*,*R*)-ProSQ-C16.

First, the experimentally obtained absorbance line shape of a dominant, sharp absorption line followed by a continuum can be already rationalized by considering a simple one-dimensional chain aggregate and intermolecular charge transfer. The low spectral position of maximum absorption in the experimental data can only be realized if the transition dipole moment interaction is of J-like character, yielding a negative Coulombic coupling energy. Since the continuum as well as the red-shift scales strongly with t_c, the charge transfer integral must be significant to account for the more than 0.1 eV shift observed in the experimental data. Finally, the majority of the CD signal is condensed into the sharp absorption line only if $e_{CT} \in [e_{mon}, 2J)$. Overall, the experimental results can be relatively well simulated with configuration 4 (see Fig. 6.10).

While configuration 4 is the most suitable candidate, many optimizations could still be made to cater the model used here more accurately to the experimental data. First, the model parameters need to be fitted to the experimentally obtained absorption data using the effective Hamiltonian approach. Second, a structure has to be found that actually yields the fitted model parameters based on its geometry, which is especially important for J and t_c, as they have a strong dependence on the intermolecular orientation. In the context of a quasi-one-dimensional model as considered here, an appropriate starting point for the aggregate structure would be a hybrid between helix and creeper geometries, as the molecules adopt a head-to-tail arrangement while staying either on axis with their center of mass or following a

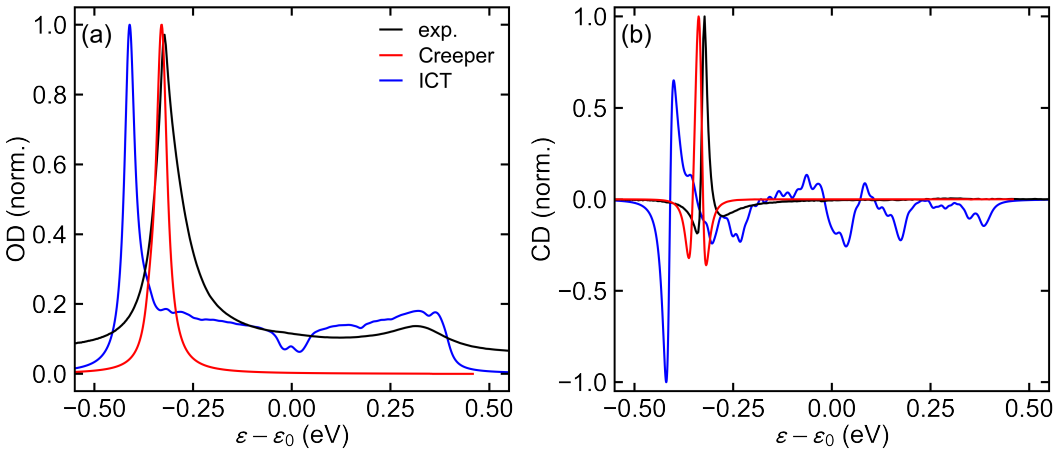

Figure 6.10: The best fitting results of simulations 2 and 3 to the experimental results ("exp", blacklines) in terms of (a) absorbance and (b) CD. From simulation 2 ("Creeper", red lines) configuration 4 (z = 90 Å) was chosen. From simulation 3 ("ICT", blue lines), configuration 4 (t = 2J) was chosen.

creeper spring with a radius much smaller than the extent of the molecule. Following these steps, different related structures might be derived.

A weak point of the models incorporating intermolecular charge transfer is the persistent bisignate CD signature of the main absorption line, opposite to the trisignate spectral shape observed in the experimental data. As the experimental CD of this peak as well as the simulated ones are conserved, the differences in shape might be addressed by considering different band widths of the states absorbing left- and right-hand polarized light. In this context, the double sign-change observed in the experimental data stems from a broad negative excitonic CD response, and a narrow positive CD response, which is enveloped by the wider negative CD response on both sides. In order to grasp such an effect in the simulation, energetic disorder can be considered, which might introduce state-specific exciton band broadening. Furthermore, the introduction of energetic disorder could localize the collective aggregate exciton states, which has major implications on the rotation strength of each state, and therefore the circular dichroism spectra. The implementation of energetic disorder is computationally very costly, as a statistical ensemble of simulations must be created to properly account for the randomly disordered monomer energy levels, which is beyond the scope of this project.

6.3 Discussion

Our results are well in line with the work of the Giavazzi *et al.*, which have predicted a similar scheme of either two separate aggregates or a single aggregate with a considerable intermolecular charge transfer, even if the focus of their work was more on the aggregation in solution rather than thin films [1]. However, their work uses more sophisticated and complete essential states models and has been generally crafted as a more comprehensive and complete work. In the following, we address the biggest differences between this work and Ref. [1], and what we can learn from the here presented simplified approach in a direct comparison to more sophisticated approaches.

As mentioned in Ref. [1], there are several drawbacks of the exciton model that we have used in this work as opposed to a full essential states model of the aggregate. Most importantly, the polarizability of molecules and charge redistribution due to Coulombic interaction with the neighboring molecules is completely neglected, which they have shown to impact especially the chiroptical properties of the dimer system [1]. On the other hand, the total number of state involved in a N molecule aggregate is given at 3^N, which limits the aggregate size of their simulation to around 9 molecules, or around twenty thousand states. In the case of this model, only the excitonic states where a single molecule is (once) excited are relevant for the Hamiltonian. The number of states considered is therefore equal to N, allowing us to perform simulations of much larger aggregate systems even on personal tabletop hardware. Enabling $N > 10$ is crucial for allowing larger structures like the large radius creeper aggregates described in section 6.2.2, where multiple turns of molecules along the spring structure have to be considered to properly weigh the interaction strength between the inter- and intra-ring neighboring molecules.

While parts of the drawbacks of using the exciton model are mitigated by choosing the extended dipole approximation, it is worth noting that appointing the transition charges as point-like charges is another crude approximation and should be replaced by a transition charge density for more accurate interaction energies. Moreover, the effective arm length of the ProSQ-C16 chromophore has been estimated in Ref. [1]

by fitting essential states model parameters to the monomeric spectrum, yielding an arm length of $\Delta l = 4.33$ Å, which is significantly smaller than the 6.7 Å used in this work, and present a point for potential improvements of the simulations. Lastly, the more variable model presented in Ref. [1] includes the neighbor displacement along the molecular axis x as an additional parameter. The case where $x = 0$ is identical to the helix aggregate reported above. For $x > 0$, the model adopts a creeper-like geometry similar, but not identical to the one used in this study. The two main differences are that in the model presented here, the alignment of the molecules is truly tangential to the radius, and that the molecular axis is not perpendicular to the creeper axis but follows the spring geometry. Especially the latter is an important aspect for the simulated spectra, as the qualitatively suitable simulated spectra of this study require a significant component of the molecular axis to be parallel to the creeper axis. This suggests future investigations adopting a structure which is similar to what has been presented in this work, using the more elaborate essential states model as presented in Ref. [1] could be beneficial.

Compared to models incorporating intermolecular charge transfer, the drawback of the essential states model is becoming more evident, as the tetramer considered in Ref. [1] already requires an inclusion of 10453 states. In contrast, the base chosen for the calculations in this study scales with N^2, which allows for simulations of aggregates up to more than 100 molecules. The strong limitation of aggregate size is especially problematic for the circular dichroic properties, as delocalization of the excitonic states allows for large rotation strengths of eigenstates and therefore large CD signals [4], which can hardly be explored in a mere tetramer. Furthermore, the charge transfer hopping energies have to be inflated to account for the finite size effects in the essential states model [1, 3]. This suggests that to capture the chiroptical properties of the large ProSQ-C16 aggregates in thin films, the essential states model is insufficient, and a more lightweight approach is needed to capture essential properties.

In an alternative take on intermolecular charge transfer, Manrho, Jansen and Knoester have presented the effect of one-dimensional aggregates featuring both Frenkel and intermolecular charge transfer excitons of arbitrary size, demonstrating linear absorption properties in high degree of agreement with the absorption spectrum of enantiopure ProSQ-C16 thin films [7]. As the simulations conducted in the present

work are supposed to be covered by the generalized observations of Manrho *et al.*, the similarities between the absorption spectra of this work and Ref. [7] act as validation for the model used for the linear absorption.
Beyond the limitations of the CD calculations based on the mapping of generic eigenstates onto a chiral structure, the methodology presented here might have another problem in the presence of charge transfer states: common CD models have been based on purely Frenkel exciton models sitting on single molecules and did not account for ICT states connecting multiple molecules [1]. While the simple approach used in this work on the ICT Hamiltonian only considers transition dipole moments of the Frenkel excitons, it is unclear if the CD is only influenced by the Frenkel part of each eigenstate. Further theoretical investigations are needed to answer this question.

6.4 Conclusions

Overall, we have demonstrated simple structural and interaction schemes that qualitatively explain the linear absorption and circular dichroism properties of ProSQ-C16 molecules both in solution and annealed thin films. Chiral ProSQ-C16 aggregates in solution were successfully modelled using a helix model, where the center of the molecules is located at the helical axis, while only transition dipole interaction of optically bright excitons was considered. For chiral ProSQ-C16 aggregates in the annealed thin film, our results suggest that either a stretched creeper-aggregate in combination with a helix-aggregate can replicate the absorption and CD features, if only transition dipole moment interactions are considered, or that a single type of aggregate can account for the chiroptical properties if intermolecular charge transfer is considered.
Our results and comparison with literature demonstrate the difficulties of balancing the complexity of a model and its scalability, especially in covering chiroptical properties of aggregates. While quantitatively fitting simulated spectra have not been highly successful, the qualitative agreement of experiment and simulations shows that simplified models can be effectively used to roughly estimate the underlying structure-property relationships in molecular aggregates. Our study will serve as a base for future studies on large-scale aggregated systems, which cannot be accounted

for using more heavyweight modelling.

6.5 Contributions

Robin Bernhardt and Paul van Loosdrecht conceived the project. Robin Bernhardt conducted the simulations. Paul van Loosdrecht and Thomas la Cour Jansen supervised the project.

References

(1) Giavazzi, D.; F. Schumacher, M.; Grisanti, L.; Anzola, M.; Maiolo, F. D.; Zablocki, J.; Lützen, A.; Schiek, M.; Painelli, A. *Journal of Materials Chemistry C* **2023**, *11*, 8307–8321.

(2) Schulz, M.; Zablocki, J.; Abdullaeva, O. S.; Brück, S.; Balzer, F.; Lützen, A.; Arteaga, O.; Schiek, M. *Nature Communications* **2018**, *9*, 2413.

(3) Hestand, N. J.; Zheng, C.; Penmetcha, A. R.; Cona, B.; Cody, J. A.; Spano, F. C.; Collison, C. J. *The Journal of Physical Chemistry C* **2015**, *119*, 18964–18974.

(4) Lindorfer, D.; Renger, T. *The Journal of Physical Chemistry B* **2018**, *122*, 2747–2756.

(5) Bertocchi, F.; Sissa, C.; Painelli, A. *Chirality* **2023**, *35*, 681–691.

(6) Hanwell, M. D.; Curtis, D. E.; Lonie, D. C.; Vandermeersch, T.; Zurek, E.; Hutchison, G. R. *Journal of Cheminformatics* **2012**, *4*, 17.

(7) Manrho, M.; Jansen, T. L. C.; Knoester, J. *The Journal of Chemical Physics* **2022**, *156*, 224112.

Summary

The scope of this work covers the ultrafast and steady-state photophysical and excitonic properties of aggregates and blends based on the squaraine molecules nBSQ and ProSQ-C16, targeted for photodetection, photovoltaic and chiroptical applications. In detail, we utilized ultrafast transient absorption spectroscopy and steady-state absorption and emission spectroscopy, employing both experimental and simulation approaches. The use of a white light supercontinuum probe in transient absorption enabled us not only to study the lifetime of excitons, but also reveal their physical nature. Complementary to the experimentally obtained spectra, lightweight simulations of both steady-state and ultrafast transient spectra were employed. This approach unfolded the underlying large-scale aggregate structure, revealing the structure-property relationships in squaraine-based molecular aggregates.

We first investigated the photophysical properties of aggregated, annealed thin films of nBSQ. Its broad "double-hump" absorbance spectrum as well as the surprising lack of photoluminescence contradict predictions of standard exciton theory. We deployed ultrafast transient absorption spectroscopy on this system for the first time to reveal that both of the humps in the steady-state absorption originate from the same aggregate structure. Furthermore, we applied a disordered structure model based on a Frenkel exciton Hamiltonian to successfully replicate not only steady-state absorbance and photoluminescence properties, but also early time transient properties. Fitting of the model to the experimental data revealed an ensemble of aggregates with average sizes in the order of 10 nBSQ molecules, which is beyond the limitation of models used in previous works. Based on our experimental and simulated outcomes, we have proven that structural disorder of the aggregate and

simple Coulombic interactions are sufficient to explain both the established exotic steady-state optical properties and newly reported transient spectral features. This study has been published in the *Journal of the American Chemical Society* in 2022. Although most of the steady-state and transient optical properties of nBSQ aggregates can be explained by the structural disorder model, it cannot capture the transient dynamics for longer delay times, especially beyond 200 ps. In order to understand the origin of the transient dynamics and which non-Frenkel-exciton states contribute to it, we conducted another set of ultrafast transient absorption spectroscopy measurements on the annealed nBSQ thin film, as well as an donor-acceptor blend thin film of nBSQ and $PC_{61}BM$ in a weight ratio of 2:3. Using different photoexcitation energies, we selectively excited either nBSQ or PCBM. In both thin films, a derivative-like feature manifested for delay times longer than the exciton lifetime of around 200 ps. When the PCBM component was excited, only the derivative-like feature emerged as a signal, without the bleach signatures of the Frenkel excitons in nBSQ. Based on the spectral and dynamic footprints of the feature, we assigned it to photoinduced electroabsorption (EA). The origin of the photoinduced EA signal in donor-acceptor blends is well known to be from charge separated states. The fast rise time of the EA signal when PCBM is excited suggests an efficient, delocalized-wave function driven charge separation process. Contrary to the blend film, photoinduced EA signals have not been reported so far for single chromophore systems to the best of our knowledge. This marks nBSQ aggregates as the first such system exhibiting this transient response. We concluded that this strong EA response originates from semi-delocalized intermolecular charge transfer (ICT) states spanning over multiple molecules, which persist much longer (≈ 2 ns) than the Frenkel excitons. Our results underlined the importance of non-Frenkel-like states, and especially ICT states for the optical properties of nBSQ beyond the steady-state absorption.

The second series of aggregated squaraine systems investigated in this thesis contained enantiopure and racemic thin films of the prolinol-derived ProSQ-C16. This squaraine features the same chromophore as nBSQ, but possesses different, chiral side groups. Enantiopure ProSQ-C16 thin films are known for their extreme coupling to circularly polarized light, evident by a circular dichroism (CD) signal orders of magnitude higher than that of conventional molecular aggregates. Additionally, their absorbance features multiple absorption bands, dominated by a red-shifted ab-

sorption band of odd shape, while low photoluminescence yield is present at the same time. Despite these unique optical features, the aggregate structure of ProSQ-C16 is not well-understood, and the role of chirality for the optical properties beyond CD effects remains elusive. Once more, we employed ultrafast transient absorption spectroscopy to investigate the structure-property relationship in these materials, comparing enantiopure and racemic thin films. For enantiopure ProSQ-C16 thin films, transient absorption spectra are dominated by a threefold response of ground state bleach, stimulated emission, and two-exciton absorption, indicative for a J-aggregate-like character. This response was consistent across different photoexcitation conditions for the enantiopure thin films. However, this does not completely hold true for the racemic thin films, whose transient response is more convoluted and dependent on the photoexcitation energy. Based on our results and previous theory work, it was concluded that optical properties of the enantiopure thin film emerge from a single type of aggregate, which features a strong drive for ICT. On the other hand, multiple aggregates must be considered to fully grasp the transient response of the racemic thin film. Moreover, through singular value decomposition of the transient response, we revealed a dark excitonic state. This state mediates the fast relaxation dynamics from the initially photoexcited state to the ground state, explaining the observed lack of fluorescent emission. This study has revealed the strong impact of non-Frenkel-exciton states on the optical properties of chiral ProSQ-C16 aggregates.

Complementary to the experimental study conducted on ProSQ-C16 thin films, we conducted a theoretical investigation into the steady-state optical properties of enantiopure ProSQ-C16 aggregates. This project was conducted at the University of Groningen under the guidance of Prof. Thomas Jansen. Unlike previous models used to simulate the optical properties of ProSQ molecules in solution, we did not resort to the essential states model (ESM), but a much more simplified Frenkel exciton model. This allowed us to consider chiral aggregate structures of large scale ($>$10 molecules), far beyond the very limited aggregate size feasible in the ESM. Based on large scale aggregation models, we were able to simulate both the absorbance and CD spectrum of a given structure. Our model was validated by successfully simulating the more ordinary absorptive and chiral properties of ProSQ-C16 aggregates in solution. For the chiroptical properties of the thin films, we were able to find

suitable structure candidates. If only Frenkel excitons and Coulombic interactions are considered, we established that a large-scale "creeper" aggregate coexisting with a helix geometry aggregate might qualitatively describe the chiroptical properties of the thin film. Under the consideration of ICT states, even a single aggregate was found to be able to qualitatively reproduce the absorbance. The applicability of the ICT model to the CD spectra remained ambiguous. Our study has proven once more that large-scale aggregation geometries and intermolecular interaction both can contribute significantly to the exotic optical properties of molecular aggregates.

In addition to the scientific outcome presented above, this thesis also entails an introduction to the photophysical properties of organic dye molecules and their aggregates. Moreover, the concepts of ultrafast and steady-state optical spectroscopy are presented, together with the experimental realisation of these spectroscopy techniques. Besides the experimental methods, structural modelling and simulation techniques are introduced.

In summary, this thesis focuses on the steady-state and transient photophysical properties of squaraine-based molecular aggregates. Using various optical spectroscopy techniques and simulations, we successfully resolved the structure-property relationships of two highly unconventional aggregated squaraine systems. Our results underline the importance of considering large-scale aggregate structures and non-Frenkel-exciton states.

Zusammenfassung

Diese Arbeit umfasst die ultrakurzen sowie statischen photophysikalischen und exzitonischen Eigenschaften verschiedener organischer Lösungen und Festkörper auf der Basis von Squarain Molekülen, welche von besonderem Interesse für Anwendungen als Photodetektor oder in der Photovoltaik sind. Zu diesem Zweck verwendeten wir ultrakurze transiente Absorptionsspektroskopie und statische Absorptions- und Emissionsspektroskopie, sowohl experimentell als auch simuliert. Das Nutzen eines Weißlicht Superkontinuums als Abfragepuls erlaubte uns, nicht nur die Lebenszeit diverser Anregungen zu studieren, sondern auch deren physikalische Natur. Komplementär zu unseren experimentellen Studien wurden leichtgewichtige Simulationen verwendet, sowohl von den statischen, als auch den transienten Spektren. Dieser zweigleisige Ansatz offenbarte die zugrundeliegenden Aggregatstrukturen und damit die Struktur-Eigenschafts-Beziehungen dieser komplexen Materialien.
Zunächst haben wir die photophysikalischen Eigenschaften aggregierter, getemperter Dünnfilme des Squarain Moleküls nBSQ untersucht. Dieses System ist bekannt für das ebenso begehrte wie ungewöhnliche panchromatische Absorptionsspektrum, welches zwei breite absorbierende "Höcker" aufweist. Dieses exotische Absorptionspektrum sowie das überrraschende Fehlen der Photolumineszenz widersprechen der Voraussagungen der gewöhnlichen Exziton-Theorie. Wir setzten erstmals ultraschnelle transiente Absorptionsspektroskopie an diesem System ein, um zu enthüllen, dass beide "Humpen" von derselben Aggregatstruktur stammen. Darüber hinaus wandten wir ein ungeordnetes Strukturmodell basierend auf dem Frenkel-Exziton Hamiltonian an, welches nicht nur die statischen, sondern auch die kurzzeitigen transienten Eigenschaften bestätigen konnte. Basierend auf den experimentellen und simulierten Daten haben wir bewiesen, dass strukturelle Unordnung und einfache

intermolekulare Coulombsche Wechselwirkungen ausreichen, um nicht nur die statischen optischen Eigenschaften, sondern auch die von uns beigetragenen transienten optischen Eigenschaften zu verstehen. Diese Studie wurde 2022 in dem *Journal of the American Chemical Society* veröffentlicht.

Obwohl die meisten statischen und transienten optischen Eigenschaften von nBSQ Aggregaten durch das Modell struktureller Unordnung erklärt werden können, kann die transiente Dynamik bei längeren Verzögerungszeiten nicht von diesem Modell erfasst werden. Um den Ursprung der transienten Dynamik sowie den beteiligten Nicht-Frenkel-Exziton Zuständen zu verstehen, führten wir eine weitere Reihe von ultraschnellen transienten Absorptionsspektroskopiemessungen durch, dieses Mal sowohl für einen reinen nBSQ Dünnfilm als auch einen Dünnfilm aus einem nBSQ:$PC_{61}BM$ Donor-Akzeptor-Gemisch im Gewichtsverhältnis 2:3. Mit unterschiedlichen Anregungsenergien konnten wir selektiv entweder nBSQ oder PCBM anregen. In beiden Dünnfilmen manifestierte sich ein Ableitungs-ähnliches Signal im transienten Absorptionsspektrum, vor allem für Verzögerungszeiten oberhalb der Exzitonlebensdauer von etwa 200 ps. Wurde PCBM selektiv angeregt, trat sogar nur das Ableitungsähnliche Signal, abseits jeder Signatur eines Frenkel-Exziton, auf. Basierend auf dem spektralen und dynamischen Fingerabdruck ordnen wir das Signal photoinduzierter Elektroabsorption (EA) zu. Die Herkunft des photoinduziertem EA Signals sind für Donor-Akzeptor-Gemische bekannterweise ladungsgetrennte Zustände. Die schnelle Anstiegszeit des Signals nach PCBM Anregung deutet auf eine schnelle, ballistische Ladungstrennung hin. Im Gegensatz zu den Gemischen wurde nach unserem besten Wissen noch kein starkes photoinduziertes EA Signal in Systemen eines einzelnen Chromophor-Typs nachgewiesen. Dementsprechend sind nBSQ Aggregate das erste derartige System bisher, welches diese Reaktion zeigt. Wir kamen zu dem Schluss, dass das starke EA Signal von halb-delokalisierten intermolekularen Ladungszuständen (ICT) hervorgerufen wird, welche sich über mehrere Moleküle erstrecken und viel länger (ca. 2 ns) als Frenkel-Exzitonen Bestand haben. Unsere Ergebnisse unterstreichen die Bedeutung von Nicht-Frenkel-Exziton Zuständen und insbesondere ICT Zuständen für die optischen Eigenschaften von nBSQ, die weitergehen, als die reine statische Absorption.

Die zweite Serie von aggregierten Squarain-Systemen, die in dieser Arbeit untersucht wurde, enthielt enantiopure und razemische Dünnfilme aus ProSQ-C16. Dieses

Squarain besteht aus demselben Chromophor wie nBSQ, besitzt jedoch andere, chirale Seitengruppen. Enantiopure ProSQ-C16-Dünnfilme sind für ihre extreme Kopplung zu zirkular polarisiertem Licht bekannt, erkennbar an einem gigantischen Zirkulardichroismus (CD) Signal, dass um Größenordnungen höher ist als üblich für molekulare Aggregate. Zusätzlich weist das Absorptionsspektrum mehrere Absorptionsbänder auf, dominiert von einem rotverschobenen Absorptionsband ungewöhnlicher Form, welches nur schwach photolumineszent ist. Trotz dieser einzigartigen optischen Eigenschaften ist die Aggregatstruktur von ProSQ-C16 nicht gut verstanden, und die Rolle der Chiralität für die optischen Eigenschaften bleibt über die starken CD-Effekte hinaus unklar. Einmal mehr setzten wir ultraschnelle transiente Absorptionsspektroskopie ein, um die Struktur-Eigenschafts-Beziehung in diesen Materialien zu untersuchen, wobei enantiopure und razemische Dünnfilme verglichen wurden. Für enantiopure ProSQ-C16-Dünnfilme werden die transienten Absorptionsspektren von einem dreifachen Signal aus Grundzustandsbleiche, stimulierter Emission und Zwei-Exzitonen-Absorption dominiert, was auf einen J-Aggregat-ähnlichen Charakter hindeutet. Dieses Signal war konsistent trotz verschiedener Photoanregungsbedingungen für beide enaniopure Dünnfilme. Dies gilt jedoch nicht vollständig für den razemischen Dünnfilm, dessen transiente Spektren komplizierter sind und von der Photoanregungsenergie abhängen. Basierend auf unseren Ergebnissen und früheren Theoriearbeiten wurde geschlossen, dass die optischen Eigenschaften des enantiopuren Dünnfilms auf einen einzelnen Aggregat-Typ rückführbar sind, welcher einen starken Drang zu intermolekularen Ladungstransfer aufweist. Dem entgegengesetzt müssen mehrere Aggregate berücksichtigt werden, um das transiente Signal des razemischen Dünnfilms vollständig zu erfassen. Darüber hinaus enthüllten wir durch Einzelwertzerlegung des transienten Signals einen dunklen Exzitonzustand. Dieser Zustand vermittelt die schnelle Relaxationsdynamik des anfänglich photoangeregten Zustandes hin zum Grundzustand und erklärt das Fehlen der Photolumineszenz. Diese Studie hat den eindeutig starken Einfluss von Nicht-Frenkel-Exziton-Zuständen auf die optischen Eigenschaften von chiralen ProSQ-C16 Aggregaten offenbart.
Ergänzend zur experimentellen Studie an ProSQ-C16-Dünnfilmen, führten wir eine theoretische Untersuchung der statischen optischen Eigenschaften von enantiopuren ProSQ-C16-Aggregaten durch. Dieses Projekt wurde an der Universität Groningen unter der Betreuung von Prof. Thomas Jansen durchgeführt. Im Gegensatz zu

früheren Modellen, welche zur Simulation der optischen Eigenschaften von ProSQ-Molekülen in Lösung verwendet wurden, griffen wir nicht auf das Essential States Model (ESM) zurück, sondern auf das viel einfachere Frenkel-Exziton-Modell. Dies ermöglichte es uns, chirale Aggregatstrukturen von größeren Dimensionen zu betrachten (>10 Moleküle), weit über die im ESM realisierbare, sehr begrenzte Aggregatgröße hinaus. Basierend auf großdimensionierten Aggregatmodellen konnten wir sowohl das Absorptions- als auch das CD-Spektrum einer gegebenen Struktur simulieren. Die Gültigkeit unseres Modells wurde überprüft, indem wir erfolgreich die deutlich gewöhnlicheren absorptiven und chiralen Eigenschaften von ProSQ-C16-Aggregaten in Lösung simulierten. Auch für die chiroptischen Eigenschaften der Dünnfilme konnten wir geeignete Strukturkandidaten finden. Wenn nur Frenkel-Exzitonen und Coulombsche Wechselwirkungen berücksichtigt werden, konnten wir feststellen, dass ein "Creeper"-Aggregat von großem Maßstab, welches mit einem helixförmigen Aggregat koexistiert, die chiroptischen Eigenschaften des Dünnfilms qualitativ beschreibt. Unter Berücksichtigung von ICT-Zuständen wurde festgestellt, dass sogar ein einzelnes Aggregat die Absorption qualitativ reproduzieren kann. Die Anwendbarkeit des ICT-Modells auf die CD-Spektren blieb unklar. Unsere Studie hat einmal mehr bewiesen, dass sowohl größer dimensionierte Aggregationsgeometrien als auch intermolekulare Wechselwirkungen exotische optische Eigenschaften in molekularen Aggregaten hervorbringen können.

Zusätzlich zu den oben dargestellten wissenschaftlichen Ergebnissen umfasst diese Arbeit auch eine Einführung in die photophysikalischen Eigenschaften organischer Farbstoffmoleküle und ihrer Aggregate. Darüber hinaus werden die Konzepte der ultraschnellen und statischen optischen Spektroskopie vorgestellt, zusammen mit der experimentellen Umsetzung dieser Spektroskopietechniken. Neben den experimentellen Methoden werden auch Strukturmodellierung und Simulationstechniken eingeführt.

Zusammenfassend konzentriert sich diese Arbeit auf die statischen und ultraschnellen photophysikalischen Eigenschaften von auf Squarainen basierenden molekularen Aggregaten. Mit Hilfe verschiedener optischer Spektroskopietechniken und Simulationen konnten wir erfolgreich die Struktur-Eigenschafts-Beziehungen von zwei hochgradig unkonventionellen aggregierten Squarainen-Systemen aufklären. Unsere Ergebnisse unterstreichen die Bedeutung der Berücksichtigung von großdimensionalen Aggre-

gatstrukturen und Nicht-Frenkel-Exziton-Zuständen.

Acknowledgements

The conclusion of this thesis also marks the end of a spectacular time I had at the University of Cologne. This place has felt like home for the last ten years, and I have enjoyed the company of many great people here.
First and foremost, I want to thank my supervisor and "Doktorvater" Prof. Paul van Loosdrecht for more things than I can mention here. You gave me the opportunity to do this PhD project in the first place, even though my experience with organic materials was constrained to grocery shopping. For the amount of trust you put in me, that you believed I could master a new setup, new materials, and even some theory, I want to say thank you from the bottom of my heart. Your lighthearted outlook on life and the world of science always helped to keep the spirits up high, and reminded me to not take problems, or myself, too seriously. Whenever I needed help, you always made sure to take time for me, even if it ruined your tightly packed schedule. Your guidance always meant a great deal to me and I would like to think I became a better person and scientist because of it. And I appreciate that you always openly communicated with me, and gave me your opinion on matters. Unless it is about *stroopkoeken*, which are clearly superior to *stroopwafels*, no matter what you say. Bedankt voor alles, Paul.
I want to thank Prof. Maxim Pchenitchnikov for taking the time to read through my thesis and be my second examiner. I also want to thank Prof. Stefan Schlemmer to agree to chair the disputation.
I want to express my gratitude towards my thesis advisory committee, Prof. Arne Lützen and Prof. Manuela Schiek. Your support and encouraging words for my projects were as valuable to me as your scientific guidance as collaborators. Without your deep knowledge of everything squaraine-related, and the dark magic that is

molecule synthesis, this thesis would not have been possible. This extends of course also to Jennifer Zablocki and Marvin Schumacher, who supplied me non-stop with high-quality samples.
Part of this great collaboration was my membership in the TIDE research training group. I want to thank everyone in the TIDE team, but especially Prof. Klaus Meerholz, for enabling this platform. It was a great privilege to be part of this cohort, meeting great colleagues, going to interesting places, and learning much more than in a usual PhD program. The research residence in particular was a unique opportunity to live in another country and gain more scientific experience. I want to thank Prof. Thomas la Cour Jansen and the Zernike Institute of Advanced Materials of the University of Groningen for being a great host, for letting me be part of his group for a while, and for teaching me the ways of computational spectroscopy. Moreover, I want to thank Prof. Thomas Jansen and Prof. Jasper Knoester for their excellent collaboration. Furthermore, I want to thank Prof. Anna Painelli and Prof. Daniele Fazzi for great and fruitful scientific discussions.
During my time in Groningen, I had the pleasure to work with great colleagues. I want to mention a special thank you to Marick Manrho, who was always there for me when I struggled with problems. Your excellent and at times scary knowledge of python helped me out countless times; in fact so often, that I had a "I need help with python" sticker almost permanently glued to your desk. Our discussions were always of great value, be it about the parametrization of intermolecular charge transfer, or how to calculate the entropy of a chess game. Thank you for making Fridays by far the best day of the week during my stay. I am very proud to count you as a colleague and a friend. The same holds true for Vesna Eric, who has been a great office and conference mate. I enjoyed our hourlong discussions a lot, which usually started scientifically, but ended up with existential questions about society and life itself.
I want to thank Dr. Jingyi Zhu for your time as my day-to-day supervisor. Thank you for your never-ending patience with me in the lab, and for teaching me how to get a job done. You taught me how to be self-reliant and how to learn things fast, and I am sure any project would take twice as long without you. It was a sad day when you moved to Dalian, but I hope you thrive there and that you can enjoy the beaches as much as you hoped. Thank you, Jingyi!

Dr. Tianyi Wang, I also want to thank you for being my subgroup leader in the last year. Even though my work was very unfamiliar to you in the beginning, you picked everything up incredibly fast and started to bring structure into our "at times" unorganized subgroup. Your genuine curiosity and readiness to always learn something new was always very inspiring, and I appreciate a lot that we established an open-minded and constructive discussion culture in the subgroup, be it about science or not. I will forever be in your debt for the countless hours you put into proof-reading and discussing my thesis. While I know that you are very modest about this, you went above and beyond your duty as a supervisor and I will never forget that we sat in the office until 1:30 AM on a Saturday to correct the thesis. Thank you for your great display of leadership, Tianyi!

I was lucky enough to be a day-to-day supervisor myself, and I thank Omar Abdul-Aziz for having patience with me in this new role. I hope your PhD project will be as successful as your Master's!

I also want to extend my thanks to all former and present members of the OCMS group, who I had the pleasure of working with over the last couple of years. A special thank you belongs to Lukas Rieland, who has displayed true comradery over the last three years. It was a great pleasure working at your side. Especially when things didn't work out—which they usually did not—it was invaluable to me to know that I can count on your help. And even if I did not always answer each of your questions productively ("Is this an interlock?"), I hope you know that you can always count on my help.

Together with Chris Reinhoffer, we shared a good number of hilarious moments, especially during the move of our labs into the new building. Our designated lab move playlist is a testimony to our will to make the best out of any situation, which I got to enjoy a lot over the years.

Thanks also to Jens Koch, Claudia Hazel, and Dr. Thomas Koethe for always keeping our group running and organized.

I also want to thank Dr. Niels Ehlen, Dr. Andrea Bliesener, Dr. Peacock, Dr. Raphael German and Dr. Yannic Falke for many great social events throughout the years. I would also like to thank Alla Bezvershenko for very fruitful discussions, especially when it was not about science, and for all the convenient excuses you gave me to "meet theory collaborators" and grab a coffee.

Without a doubt, the person that I have to thank the most is Kateryna Vynokurova. Your care and support is absolute. No matter how bad work was that day, no matter which virus locked us at home, and no matter which dictator wants to ruin our way of life, you always put a smile on my face in the end of the day. I truly could not have done it without you. Дякую.

An dieser Stelle möchte ich meiner Familie von ganzem Herzen danken. Danke an meine Eltern, die immer für mich da waren, und stets meine Wissbegierde gefördert haben, auch wenn das nicht immer einfach war. Die immer Verständnis haben, dass ich mich häufig zu lange zu Hause nicht blicken lasse. Und die, auch wenn sie keine Ahnung haben, was ich genau an der Universität den ganzen Tag mache, mich dabei unterstützen und mir immer das Gefühl geben, dass meine Arbeit viel wert ist, und dass sie stolz auf mich sind.

List of Publications of the Author

Bernhardt, R.; Manrho, M.; Zablocki, J.; Rieland, L.; Lützen, A.; Schiek, M.; Meerholz, K.; Zhu, J.; Jansen, T. L. C.; Knoester, J.; van Loosdrecht, P. H. M.; Structural Disorder as the Origin of Optical Properties and Spectral Dynamics in Squaraine Nano-Aggregates *Journal of the American Chemical Society* **2022**, 144, 42, 19372-19381 (chapter 3)

Zhu, J.; Bernhardt, R.; Cui, W.; German, R.; Wagner, J.; Senkovskiy, B. V.; Grüneis, A.; Pichler, T.; Li, Y.; Li, X.; Wu, K.; Liu, R.; Zhu, X.; van Loosdrecht, P. H. M.; Shi, L.; Unraveling the Excitonic Transition and Associated Dynamics in Confined Long Linear Carbon Chains with Time-Resolved Resonance Raman Scattering *Laser & Photonics Reviews* **2021**,15,12, 2100259

Kuhn, H.; Wagner, J.; Han, S.; Bernhardt, R.; Gao, Y.; Xiao, L.; Zhu, J.; van Loosdrecht, P. H. M.; Excitonic transport and intervalley scattering dynamics in large-size exfoliated MoSe2 monolayer investigated by heterodyned transient grating spectroscopy *Laser & Photonics Reviews* **2020**, 14, 12, 2000029

Wagner, J.; Kuhn, H.; Bernhardt, R.; Zhu, J.; van Loosdrecht, P. H. M.; Trap induced long exciton intervalley scattering and population lifetime in monolayer WSe2 *2D Materials* **2021**, 8, 3, 035018

Cuzzupè, D. T.; Ünlü, F.; Lê, K.; Bernhardt, R.; Wilhelm, M.; Grosch, M.; Weißing, R.; Fischer, T.; van Loosdrecht, P. H. M.; Mathur, S.; Thermally-induced drift of A-site cations at solid-solid interface in physically paired lead halide perovskites

Scientific reports **2022**, 12, 1, 10241

Erklärung zur Dissertation

gemäß der Promotionsordnung vom 12. März 2020

Hiermit versichere ich an Eides statt, dass ich die vorliegende Dissertation selbstständig und ohne die Benutzung anderer als der angegebenen Hilfsmittel und Literatur angefertigt habe. Alle Stellen, die wörtlich oder sinngemäß aus veröffentlichten und nicht veröffentlichten Werken dem Wortlaut oder dem Sinn nach entnommen wurden, sind als solche kenntlich gemacht. Ich versichere an Eides statt, dass diese Dissertation noch keiner anderen Fakultät oder Universität zur Prüfung vorgelegen hat; dass sie - abgesehen von unten angegebenen Teilpublikationen und eingebundenen Artikeln und Manuskripten - noch nicht veröffentlicht worden ist sowie, dass ich eine Veröffentlichung der Dissertation vor Abschluss der Promotion nicht ohne Genehmigung des Promotionsausschusses vornehmen werde. Die Bestimmungen dieser Ordnung sind mir bekannt. Darüber hinaus erkläre ich hiermit, dass ich die Ordnung zur Sicherung guter wissenschaftlicher Praxis und zum Umgang mit wissenschaftlichem Fehlverhalten der Universität zu Köln gelesen und sie bei der Durchführung der Dissertation zugrundeliegenden Arbeiten und der schriftlich verfassten Dissertation beachtet habe und verpflichte mich hiermit, die dort genannten Vorgaben bei allen wissenschaftlichen Tätigkeiten zu beachten und umzusetzen. Ich versichere, dass die eingereichte elektronische Fassung der eingereichten Druckfassung vollständig entspricht.

05.03.2024, Robin Bernhardt